INTERFACE EFFECT ON THE PHOTOVOLTAIC PROPERTIES OF BIFEO$_3$

XING LI

M.Phil

The Hong Kong Polytechnic University

2016

The Hong Kong Polytechnic University
Department of Applied Physics

Interface Effect on the Photovoltaic Properties of $BiFeO_3$

XING LI

A thesis submitted in partial fulfillment of the requirements
for the degree of Master of Philosophy

October 2015

CERTIFICATE OF ORIGINALITY

I hereby declare that this thesis is my own work and that, to the best of my knowledge and belief, it reproduces no material previously published or written, nor material that has been accepted for the award of any other degree or diploma, except where due acknowledgement has been made in the text.

__________________________________ (Signed)

____Xing Li____________________________ (Name of student)

Abstract

Ferroelectric-photovoltaic (FePV) devices employing a homogeneous ferroelectric material as the light absorbing layer, have been investigated intensively during the past decades. The physical mechanism governing the FePV effect is distinctly different from that of a typical *p*-*n* junction type photovoltaic (PV) effect, whose open-circuit voltage is limited by the bandgap of the light absorbing material. Therefore, FePV material is regarded as the potential candidate for above-bandgap solar cells. Among all the FePV materials, $BiFeO_3$ (BFO), possessing simultaneous ferroelectric and antiferromagnetic orders at room temperature, is most widely studied in the last decade.

In this thesis, systematic experimental work has been carried out to investigate the FePV effect in BFO.

First, the influence of secondary phase on FePV of BFO thin film was examined. Pulsed laser deposition (PLD) was used to fabricate epitaxial BFO thin films. Three different targets were used for laser ablation and different ablation parameters (oxygen pressure and laser pulse frequency) were tried to obtain phase pure BFO thin film. Our results demonstrated that the photocurrent and photoconductivity of BFO thin films are closely related to Bi_2O_3 secondary phase and bismuth vacancies. A large photocurrent density of 12 mA/cm^2, a large remnant polarization of 60 $\mu C/cm^2$ and good switching behaviour were observed in optimized epitaxial BFO films.

Second, the influence of metal-semiconductor interface effect on BFO FePV was studied. Titanium (Ti) and gold (Au) metals are used as symmetric in-plane electrodes, respectively, on optimized BFO thin films. Since the work functions of Ti and Au are different, which are above and beneath the Fermi level of BFO, respectively, Ohmic contact is formed at the Ti/BFO interface and Schottky contact is formed at the Au/BFO interface. The contact types were confirmed by Kelvin probe force microscopy. The photovoltaic behaviours of these two types of electrode BFO thin films were performed and the photocurrent is larger in a BFO thin film with an Ohmic contact.

Last, but not least, the strain effect on BFO FePV behaviour was studied. Epitaxial BFO thin films are deposited on $LaAlO_3$ (LAO) [1 0 0] and $0.67Pb(Mg_{1/3}Nb_{2/3})O_3$-$0.33PbTiO_3$ (PMN-PT) [1 1 1] substrates. No obvious increase in short circuit photo-current was detected in BFO/LAO sample which has a tetragonal-like BFO phase, as confirmed by Raman spectroscopy. However, large photoconductivity at large voltage bias was obtained. A small but non-trivial photovoltaic effect was observed in BFO/PMN-PT sample with a rhombohedral structure. It is concluded that the FePV effect is also closely related to the symmetry group of the lattice structure. A prominent photo-response was observed in strain-free electrospun BFO nanofibers, which may have potential applications due to the flexible nature of the nanofibers.

List of Publications

1. Linfeng Fei, Yongming Hu, **Xing Li**, Ruobing Song, Li Sun, Haitao Huang, Haoshuang Gu, Helen L. W. Chan, and Yu Wang, "Electrospun Bismuth Ferrite Nanofibers for Potential Applications in Ferroelectric Photovoltaic Devices," *ACS Appl. Mater. Interfaces*, vol. 7, no. 6, pp. 3665–3670, 2015.

2. **Xing Li**, Biaolin Peng, Yu Wang, Siu Hong Choy, Helen L. W. Chan, and Haitao Huang, "Complex Deposition Dynamics Investigation in Synthesis of Highly Epitaxial Multiferroic Thin Film," *presented at The 6th Chian-Japan Symposium on Ferroelectric Materials and Their Applicaitons, Yamanashi, Japan, 2014*

3. Biaolin Peng, Qi Zhang, **Xing Li**, Tieyu Sun, Huiqing Fan, Shanming Ke, Mao Ye, Yu Wang, Wei Lu, Hanben Niu, James Scott, Xierong Zeng, Haitao Huang, "Giant Electric Energy Density in Epitaxial Lead-Free Thin Films with Coexistence of Ferroelectrics and Antiferroelectrics," *Adv.Electr.Mater. 1, 1500052 (2015)*

Acknowledgments

First and foremost, I would like to express my sincere gratitude to my supervisors, Dr. H.T. Huang and Dr. S.H. Choy, for their patience and valuable guidance throughout my period of postgraduate studies. I also highly appreciated it that they always give me trust and support in the research. I would also like to thank Dr. Y. Wang, Prof. J.Y. Dai, Dr. X.M. Zhang in their assistance for my research and coursework studies.

My genuine thanks go to Dr. B.L. Peng for his helpful advices ferroelectric and dialectic measurements, to Mr. Y.Z. Liu and Mr. K. Au for their assistance in thin film deposition and XRD measurements, to Dr. Y.Z. Xie and Dr. P. Lin for their assistance in photolithography, to Dr. L.F. Fei for his assistance in SEM operations, to Dr. T.Y. Sun and Mr. Z.H. Yong for their assistance in theoretical discussion.

I am grateful to all my friends and colleagues in AP for their help and assistance. They include Ms. R.B. Song, Dr. N.Q. Fu, Dr. M. Guo, Ms. Y. Liu, Dr. C. Huang, Dr. T. Li, Mr. J.J. He and Mr. H.Y. Jin.

I gratefully acknowledge the financial support from the Department of Applied Physics and the Centre for Smart Materials of the Hong Kong Polytechnic University.

Last but not least, I would like to thank my parents, for their love, support and patience that inspired me to continue my study.

Table of Contents

Chapter 1. Literature Review

1.1 Introduction of ferroelectric photovoltaic effect

Since 19th century, the world population has been experiencing a steady and rapid growth, especially after the World War II. As a result, the total energy consumption by human beings on the earth has also roared up and reached as high as 143,851 terawatts-hours per year until 2008, and eighty-one percent of that comes from fossil fuels. However, the traditional energy sources, such as fossil fuels (crude oils, natural gas, etc.), are not only limited in amount, but also environmental unfriendly. For the sustainable development of human society, the exploration of renewable energy sources is in urgent need. Among the existed candidates, solar energy is a promising one, since it is green, unlimited in amount and can be utilized in most areas on the Earth. By now, various solar technologies have been employed for efficient and effective utilization of solar energy, including solar heating, solar thermal electricity and solar photovoltaic. In recent years, solar photovoltaic technology has attracted the most attention because of its relatively high conversion efficiency. And it is now generally regarded that, photovoltaic technology is such an important complement, even a replacement, hopefully, of fossil combustion in the near future.

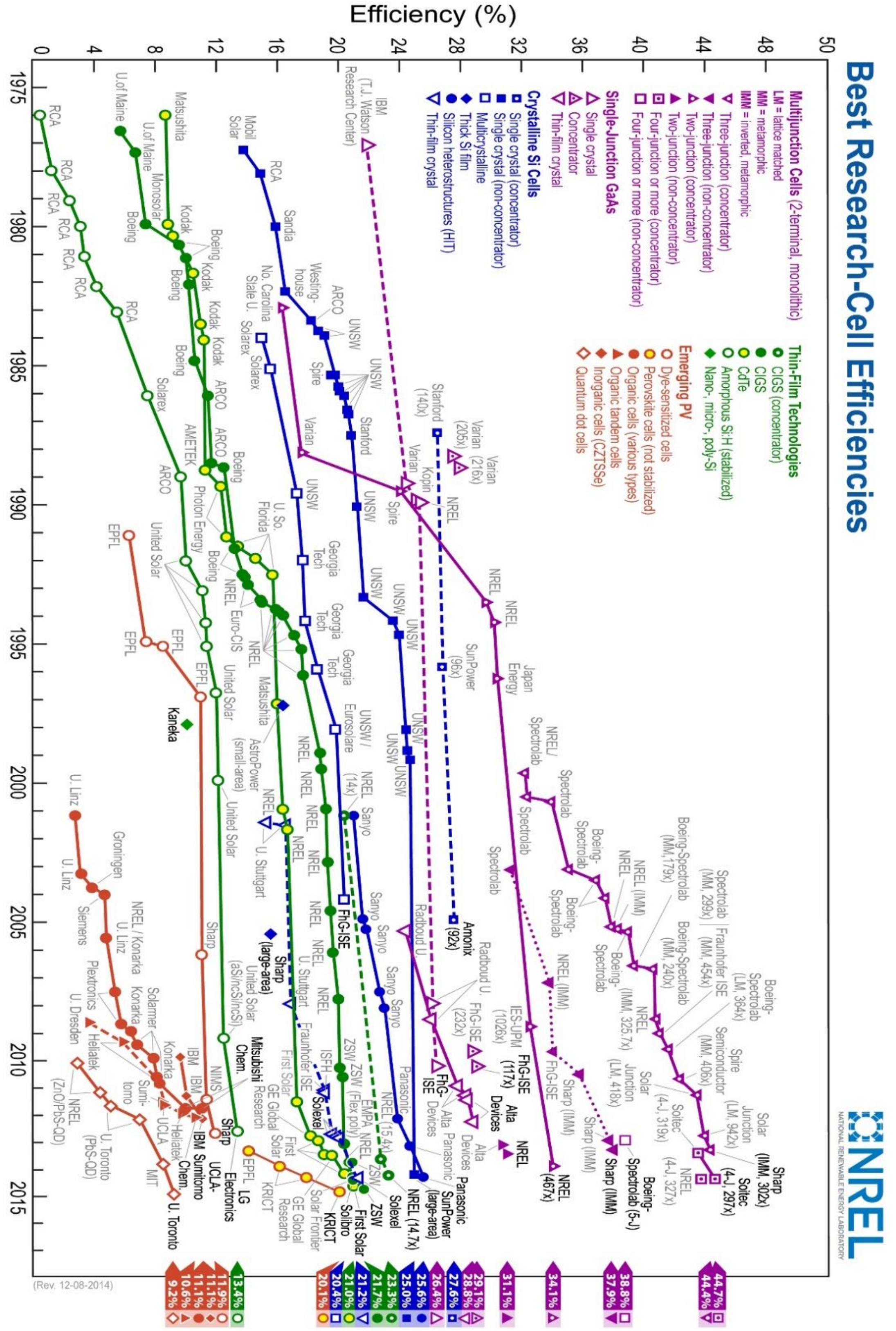

Fig. 1.1 Best efficiencies for solar cells in labs dated to 2015 (provided by NREL).

Upon decades of development, various types of solar cells have been invented, such as thin film crystalline silicon solar cells, amorphous silicon solar cells, copper indium gallium selenide solar cells, dye-sensitized solar cells, cadmium telluride solar cells, quantum dot solar cells, organic solar, and perovskite solar cells, *etc.* The world record of conversion efficiency for these cells has been shown in Fig 1.1. Besides these solar cells, ferroelectric solar cell has its unique structural characteristics and mechanism. It is a single-material cell other than those based on various p-n junctions. Its photo-electric conversion mechanism is quite different from other solar cells. And hence, the investigation of ferroelectric photovoltaic (FePV) phenomenon is quite hot in recent years.

The FePV effect was first observed at around 1960s in $BaTiO_3$ single crystal, which is a ferroelectric material lacking of central symmetry[1]. Compared with other types of solar cells, ferroelectric solar cell can generate a high photovoltage which is normally several orders of magnitude larger than that of p-n junction type solar cells, and the value of photovoltage is simply proportional to the separation distance of electrodes. Another feature of ferroelectric photovoltaic effect is that a steady-state photocurrent is generated along the polarization direction; though the photocurrent is relative small, which can be simply reversed by switching the polarization to the opposite direction. This phenomenon was also found in other ferroelectric bulk materials like LNO, SBN, PLZT and BFO[2][3]. However, due to the small photo-electric conversion efficiency, investigations of ferroelectric solar cell stalled shortly afterwards.

In recent years, upon the rapid development of thin film technology, the research of FePV effect has been rejuvenated and with the help of scanning probe system, a photo conversion efficiency of 10% has been reached. Moreover, switching of photocurrent in ferroelectric thin film is fast with low energy loss. This feature renders potential application of ferroelectric materials for new generation of non-volatile memory devices. FePV effect is also applicable for light sensors and actuators which have advantages of high accuracy, fast response and good durability. Due to these charming and promising applications, FePV is currently one of the major research fields in materials and physical sciences, and many novel features associated with FePV are to be uncovered.

1.2 Possible mechanisms of FePV effect

The exciting FePV phenomenon is widely observed in most ferroelectric materials. However, the mechanism behind it is still not fully understood. Considerable amount of experiments were conducted aiming to uncover its physical nature, and several theories were built up in recent years. In this section, some mainstream interpretations of FePV effect are presented.

1.2.1 Surface charge model

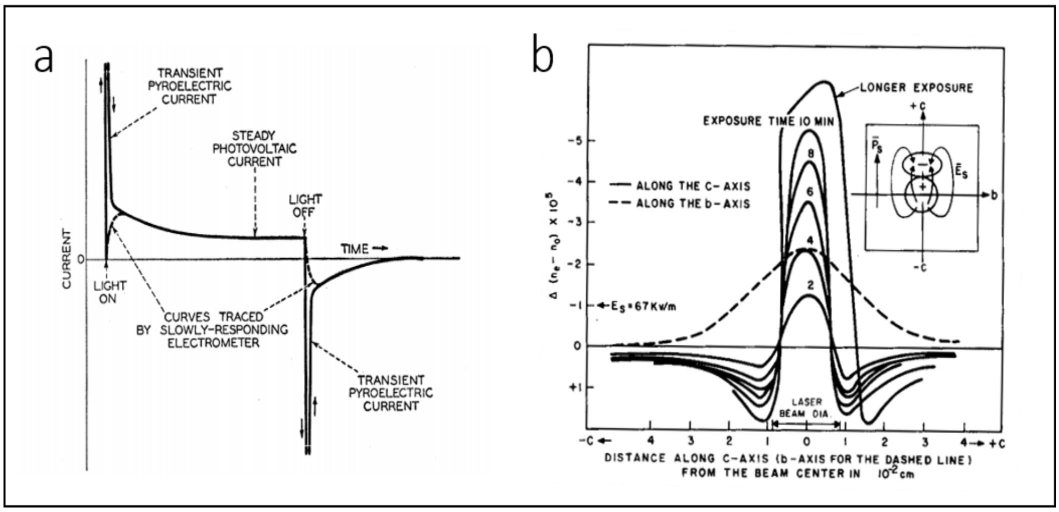

Fig. 1.2 (a) Schematic diagram showing the time variation of the current during a slow light-dark cycle. The pyroelectric and photo-voltaic components of the total current are indicated; (b) Optically induced index change along the *b* and c axes with various exposure time. Space-charge field *E_s* shown in the inset causes the observed distribution of $\Delta(n_e - n_o)$. Reprinted from A. G. Chynoweth et al[1]. and F. S. Chen et al[4].

A. G. Chynoweth's work published in 1956 was normally regarded as the first observation of photovoltaic effect in ferroelectric materials. As shown in Fig. 1.2 (a), he discovered that, when BTO single crystal was under illumination, a transient current followed by a steady state current was detected from in-plane electrodes placed on crystal surface. Chynoweth then attributed the transient and large photocurrent to pyroelectric effect caused by movement of impurity ions in the space-charge layer on the crystal surface by investigating the transient pyroelectric current below and above the Curie temperature. He concluded that the steady-state photovoltaic current was driven by the same force for the transient pyroelectric current. However, no specific form of this force was given in his work.

Another early work done by F. S. Chen showed that, when $LiNbO_3$ and $LiTaO_3$ single crystals were illuminated, the refractive indices at the illuminated area would change, as shown in Fig. 1.2 (b). The author carefully examined the change of the difference between ordinary and extraordinary refractive indices, i.e. $\Delta(n_e - n_o)$, under different illumination duration and intensity. The extraordinary index of refraction was observed to decrease by 0.001 with a focused Ar laser of 20 mW intensity at λ= 0.488 μm, while the change of ordinary index was much smaller. A model was proposed that the local change of refractive indices was attributed to the drifting of photoexcited electrons out of the illuminated region followed by their retrapping near the beam periphery. The author believed that there are two types of electron traps before light illumination, and an unknown internal electric field is responsible for dragging of photoexcited electrons from filled traps to empty ones until the electrons are moved out of illuminated area and immobilized. The specific form of this internal field was not discussed in this work, except that it was in the antiparallel direction of the spontaneous polarization.

However, the above two proposed mechanisms either failed to incorporate the photovoltaic phenomenon, or lacked concrete details. A more fundamental theory is required to explain the FePV phenomenon.

1.2.2 Bulk photovoltaic effect theory

In 1974, Glass *et al.* attributed the photocurrent in ferroelectric material to bulk photovoltaic (BPV) effect for the first time (for the best of our knowledge)[2]. A more comprehensive model proposed by B. Baltz and W. Kraut explained BPE as a consequence of breakdown for spatial symmetry, not only time-reverse symmetry[5][6][7][8]. Though the BPE was first identified in ferroelectric material, the existence of such effect was also predicted and verified in other non-ferroelectric materials which are belong to any non-centrosymmetric space groups. For certain space groups (only one exception in the 21 crystal classes that lack a center of inversion symmetry), the photocurrent arises because the real-space center of charge for the valence bands differs from that for the conduction bands. Fig. 1.3 illustrated a simple situation of the electron movement when a simple ferroelectric material is illuminated: only two electron states are considered. After the absorption of photons, electrons would move in the A-B-C direction, where the blue line represents excitation and the purple one represents decay. Due to the breaking of spatial symmetry, electrons moving along the reverse way, e.g. C-B-A, need larger thermal activation, thus only happens with very small possibility.

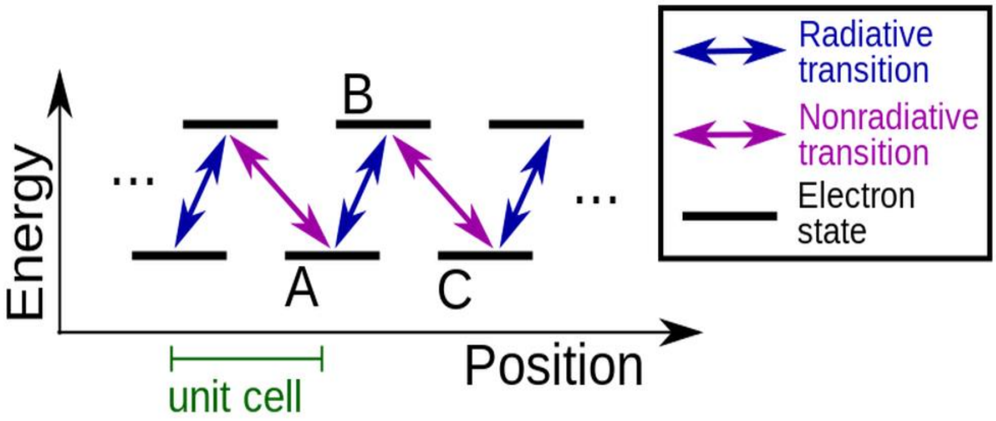

Fig. 1.3 Illustrative diagram of movement of electrons excited by illumination in bulk photovoltaic effect. Reprinted from Wikipedia.

Usually, the experimental result of BPV effect can be quantified as:

$$J_{ph} = \alpha(\omega) G(\omega) I_0 \tag{1}$$

where ω denotes the frequency, I_0 is the radiation intensity on sample surface, α(ω) denotes the absorption coefficient of the crystal, and G(ω) denotes Glass's photovoltaic coefficient, which depends on the polarization of the radiation. This form of expression is only suitable for the situation when the current measurement is along the polarization direction. If the current measurement direction is not placed parallel to the polarization, then the Glass coefficient should be replaced by a third-rank tensor, e.g.

$$\boldsymbol{J_i = I\beta_{ijk}e_je_k}$$

Where $\boldsymbol{e}_j$and $\boldsymbol{e}_k$ are projections of electromagnetic field vector, and $\boldsymbol{\beta}_{ijk}$ represents the ability to respond to electromagnetic field. And the photovoltage can be expressed as

$$V_{oc} = \frac{J_{ph}}{\sigma_d + \sigma_{ph}} d \qquad (2)$$

in which σ_d and σ_{ph} denotes dark conductivity and photoconductivity, d denotes electrodes separation distance, which is very critical to obtain a high overall open circuit voltage, e.g. V_{oc}. Under this model, the photocurrent and photovoltage are both well-defined and easily quantified. Various experiments have been designed to testify its correctness, and the third rank tensor has been obtained for different materials[9][10][11].

Although the BPV theory has successfully explained many experimental phenomena, its microscopic origin is still lack of detailed description. In recent years, a shift current theory is thought as the dominant mechanism to give rise to a truly bulk effect in ferroelectric photovoltaic behavior[12][13]. The term *shift current* is nonlinear optical process, giving rise to a truly bulk effect and having been verified by first-principles calculations. The term *shift current* also vividly depicts the electron movement in real space realm, e.g. from one unit cell to another, which is different from the electron-hole flow in kinetic space in a typical semiconductor or metal.

1.2.3 Depolarization field theory

The bulk photovoltaic theory is good enough to explain most observations performed on bulk materials. In thin film situation, however, more factors should be considered. One frequently mentioned mechanism for photovoltaic effect in ferroelectric thin films is the depolarization field theory[14]. In a polarization process, after the removal of an external DC field, the electrodes should normally be connected to neutralize redundant free charges. Occasionally, due to impurities or defects around the electrode-sample interface, the charge neutralization may be imperfect. Thus, those unscreened boundary charges would build up an internal field which could be the driving force for electron-hole separation when an atom is excited by a photon. In bulk scale, the depolarization field is too weak to provide a strong force, but in thin film scale, the depolarization field could play a critical role that needs careful consideration.

1.2.4 Domain wall theory

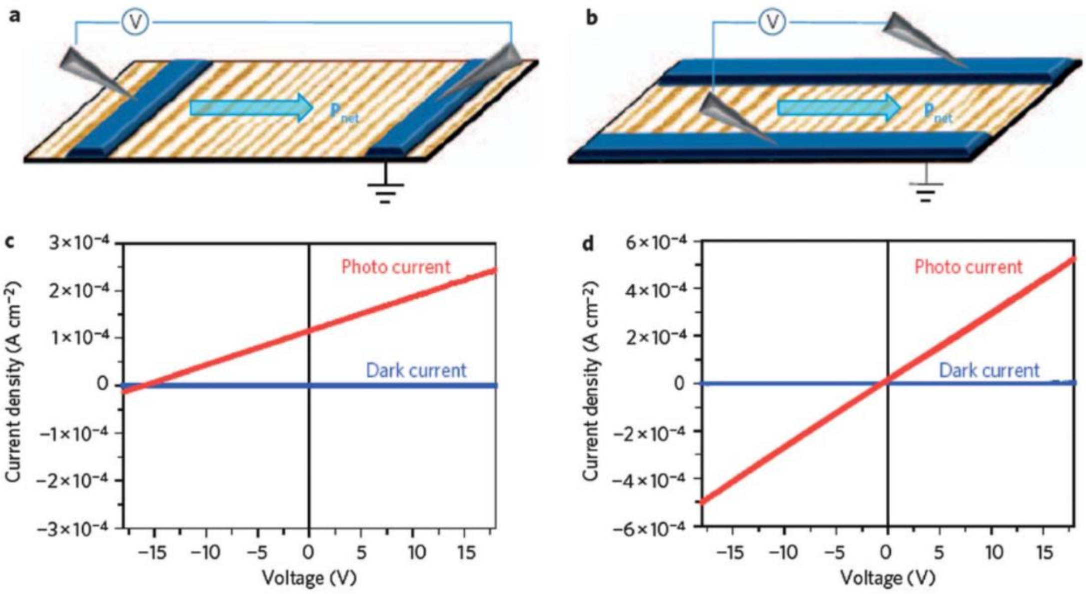

Fig. 1.4 Schematics of the measurement configuration with (a) perpendicular domain walls (DW⊥) and (b) parallel domain walls ($DW_{||}$). The corresponding I-V curves for the devices in (a) and (b) are shown in (c) and (d), respectively. Reprinted from Yang et al.[15].

Recently, Yang *et al.* have examined the FePV effect in rhombohedrally distorted $BiFeO_3$ (BFO) thin films with periodic stripe domains[10][15][16][17], and their work provides a big step forward because it presents important insight into the photovoltaic effect in ferroelectrics. Since BFO has a rhombohedral–orthorhombic transition at its Curie temperature, three types of domain walls exist in a BFO epitaxial thin film. By using a strain engineering method, they have successfully separated 71^o and 109^o domain walls on different samples, and measured the photo-electric response using two electrode configurations, namely, perpendicular domain walls ($DW_{\perp}$) and parallel domain walls ($DW_{||}$), as shown in Fig. 1.4 (a) and (b), respectively. It is observed that the photovoltage in the $DW_{\perp}$ configuration was prominent and much larger than the bandgap of BFO, but vanished in the $DW_{||}$ configuration, as shown in Fig. 1.4 (c) and (d), respectively.

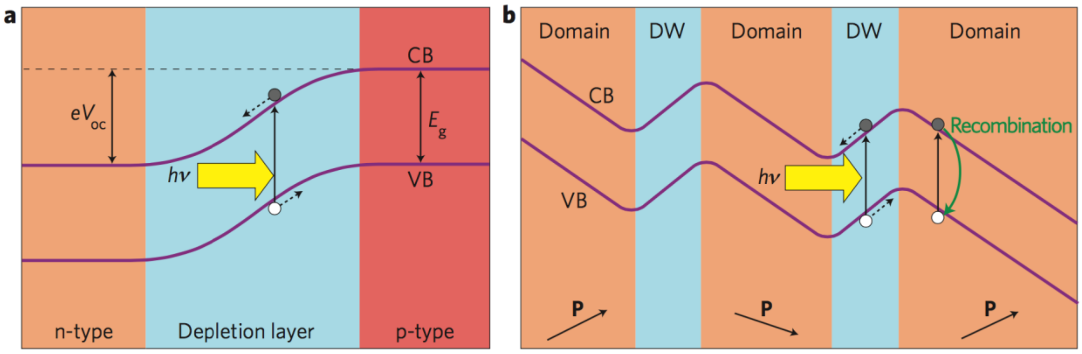

Fig. 1.5 Principles of operation for a conventional solar cell and the ferroelectric alternative. (a) Band diagram of a conventional semiconductor p–n junction, showing the conduction band (CB), valence band (VB), bandgap (Eg) and open-circuit voltage (Voc). Here, *hv* is the energy of the incident photon and *e* is the elementary electric charge. (b) In the ferroelectric domain, band bending occurs across the domain wall (DW). The directions of electric polarization (P) are shown by arrows. Reprinted from Haitao Huang[17].

The authors suggested a new model to explain the phenomenon. According to previous *ab initio* calculations, ferroelectric domain walls have built-in potential steps[18][16], arising from the component of the polarization perpendicular to the domain wall. The intrinsic potential drop at 71° domain walls (~10 mV)[16] induces a huge electric field of ~$5x10^6$ V m^{-1} inside the narrow domain wall, which was suggested to be a strong driving force for the dissociation of the photo-generated exciton. When the sample is illuminated, each individual domain wall act as a nanoscale p-n junction connected by adjacent domains in which the photogenerated charge carriers are localized and tightly bound, as shown in Fig. 1.5.

The domain wall theory gives an important complementary explanation for ferroelectric photovoltaic effect besides bulk theory, and, for the first time, the ferroelectric domain walls are thought to be functional rather than functionless thin layers. Recent study suggests that domain walls in epitaxial BFO thin film is more conductive than bulk domains where the dark conductivity in the DW⊥ configuration is much smaller than that in the $\mathrm{DW}_{||}$ configuration[11].

1.3 Ferroelectric photovoltaic effect in bismuth ferrite

1.3.1 Introduction of bismuth ferrite

Multiferroics are usually defined as single-phase crystals exhibiting both ferromagnetism (or anti- ferromagnetism) and ferroelectricity (or antiferroelectricity) at a certain temperature and pressure. The interest in multiferroics at present is growing rapidly, and the interest is twofold: (1) from a fundamental point of view, the coupling between spins and lattices in crystals has been recognized as complex and fascinating for several decades; and (2) multiferroics also present a possible avenue for the next generation of computer digital memories, in which information would be stored by magnetization, and read solely by electric fields. However, the phase transition temperature (from para-phase to ferroic-phase) of most multiferroics is below ambient temperature, thus room temperature multiferroics will be of great importance, one of them being BFO[19][20][21][22][23][24].

BFO possess a rhombohedral structure (point group R3c) at room temperature[25] The perovskite-type unit cell has a lattice parameter of 0.3956 nm, and a rhombohedral angle of 89.3–89.4^o at room temperature[26], with ferroelectric polarization along $[1\ 1\ 1]_{pc}$[26]. The unit cell can also be described in a hexagonal frame of reference, with the hexagonal c-axis parallel to the diagonals of the perovskite cube, i.e., $[001]_{hex} \parallel [1\ 1\ 1]_{pc}$. The hexagonal lattice parameters are a_{hex} = 0.558 nm and c_{hex} = 1.39 nm[26][27][28]. The coefficient of thermal expansion is neither completely linear nor isotropic[29][30][27], and the reported values differ notably, ranging from ca. 6.5 to 13 x 10^{-6} K^{-1}[29][27].

The study of BFO as a magnetoelectric (coupling between electric and magnetic ferroic orders) material was pioneered as early as 1960s. In 1963, Kiselev *et al* found BFO to be a G-type antiferromagnet with Néel Temperature at around 640 K. [102] In 1970 Teague *et al* reported the first polarization-electric field hysteresis loop at low temperature with a polarization value of only 6 μC/cm^2[31]. The small value of polarization is own to sample leakage, and the difficulties in preparing high a quality BFO single crystal had prevented the investigation of its ferroelectric properties. The rejuvenation of studying BFO material was initiated by R. Ramesh's group in 2003[32]. In 2003's work, the [0 0 1]$_{pc}$-oriented BFO epitaxial thin film grown on a single crystal substrate showed a remnant polarization as high as 55 μC/cm^2 and an enhanced thickness-dependent magnetism as compared with the bulk BFO. It was the first time that a large polarization was observed in a lead-free ferroelectric material, and the ferroelectric property was later found to be intrinsic rather than strain induced which was proposed by the authors. In 2007, Lebeugle *et al* and Shvartsman *et al* showed that the polarization in bulk BFO is about 100 μC/cm^2 along [1 1 1]$_{pc}$, which is the highest reported value in bulk ferroelectrics[33][34].

Besides exceptional ferroelectric properties, the optical properties of BFO are also remarkable. The bandgap is low compared to most ferroelectric perovskites, with reported values in the range of 2.6 to 3.0 eV[35]. The corresponding absorption edge is in the visible range, which has kick-started the theoretical and experimental investigation of FePV in BFO[33][36].

In recent years, the study of BFO is mainly focused on fabrication and characterization of epitaxial thin film and its physical properties. By a so-call strain engineering method, the lattice structure and domain pattern of BFO thin film could be modified in a way that is impossible for the bulk material.

Strain Engineering of BFO thin film

By using different substrates, the properties of BFO thin film could be changed greatly[37][38][39][40][41]. A wide range of single crystal perovskite substrates, with various orientations and miscuts, have enabled diverse manipulation methods of the crystalline structure in a BFO epitaxial thin film. Reports of pure tetragonal, tetragonal-like (T-like) Monoclinic M_C, orthorhombic, rhombohedral-like (R-like) monoclinic M_A and monoclinic M_B BFO films can all be found in literature[42][43][44][45][46][47][48]. The most frequently used substrates are $SrTiO_3$ (STO), and the lattice structure of BFO thin film deposited on STO would be changed from pure tetragonal to rhombohedral phase at different thickness. $DyScO_3$ (DSO) is another frequently used substrate since its in-plane lattice constant in [1 1 0]-direction is almost the same as the lattice constant of bulk BFO. Through strain-engineering approach, an electric field driven phase transition can be achieved, analogical to the morphology phase boundary in piezoelectric materials. R. J. Zeches *et al.* have found that BFO thin films deposited on $LaAlO_3$ (LAO), $YAlO_3$ (YAO) substrates could exhibit a stable mixed-phase topology between pure tetragonal-like phase and a mixture of T-like and R-like phases[42], which is tunable by electric field. By proper choose of substrate and deposition condition, a remnant polarization of ~150 μC/cm^2 could be obtained in highly strained thin film with T-like phase, which is 1.5 times that in bulk rhombohedral phase[49]. Those features open new prospects for BFO material for the applications in nano-sized and nonvolatile electronic devices.

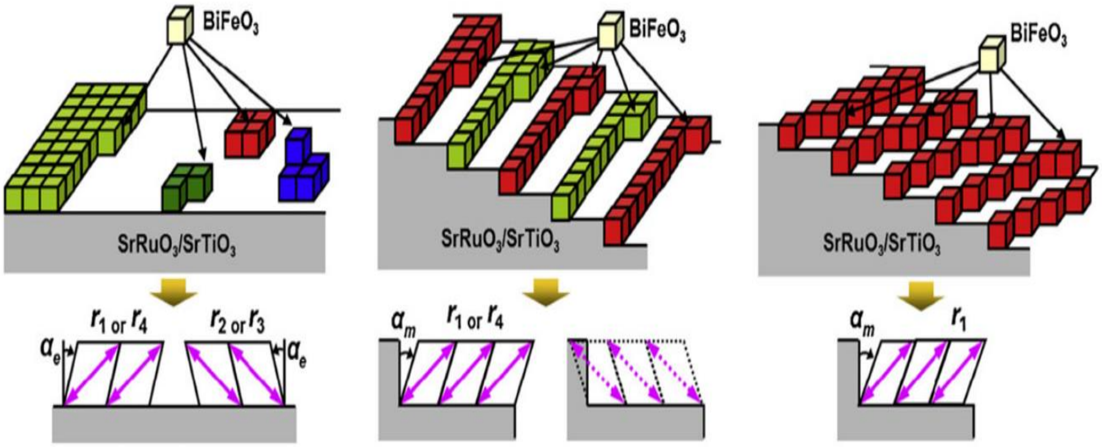

Fig. 1.6 Schematic illustration of domain engineering of $BiFeO_3$ thin films by miscut substrates. (a) 4-Variant $BiFeO_3$ on exact (0 0 1) $SrTiO_3$ single crystal substrate. (b) 2-Variant $BiFeO_3$ on substrate with 4 miscut along [1 0 0]. (c) Single-variant $BiFeO_3$ on substrate with 4 miscut along [1 1 0]. Reprinted from J.E. Giencke *et al.*[40].

It is also possible to control the ferroelectric domain pattern through strain engineering[40][50][46][52][53]. Since strain-free phase of BFO is rhombohedral, the polarization can point along one of the eight diagonal directions, giving rise to eight possible domain variants, and 3 types of domain walls: 71^o, 109^o and 180^o. The complexity would result in random domain patterns on the thin film surface, thus preventing further investigation of the detailed behavior and functionalities of ferroelectric domains in BFO. However, by using appropriate-cut substrates, e.g. vicinal STO substrate, the freedom of polarization directions can be reduced to two or one. Fig. 1.6 shows three types of substrate: no miscut, miscut along $[1\ 0\ 0]_{pc}$ (2-variant), and miscut along $[1\ 1\ 0]_{pc}$ (1-variant). The miscut angle is proportional to the accumulated step height across the entire surface, and the larger angle leads to more steps on the surface, hence smaller step area. Y. Chu *et al.* [50][51] showed that there were only two types of domain walls (109^o and 71^o) when BFO was deposited on 0.5^o miscut STO substrate; and when the miscut angle of 1-variant STO substrate was increased from 0.5^o to 3^o, the 109^o domain walls gradually disappeared and left only 71^o domain walls. The reduction of domain types renders two advantages: first, 109^o domain wall is thought to be much leakier than 71^o one, thus the ferroelectric property of the thin film containing pure 71^o domain walls is better than that deposited on no-miscut substrate; second, the separation of two types of domain walls provides better chance to unveil new insights in photovoltaic effect of BFO, as we have discussed in previous section[16][22][42][54].

After thirteen years of development, the understanding of BFO material is very comprehensive, and various kinds of applications of BFO material were proposed. In the following sections, recent work on photovoltaic effect of BFO material in single crystals, thin films and nanofibers are presented.

1.3.2 FePV effect in BFO single crystals

Although FePV has been discovered for half a century, the investigation of photovoltaic effect in BFO remained absence until 2008[33]. The long period of blank is mainly due to the high conductivity of BFO samples. Compared to thin films or ceramics, single crystals are normally viewed as of better quality and simple in nature. Therefore, they are very important in preliminary research stage. Here we present several work in FePV effect of BFO single crystals.

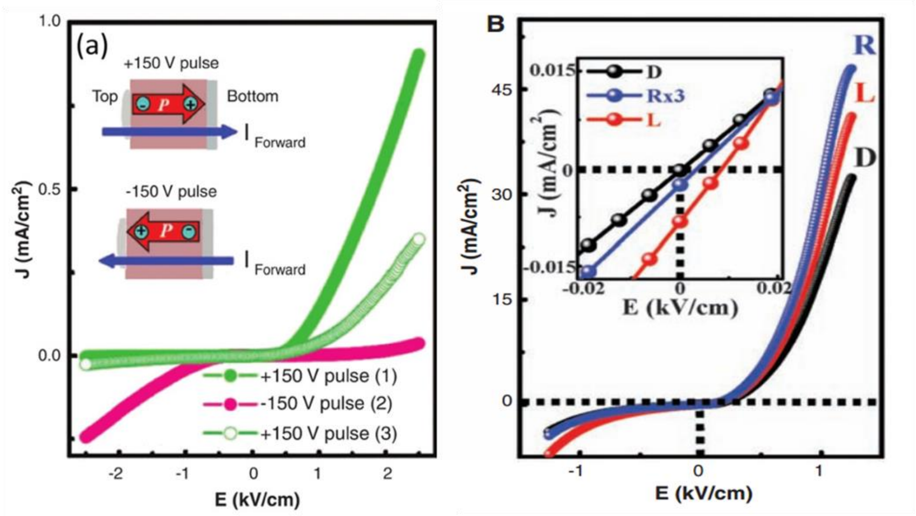

Fig. 1.7 (a) Photocurrent flipping when applied opposite voltage to BFO single crystal; (b) J-E curve in the dark (D) and with green-light illumination on right (R) or left (L) semitransparent Au electrodes. Reprinted from T. Choi et al. [36]

In 2009, T. choi *et al.* showed a diode like behavior in BFO single crystals when they were subjected to illumination under green light (Fig. 1.7 (b))[36][55]. One interesting phenomenon was showed in this work: the photocurrent direction is flipped according to opposite polarization (Fig. 1.7 (a)). The observed switching behavior has recently been confirmed in thin film structure and is of great application significance, since a new type of non-volatile memory device is possible based on this discovery. Recently, R. Moubah *et al.* [56] have measured the photocurrent in BFO single crystal with in-plane electrode configuration. They also confirmed the switchable behavior of photocurrent. However, the diode-like I-V curve was not obvious in Fig. 1.7, revealing that the optical rectification in BFO is not raised by bulk effect but related to self-doping induced by polarization at electrode-sample interface. This conclusion was further verified by H.T. Yi *et al.* [55].

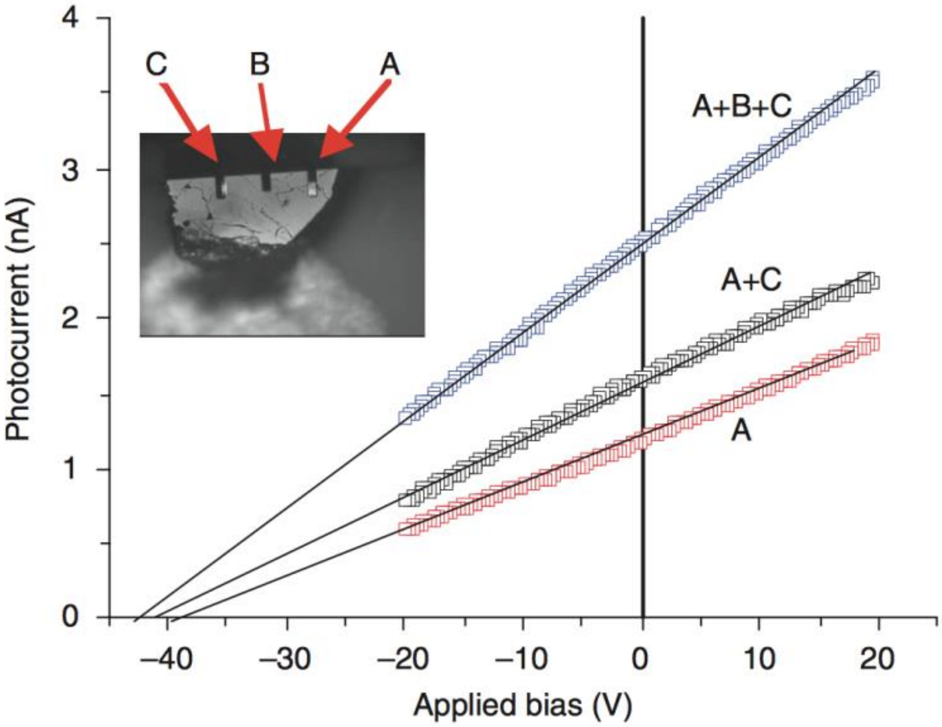

Fig. 1.8 Photocurrent–voltage characteristics obtained by successively contacting three tips of a multicantilever AFM chip. The lines represent a linear fit to extrapolate the I–V characteristic to V_{oc}. The inset shows an image of the three tips on the (100)-oriented BFO crystal. Reprinted from Marin Alexe & Dietrich Hesse[57]**.**

One drawback of ferroelectric materials that hinders their practical applications in photovoltaic market is their low light-electricity conversion efficiency, typically below 1%. With the accumulation of attempts, promising improvement has appeared and some groups have claimed to have measured around 10% external quantum efficiency (EQE) in BFO system. An interesting work done by Marin Alexe & Dietrich Hesse[57] showed that, by using photoelectric atomic force microscopy (PhAFM) combined with piezoresponse force microscopy (PFM), the conversion efficiency could be enhanced by seven orders of magnitude in BFO single domain crystal. They also demonstrated that, by contacting multiple PFM tips on sample surface, the photocurrent would increase with increasing number of tips, as shown in Fig. 1.8.

1.3.3 FePV effect in BFO thin film

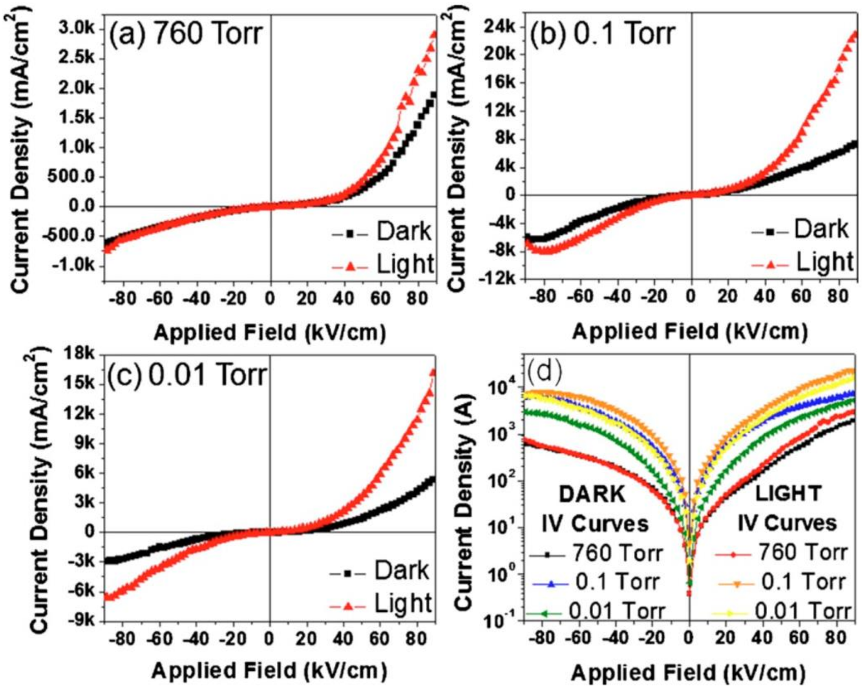

Fig. 1.9 Light and dark current density as a function of applied field for BFO/SRO/STO (111) films cooled at (a) 760 Torr, (b) 0.1 Torr, and (c) 0.001 Torr partial pressure of oxygen. (d) Log current density for the data shown in (a)–(c). Reprinted from S.R. Basu *et al.* [58].

Due to the simple fabrication process, work on BFO thin film structure is dominant in literatures [58][59][60][61][62][63][64][65]. The earliest work in BPV of BFO thin film was, to the best of our knowledge, done by S.R. Basu *et al.* [58] in 2008 (Fig. 1.9). In their work, the authors suggested an indirect bandgap of ~ 2.7 eV according to fitted absorption coefficient vs. photon energy, which was in consistent with previous simulation results, and they also identified an obvious photocurrent under 80 kV/cm bias field. Later work done by S.Y. Yang *et al.* [59] showed a zero-bias photocurrent density of 1.5 mA/cm^2, an open-circuit voltage of 0.8 V, and an external quantum efficiency of 10%. This prominent photovoltaic effect was explained by Schottky junction formed at the ITO/BFO interface. However, these two studies were conducted on samples with sandwiched structures, i.e. top electrode/BFO/bottom electrode/substrate, which has complicated the access of possible mechanism.

S.Y. Yang *et al.* [15] have proposed a new mechanism for photovoltaic effect in BFO thin film with symmetric in-plane electrode configuration. As we have mentioned above, with the help of strain engineering to separate stripe-like 71^o domain walls from random domain pattern, the authors observed that the photovoltaic effect is prominent when measurement was taken in vertical direction to domain walls, and negligible when measured parallel to domain walls (Fig. 1.4-1.5). Moreover, according to Kittel’s law, the width of domain is proportional to square root of film thickness[66]. Based on this law, the domain wall theory clearly explained the phenomenon that the open circuit voltage decreases with increasing film thickness. This work is of great importance; not only because it provides an alternative mechanism for BPV, but also due to its simple sample configuration that allows later reference and further investigation. A more market driven research of non-volatile memory device based on BFO thin film was presented by Rui Guo *et al.* [63] A prototype of 16-cell memory based on cross-bar architecture is shown in Fig. 1.10. Though the overall performance of BFO-based non-volatile memory device was not prominent better than other materials, this work provided a solid foundation for further exploration.

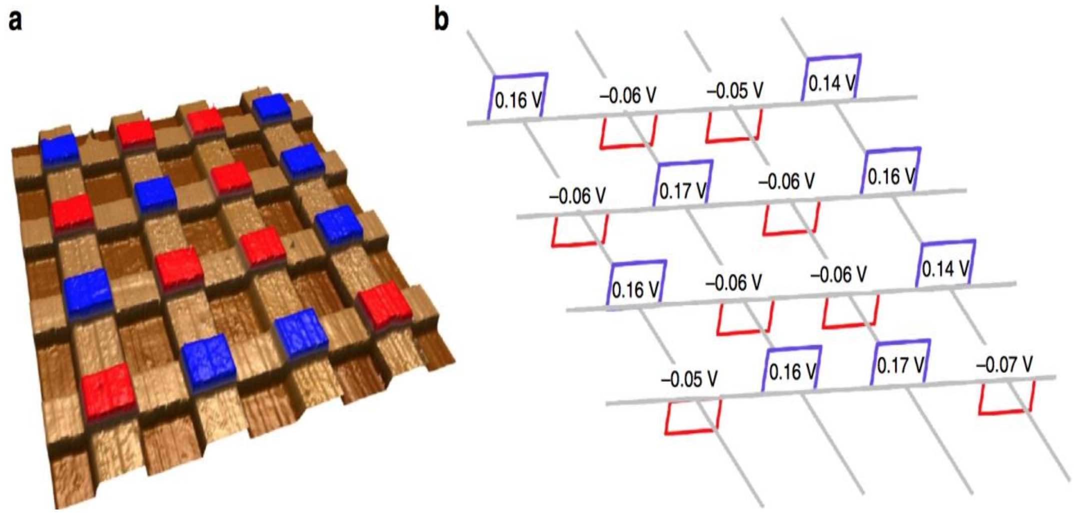

Fig. 1.10 Performance of a prototype 16-cell memory based on the cross-bar architecture. (a) Topography of the device with preset polarization direction. Blue: polarization up, red: polarization down. (b) V_{oc} of all 16 cells are indicated. These are measured under 20 mW cm^{-2} light. Reprinted from Rui Guo *et al.* [63]**.**

1.3.4 FePV effect in BFO nanowires

One-dimensional (1D) semiconductor nanowires are emerging as promising candidates for developing next generation photovoltaic cells due to their strong light absorption properties, which are a result of large surface areas and direct charge transport paths along the geometry of the wires[67][68]. K. Prashanthi *et al*. has investigated BFO single nanowire placed on Pt/Ti electrodes, and observed an obvious sub-bandgap photovoltage phenomenon (Fig. 1.11). The result can be attributed to the increased surface states resulting from the high surface-to-volume ratio for nanowires. This research is important to the development of FePV devices involving the BFO nanowire array for new generation solar cells.

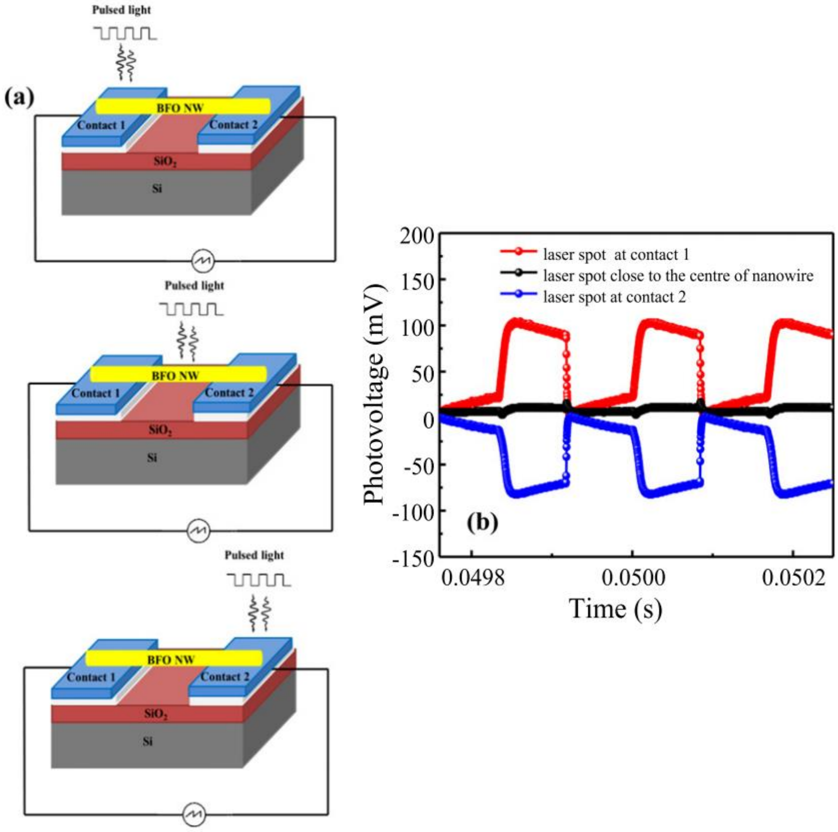

Fig. 1.11 Photovoltage response at different location on nanowire. Reprinted from K. Prashanthi et al. [69]

1.4 Outline of the thesis

A brief literature review is given in Chapter 1, concerning the historical development of FePV and its applications of BFO material.

Chapter 2 gives a brief introduction on those techniques that were employed in this study, including the deposition technique, the structural characterization techniques, and the photocurrent measurement setup.

In Chapter 3, the influences of secondary phases on BFO thin films are presented; and hence the fabrication conditions in our system have been optimized for large photovoltage and photocurrent.

In Chapter 4, the influences of electrodes on FePV effect of BFO thin film are examined. Gold and titanium electrodes were deposited on BFO thin film deposited under optimized conditions, and the I-V characterizations of photo-electric response and KPFM result confirm that Schottky and Ohmic contacts are built up at Au/BFO and Ti/BFO interfaces, respectively.

In Chapter 5, strain effect on FePV properties of BFO are examined. BFO thin films were respectively deposited on PMN-PT and LAO substrates to study their strain-dependent photovoltaic behavior. In addition, FePV effect in strain-free BFO nanofibers are also presented for comparison.

Chapter 6 gives the conclusions and future perspectives of this thesis.

Chapter 2. Experimental Methods

2.1 Introduction

This chapter provides a brief introduction on the techniques and facilities employed in this study. They include:

(1) Thin film deposition technique: Pulsed Laser Deposition (PLD). A KrF excimer laser with a wavelength of 248 nm and pulse duration of 25 ns (Lambda Physik COMPex 205) was used as laser source.

(2) Electrode patterning: DC magnetron sputtering, spin coating, oxygen plasma and photolithography were used for electrode patterning.

(3) Techniques for thin film structural characterization: X-ray diffraction (XRD), Scanning Electron Microscopy (SEM), Atomic Force Microscopy (AFM), and Transmission Electron Microscopy (TEM).

(4) Electrical characterizations: The ferroelectric properties were measured by the Precision Premier II Ferroelectric Tester. I-V curve was measured by Keithley 2410 sourcemeter.

(5) Photovoltaic measurement: The light source is a 375 nm laser with its maximum power density on sample surface of 20 mW/cm^2

2.2 Pulsed Laser Deposition

The pulsed laser was applied as a direct energy source for thin film fabrication since the discovery of laser[69][70]. The first experiment on pulsed laser deposition was conducted in 1960s. After that, several efforts were contributed to the technique in 1970s and 1980s. In late 1980s, due to the success on epitaxial deposition of high-temperature superconducting films, the pulsed laser deposition technique was then globally recognized as a fast and reproducible thin film growth method.

Compared with conventional film deposition techniques, e.g. thermal evaporation, molecular beam epitaxy (MBE), sputtering, metal-organic chemical vapor deposition (MOCVD), etc., laser ablation has the following major advantages[15][35][60][24][71][72][32]:

2 The target composition is directly transferred to the film, leading to stoichiometric deposition.

3 Tunable deposition rate can be realized by changing the frequencies of laser ablation.

Several weak points for current PLD technique also exist, including splashing of particulates onto the films. For a large-area growth, the uniformity of the film is not guaranteed during a PLD process. Thus, PLD technique is not quite suitable for large area thin film depositions.

2.2.1 Preparation of Ceramic Target

Throughout this work, three types of bismuth ferrite targets with different compositions have been used: $Bi_{1.2}FeO_3$, $BiFeO_3$ and $Bi_{0.8}FeO_3$. The target preparation was based on solid state reaction between metal oxides, which is widely employed in the preparation of ceramic targets for thin film deposition. Standard synthesis of ceramics in this project can be divided into several steps:

2 The starting materials (oxide powders) were weighted according to the chemical formula and mixed manually in an agate mortar assisted by ethanol for 2 hours, followed by ball-milling for 10 hours.

3 The powder was then totally parched in an oven and calcined in an alumina crucible at 780 ℃ for 1 hour to make the solid state reaction

happen.

4 The calcined powder was then grounded again in alcohol using zirconia balls in the ball-milling machine for 10 hours.

5 Before pressing the calcined powder into pellets, 5 wt% PVA (polyvinyl alcohol) was homogeneously mixed with the powder as binder for granulation in an agate mortar for 2 hours.

6 A one-inch diameter stainless steel pressing mold was filled by the calcined powder. A uniaxial pressure of ~30 MPa was added for 5 min to drive out the excess air inside the powder. After that, the ceramic powder became a densely packed disc.

7 The organic binder PVA in the green sample was completely burnt out at around 600 ℃ for 2 hours.

8 After complete removal of PVA, the pellets with different compositions were sintered at 820 -850 ℃ for 1 hour, followed by a rapid quenching to avoid Bi evaporation[73].

9 Dense and hard ceramic pallets as the targets of thin film deposition were formed after surface polishing with sand papers.

2.2.2 Ablation Process

Pulsed-laser deposition (PLD) is a physical vapor deposition technique where a high-power pulsed-laser beam is focused inside a vacuum chamber by lens to evoke a high density plasma vapor by thermal evaporation in a very short time. The ablated plasma will then transport forward to target surface and form a plume that is comprised of clusters of atoms, molecules, electrons, and ions. Before being deposited onto the hot substrate, these particles may involve in very complex reactions with surrounding gas molecules if the deposition is performed under a background gas like oxygen. Figure 2.1 is a schematic diagram of the PLD system in this project, where the whole setup includes a laser beam source and a stainless steel vacuum chamber with a rotating target holder and a substrate stage whose temperature is program controlled. The laser pulses are focused through an optical system to ablate the target. Multiple targets can be used to enable the growth of alternating layered thin films.

In the laser ablation process, a KrF excimer laser (with wavelength of 248 nm, pulse duration of 25 ns, energy in the range of 0.25 to 0.4 J before the focusing lens and a frequency of 1 -10 Hz, Lambda Physik compex 205) is used to ablate the target.

During deposition, the target is kept rotating so that the target will not melt due to successive incidence of laser pulses on the same point. The ablation process takes place in a vacuum chamber - either in vacuum or in the presence of some background gas. In the case of oxide films, oxygen is the most common background gas.

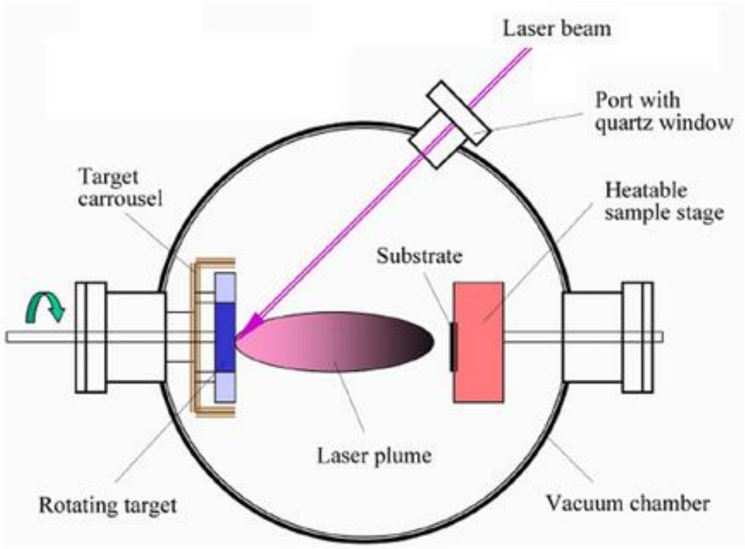

Fig. 2.1 Schematic setup of pulsed laser ablation in a vacuum chamber.

2.2.3 Deposition Process

During the deposition process, as mentioned before, high energy pulsed laser ablates material from the target surface, then atoms, ions, and molecules pass through the vacuum and finally reach the substrate surface, either being elastically reflected out of or captured on the substrate surface. Those captured particles, called adatoms, would be subjected to desorption, adsorption and diffusion on the surface and steps, and eventually nucleate and grow into a uniform film.

However, the high energetic species ablated from the target can also bombard the substrate and re-sputter off atoms from the deposited thin film, causing damage to the surface of the sample. Consequently, a collision region will be formed due to the sputtered species and particles, which serves as a source for condensation of particles. Thus, to ensure the high quality of final thin films, several influential factors, such as, substrate temperature, working pressure (oxygen partial pressure for oxide thin films), laser energy density, distance between target and substrate, laser frequency and background pressure should be taken into consideration. The complexity of interaction between these factors to each other makes it difficult to optimize the deposition conditions for a specific material. A practical method is to fix several of these factors throughout the whole experiment and only two or three factors are allowed to be varied. The experiment details are presented in the following part.

2.2.4 Deposition Parameters

In this project, BFO/LSMO/substrate or BFO/substrate thin films were deposited at an oxygen pressure of 50-100 mTorr for BFO and 300 mTorr for LSMO

(LaSrMnO$_3$). Single crystal substrates SrTiO3, LaAlO3 and PMN-PT are supplied by HeFei Crystal Materials Co., Ltd.. Before loaded into the chamber, substrates were treated with an ultrasonic bath in acetone, ethanol, and DI water, consecutively, to get rid of the organic contaminations. The pressure inside the vacuum chamber was detected by a ZDF-I vacuum gauge system (Chengdu Chenghua Electronic Instrument Factory), which combines a manometer and an ionization gauge for low and high vacuum monitoring, respectively. The substrate temperature was varied from 600 to 700 ℃ for different thin films, monitored by a chromel-alumel thermocouple. Distance between the target and the substrate was fixed at 5 cm. Pre-ablation was necessary to clean the target surface. A laser energy density of ~1 J/cm^2 for BFO and ~2 J/cm^2 for LSMO and a laser repetition rate of 1 -10 Hz were used during deposition. An additional in-situ annealing process under 5 Torr oxygen gas after deposition is essential for all samples to get a better degree of crystallization before they were finally cooled down to room temperature at a rate of 5 ℃/min.

2.3 Characterizations of Thin Films

2.3.1 X-ray Diffraction

X-ray diffraction (XRD) is a versatile, non-destructive technique that reveals detailed information of crystallographic structure of natural and manufactured materials. In this study, X-ray diffraction measurements were carried out in on a Rigaku Smartlab high resolution X-ray diffractometer (HRXRD) with a 9 kW rotating anode X-ray generator, using a Cu Kα radiation at a wavelength λ = 1.540562 Å. We have performed a standard set of XRD measurements for a thorough characterization of epitaxial thin films, including 2θ-ω scan, rocking curve and Phi scan.

2.3.1.1 Bragg’s Law

The basic principle of crystal lattice measurement by XRD is based on diffraction of X-rays which have a wavelength of the same order as the lattice parameters of a crystal, i.e. Bragg’s Law. When parallel incident x-rays approach to the crystal lattice, the periodic “planes” of lattice will elastically “reflect” the x-ray in the same way as a mirror reflects light, as shown in Fig. 2.2. Due to elasticity, the absolute value of the outgoing wave vector, will keep unchanged, but the phase at the wave frontier will be different due to different paths diffracted by consecutive planes 1’, 2’, 3’ … Therefore, for a specific incident angle θ, the strongest interference of outgoing waves will occur according to Bragg’s Law:

$$\boldsymbol{\lambda = 2d_{hkl}\ \sin\theta_{hkl}} \qquad (1)$$

Here hkl indicates the Miller indices of parallel planes (h k l) and d_{hkl} is the d-spacing of these planes. Since the λ doesn’t change for elastic scattering, there is a one to one correspondence between θ_{hkl} and d_{hkl}.

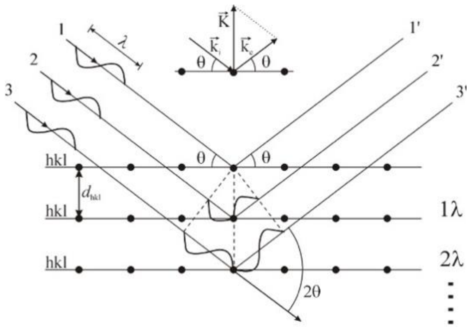

Fig. 2.2 Principle of X-ray diffraction for crystal structure characterization.

2.3.1.2 X-ray Diffraction of Thin Films

X-ray Diffraction is a crucial technique for investigation of epitaxial thin films, since it can provide detailed information on crystal structure of thin films, such as whether the resulting film is relaxed or not. Compared with powder sample, the principle for thin film is nothing more than Bragg's Law, but some technical considerations need to be taken to get an accurate measurement.

Unlike powder sample, the XRD pattern of a thin film is very sensitive to its placement on the sample holder. For common θ-2θ scan, the position of light source and light detector with respect to sample are always symmetric and will change in the same pace. However, if the surface plane of thin film is not placed horizontally, such as the tilt of sample caused by adhesive glue, then, in the θ-2θ scan, Bragg diffraction condition will not be satisfied. In this case, we should preset an offset value to correct the tilt angle and use 2θ-ω scan. By 2θ-ω scan, the position of light source and light detector with respect to sample are not symmetric, but in a manner of θ' = θ ± 2*offset. Fig. 2.3 shows the principle of 2θ-ω scan.

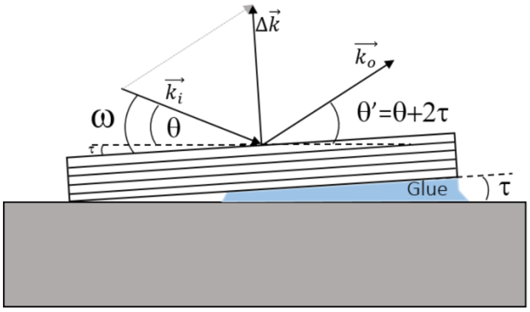

Fig. 2.3 Schematic diagram of 2θ-ω scan when the sample is tilted by τ.

2.3.1.3 2-Theta scan, Omega scan and Phi scan

Beside 2θ-ω and θ-2θ scans, there is another important scan called Omega scan. When applying Omega scan, the positions of X-ray tube and light detector are fixed while the sample plane is moved in a small range, typically within several degrees. The movement of the sample is much like rocking around the Bragg peak so that the Omega scan is often referred to rocking curve. The full width at half maximum (FWHM) of rocking curve is a good indicator of the quality of the resulting thin film: the smaller the FWHM value, the better the epitaxy of thin film. Fig. 2.4 (a) shows the working principle of Omega scan, and the broadening of the rocking curve represents that curvature or deviation in crystallographic orientation happens in the thin film, as shown in (b).

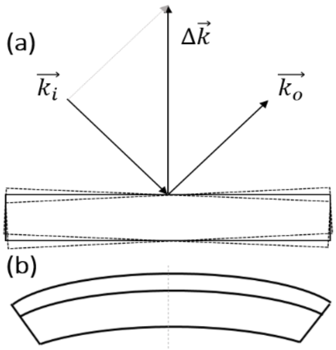

Fig. 2.4 (a) Working principle of Omega scan; (b) curvature of thin film would cause broaden of rocking curve.

Another technique that is important for thin film characterization is Phi scan. Phi scan is similar to Omega scan, but is different in that when applying the Phi scan, the sample is rotated around certain axis by 360 degrees, instead of “rocking”. Normally, it is not appropriate to apply Phi scan to planes which are parallel to substrate surface, like (0 0 1) plane on [0 0 1] orientated substrate, because this would result nothing but a flat baseline. If the lattice of the resulting thin film is cubic, for example, when we rotate the film along [1 0 1] axis and fix the X-ray tube and light detector at appropriate position, there should be only four peaks appeared in the Phi scan, as shown in Fig. 2.5 (a).

The last but not the least important scanning method is 2-theta scan. In 2-theta scan, the X-ray tube is fixed at certain place, normally about several degrees for small angle incidence, and the light detector moves, as shown in Fig. 2.5 (b). The 2-theta scan is very useful when the thin film is polycrystalline and the substrate signal is not desired.

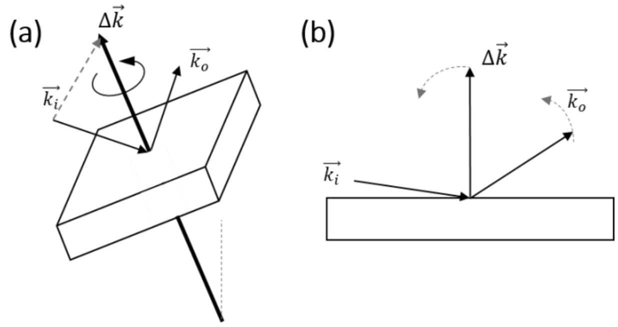

Fig. 2.5 Schematic diagram of working principles for (a) Phi scan; (b) 2-Theta scan.

2.3.1.4 Bragg’s Law in Reciprocal Space

In crystallography, the crystal can be abstracted as a periodic lattice in 3-demesion. For every real space, i.e. an abstract lattice of crystal, there is a conjugated space that represents its momentum lattice, and we call it reciprocal space. The detailed explanation of reciprocal space can be found in many excellent text books. Fig. 2.6 shows a hyperplane of reciprocal space of an epitaxial thin film. The triple digits beside each point, for example, 006, is the mark of diffraction maximum of (0 0 6) plane in thin film.

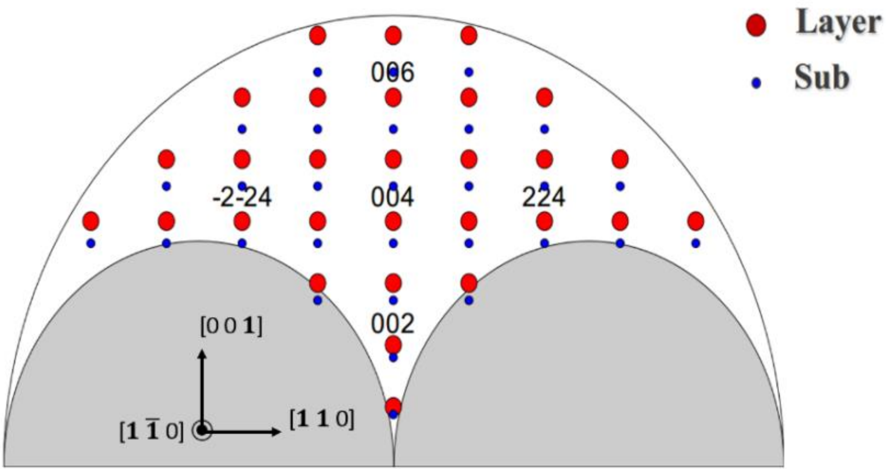

Fig. 2.6 Schematic diagram for reciprocal space. The coordinate at the left bottom shows the direction in this hyperplane of reciprocal space.

In Fig. 2.3-2.5, $\overrightarrow{k_\iota}$ and $\overrightarrow{k_o}$ are wave vectors of incident light and outgoing light. As we mentioned above, the light is elastically scattered by the crystal so that $|\overrightarrow{k_\iota}| = |\overrightarrow{k_o}| = 2\pi/\lambda$, but the change of wave vector $|\Delta\vec{k}| \neq 0$, since the propagating direction of incident light is changed. When Bragg's condition is met, i.e. $\lambda = 2d_{hkl} \sin\theta_{hkl}$, we will have:

$$\left|\Delta\vec{\boldsymbol{k}}_{\boldsymbol{hkl}}\right| = \boldsymbol{2} * \left|\overrightarrow{\boldsymbol{k}_\iota}\right| * \sin\boldsymbol{\theta}_{\boldsymbol{hkl}} = \boldsymbol{2} * \boldsymbol{2\pi}/\lambda * \sin\boldsymbol{\theta}_{\boldsymbol{hkl}} = \frac{\boldsymbol{2\pi}}{\boldsymbol{d}_{\boldsymbol{hkl}}} \qquad \textbf{(2)}$$

In reciprocal space, $\Delta\vec{k}_{hkl}$ is a vector pointing from the origin to the diffraction maximum point. For example, if we consider plane (0 0 2) and (0 0 6), then

$\left|\Delta\vec{k}_{002}\right| = \frac{2\pi}{d_{002}} = \frac{2\pi}{3*d_{006}} = \frac{1}{3}\left|\Delta\vec{k}_{006}\right|$, and since $\Delta\vec{k}_{00l}$ all pointing in the same direction, so $\Delta\vec{k}_{002} = \frac{1}{3}\Delta\vec{k}_{006}$.

When we perform 2θ-ω scan starting from 0 to 90 degree, the $\Delta\vec{k}$ will stretch from the origin straight up, as shown in Fig. 2.7. The red dots represent thin film diffraction maxima and blue dots represent substrate diffraction maxima in Fig. 2.7. The red dots are intentionally drew bigger than the blue dots because normally the epitaxial thin film isn’t one hundred percent perfect and defects will broaden and smear the shape of diffraction points. Whenever $\Delta\vec{k}$ meets a red dot or a blue dot, it will become $\Delta\vec{k}_{hkl}$, and a diffraction peak will appear.

The situations of Omega, θ-2θ and 2θ scans are slightly different compared with that of 2θ-ω scan. In Omega scan, $\left|\Delta\vec{k}\right|$ doesn’t change (please refer to Fig. 2.4) so that $\Delta\vec{k}$ actually moves like sweeping across a fan area, not a straight line in 2θ-ω scan, as shown in Fig. 2.7. In θ-2θ scan, if a tilt angle exists, the $\Delta\vec{k}$ will be deviated from that in 2θ-ω scan. As for 2θ scan, the magnitude and direction of $\Delta\vec{k}$ will simultaneously change with the increasing scanning angle and an irregular curve will be formed.

As we mentioned above, understanding different scanning modes in the frame of reciprocal space lattice is easy and straight forward. That is reason why X-ray diffraction technique is so important for thin film characterization.

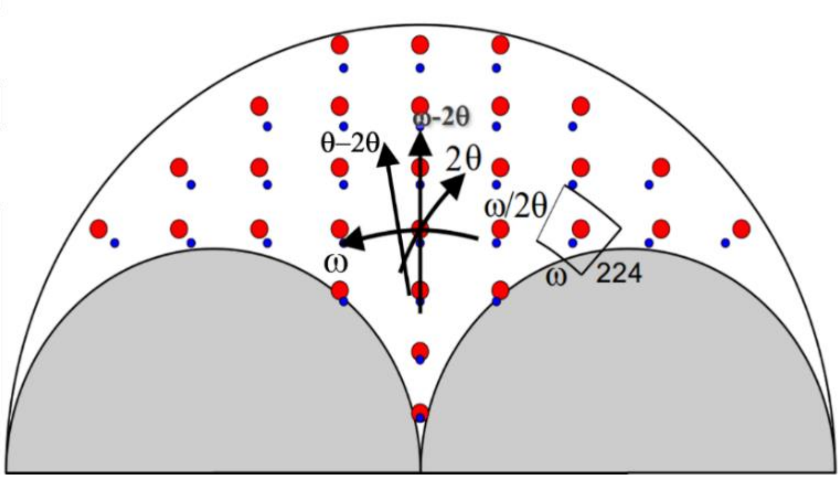

Fig. 2.7 Scan paths for different scan modes in reciprocal space of an epitaxial thin film. Red and blue dots represent thin film diffraction maximum and substrate diffraction maximum, respectively.

2.3.1.5 Reciprocal Space Mapping

By a combination of 2θ-ω and Omega scans, we can get complete information of the diffraction pattern in reciprocal space, which is called reciprocal space mapping (RSM). In Fig. 2.7, RSM scanned area of point [2 2 4] is indicated by a black square. For an ideal single crystal, each point in reciprocal space has a clear edge and round shape; while for a low quality crystal, the edge of point is blurred and the shape is deformed. In Fig. 2.8, four typical shapes that can be frequently observed in RSM measurement are shown.

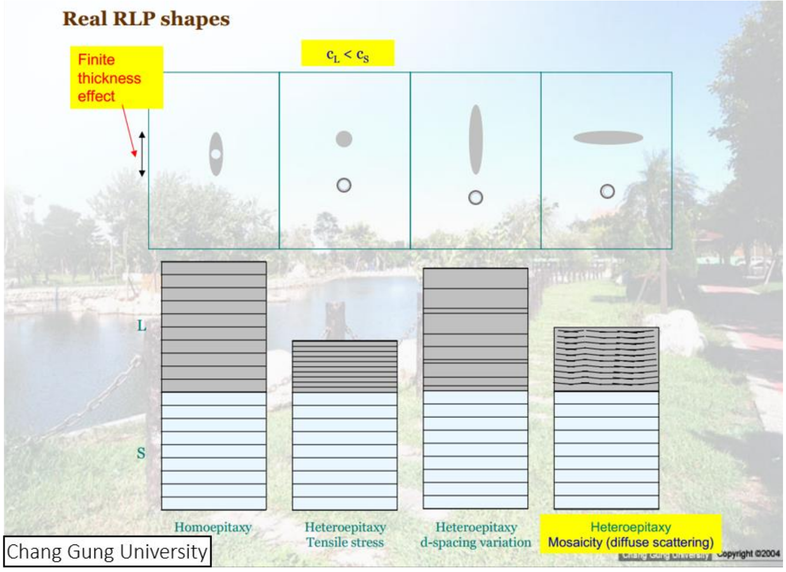

Fig. 2.8 Four typical shapes that can be frequently seen in RSM measurement. The round hollow circle represents substrate diffraction spot and the grey area indicates diffraction map of resulting film.

2.3.2 Raman Spectroscopy

Raman Spectroscopy is a spectroscopic technique used to observe vibrational, rotational, and other low-frequency modes in a system. When a sample is illuminated by monochromatic light, the molecule in the sample could have elastic or inelastic interaction with photons, the former behavior is Rayleigh scattering and the later one contains Raman scattering and infrared scattering. The selection rule for Raman spectroscopy is that only a change of polarisability of a molecule can be observed, and because this relates to different vibrational transitions from those in Infrared spectroscopy, the two techniques are complementary. Raman spectroscopy is widely used as an auxiliary method to identify crystal structure of matters[42][74][75][76][77][78][79].

HORIBA HR800 with the excitation wavelength of 488 nm was used to extract Raman vibration information. A 100× objective was used to focus the laser beam and to collect the Raman signal. The size of the laser spot is about 1 μm.

2.3.3 Scanning Probe Microscopy

Scanning Probe Microscopy (SPM) has a number of different modalities such as atomic force microscopy (topography imaging), piezoresponse force microscopy (ferroelectric domain imaging), and magnetic force microscopy (magnetic domain imaging), etc. The first AFM was designed in 1986 by Binnig and his colleagues. In early 1990s, the AFM techniques began to be widely used in commercial applications. It is a nondestructive technique used for characterization of the surface topography of thin films, polymer coatings, and single-crystal substrates. Except for surface morphology depicted by atomic force microscopy, piezoresponse force microscopy (PFM) is a powerful tool to characterize the fine ferroelectric domain configuration and switching behavior in a local area of ferroelectric and multiferroic thin films. Fig. 2.9 shows the principle parts of a PFM. The SPM used in this work is Bruker Nanoscope 8 with tapping mode and electric contact mode.

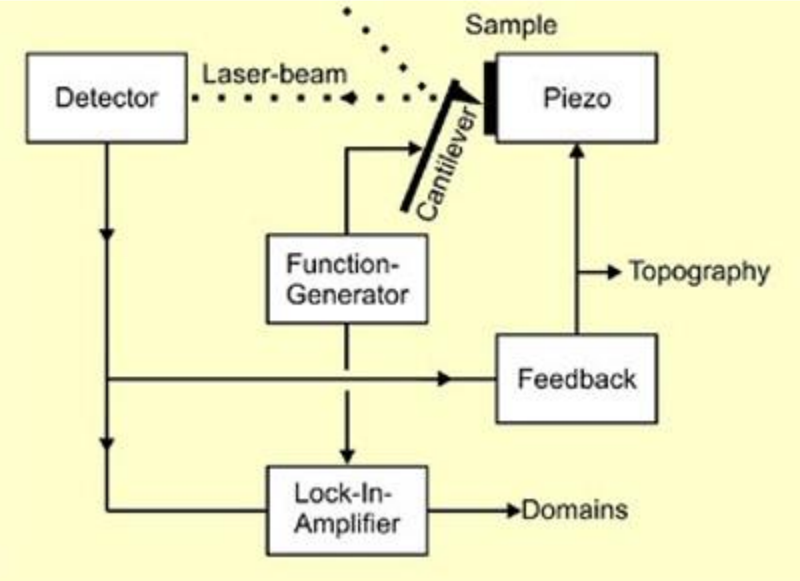

Fig. 2.9 Schematic diagram of working principle of a PFM.

2.3.4 P-E Loop Measurement

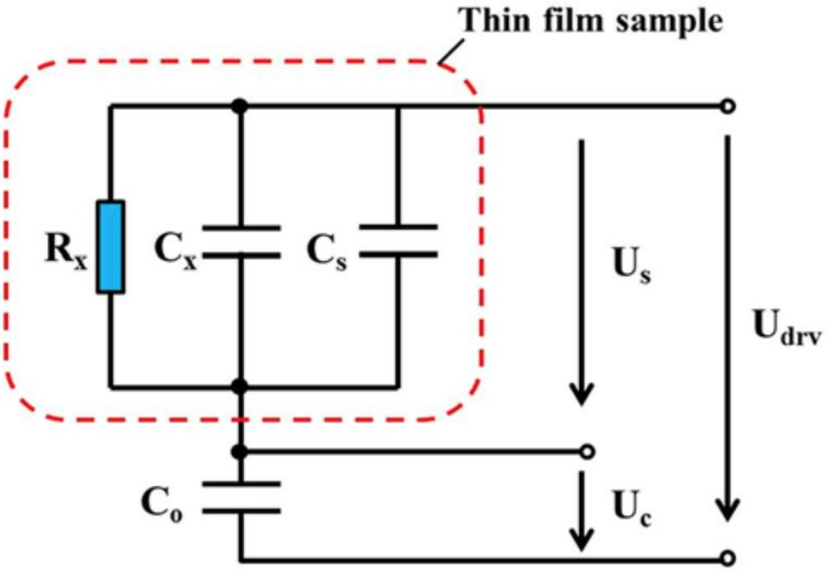

Fig. 2.10 Schematic diagram of Sawyer–Tower circuit for thin film test. Reprinted from Ying Wang[19].

Hysteresis behavior can be found in many natural or artificial systems, and is often associated with irreversible thermodynamic change. Electrical hysteresis typically occurs in ferroelectric material when the sample is below its Curie temperature (T_c). A typical Sawyer–Tower circuit, which is shown in Fig. 2.10, is essentially used for experimental ferroelectric hysteresis loop measurement below T_c. The basic principle is that $P = \frac{Q}{A} = \frac{U_C C_0}{A}$, and A is the contact area between electrodes and sample. For the test, a metal/ferroelectric/metal capacitor should be fabricated. Pulsed signals in square-wave or sine-wave forms are usually used for the study of polarization switching. Ferroelectric information including the remnant polarization P_r, the spontaneous polarization P_s, and the coercive field E_c can be obtained.

In this project, the electric field dependent electrical displacement of the BFO/LSMO/substrate is studied by measuring the ferroelectric hysteresis loops at 1 kHz at room temperature using a ferroelectric tester (Precision Premier II).

2.3.5 Photo-electric Response Measurement

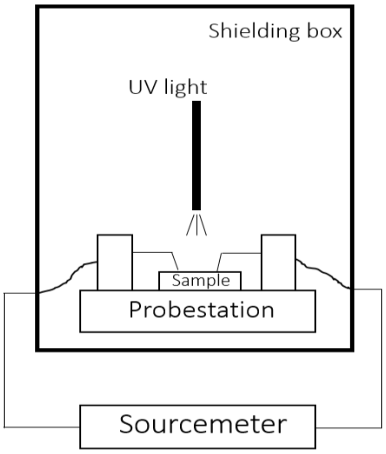

Fig. 2.11 Schematic diagram of the setup for photocurrent measurement.

In a photo-electric response measurement, the sample is placed on a probe-station inside a shielding box. The light source is a 375 nm laser with its maximum power density on sample surface of 20 mW/cm^2. The induced current was recorded by a

Keithley 2410 sourcemeter and the data was recorded by a home-made LabVIEW program. Fig. 2.11 shows a schematic diagram of our setup for photocurrent measurement.

Chapter 3. Deposition and characterizations of epitaxial BFO thin films

3.1 Introduction

As one of the few room temperature multiferroics, BFO has been intensively investigated. However, for a long time, there are practical difficulties in preparing BFO single crystals and ceramics, which prevent further exploration of its application potentials. For example, the high volatility of bismuth at high temperature (typically above 650 ^{o}C) will often cause non-stoichiometric crystals or ceramics. Fortunately, with help of the fast development of thin film deposition techniques, these problems are improved greatly by decades of effort. In 2003, epitaxial BFO thin film was successfully grown on STO substrates, and a huge electrical remnant polarization of 58 μC/cm^2 was reported for the first time. Since then, intensive studies have been conducted to uncover the relationship between thin film preparation conditions and its physical properties.

Among all of the thin film deposition techniques, PLD is an advanced technique for thin film fabrication with unique advantages such as accurate controlling of chemical composition in the resulting film by varying target composition, and tunable deposition rates by changing laser frequency[80]. There are several deposition parameters that can affect the quality of PLD-deposited thin films, i.e. the substrate temperature, the working pressure (oxygen partial pressure for oxide thin film), the laser energy density, the distance between the target and the substrate, the laser frequency (molecular flux rate) and the background pressure. For BFO thin film, a pure phase epitaxial sample can be only obtained within a small parameter ‘window’, and deviation from the optimized parameters will introduce secondary phases that are influential to the overall physical properties.

H. Béa *et al.* explored the influence of deposition pressure and temperature on the growth of BFO thin films prepared by PLD[81]. The authors reported that pure BFO phase was formed closed to P = 10^{-2} mbar and T = 580 ^{o}C. At lower temperature or higher pressure, Bi_2O_3 precipitates were detected while at lower pressure and higher temperature, Fe_2O_3 formed. Based on this work, Lu You *et al.* investigated the influence of oxygen pressure on the growth of BFO thin films and the corresponding electrical properties[82][83]. It was found that the ferroelectric properties and domain structure were closely related to the Bi/Fe ratio, which was changed in response to varying of oxygen pressure even within the window where pure phase BFO thin film could be obtained. The authors proposed that, for films grown under oxygen pressure below 20 mTorr, high concentration Bi vacancies (V_{Bi}) and oxygen vacancies (V_O) may form V_{Bi} - V_O defect-dipole complexes, which will induce randomly aligned internal field that would reduce the overall polarization. For films grown under 20 mTorr or above, the leakage current density is increased by about two to three orders of magnitude, due to conductive Bi_2O_3 phase rather than the intrinsic properties of BFO. Another work done by Rui Guo *et al.* [84] studied the influence of target composition on the ferroelectric properties of BFO thin film, and it was observed that the domain structure varied greatly by reducing Bi content from $Bi_{0.8}FeO_3$ to $Bi_{0.4}FeO_3$ in the target.

In recent years, above band-gap photovoltage was observed in BFO epitaxial thin film, and a great many of papers were published in this area, as discussed in Chapter 1. However, the influence of deposition parameters on photovoltaic properties of BFO thin film is still lack of investigation. We believe that this issue is worthy of discussion, since the preparation conditions determine the electrical and ferroelectric properties of BFO thin film, which are highly related to the photovoltaic behavior. In this chapter, BFO thin films are prepared under different deposition conditions, and their photovoltaic properties are examined by in-plane electrode configuration.

3.2 Experimental details

To explore the effects of ablation rate and oxygen pressure on thin film quality and photovoltaic behavior, BFO thin films (100 nm in thickness) were deposited on STO single crystal substrates along [0 0 1] direction by PLD. Three targets with different compositions were prepared in advance, i.e. $Bi_{0.8}FeO_3$, $BiFeO_3$ and $Bi_{1.2}FeO_3$. During PLD depositions, the substrate temperature was kept at 700 ^oC and maintained for 20 mins after laser ablation. Then it was slowly decreased to room temperature at a rate of 5 ^oC/min. A KrF excimer laser was used as the ablation source with its energy density fixed at 0.7 J/cm^2. The ablation rate was varied from 3 to 10 Hz, and the oxygen pressure was also changed from 6 to 13 Pa. The substrate was placed 5 cm away from the target to allow full interaction between Fe^{3+}, Bi^{3+} and the oxygen atoms before the plasmonic clusters arrived at the substrate.

In the following context, different samples are marked by abbreviations of their deposition parameters for convenience. The optimized sample is marked as 10 Hz & 13 Pa, and other samples are marked by deposition parameter which is different than the optimized sample. For instance, the sample prepared by ablation of $Bi_{0.8}FeO_3$ target is marked as $Bi_{0.8}FeO_3$, or 0.8; and 6 Pa & 3 Hz is short for film deposited under oxygen pressure of 6 Pa, laser frequency of 3 Hz and by ablation of target $BiFeO_3$.

3.3 Structure characterizations

3.3.1 XRD analysis

Fig 3.1 shows the $2\theta-\omega$ profiles of samples deposited under different deposition conditions, and a pure phase BFO thin film was obtained under 10 Hz & 13 Pa condition. By lowering the laser frequency from 10 to 3 Hz, Bi_2O_3 secondary phase appears, while a pure phase sample can be re-obtained by lowering both the ablation rate and oxygen pressure to 3Hz and 6Pa, respectively, as shown in Fig. 3.1 (a). Therefore, it implies that decreasing ablation rate and increasing oxygen pressure, or decreasing temperature have the same function in forming Bi_2O_3 secondary phase, as discussed in reference[81]. However, the BFO (0 0 1) peak shifted slightly towards the STO (0 0 1) peak in sample 3 Hz & 6 Pa, which indicates that the film is relaxed from the constraint by substrate.

Fig. 3.1 (b) shows the $2\theta-\omega$ profiles of BFO/STO thin film prepared by ablation of different targets while the oxygen pressure and ablation rate are fixed at 13 Pa and 10 Hz, respectively. As observed from the figure, impurity phase existed in the sample from $Bi_{1.2}FeO_3$, which is caused by excessive bismuth in the target. Fig. 3.1 (b) also indicates that the crystal structure of sample $Bi_{0.8}FeO_3$ is similar to sample 3 Hz & 6 Pa (shown in Fig. 3.1 (a), the red curve); both samples exhibited a relaxed structure while no secondary phase can be found.

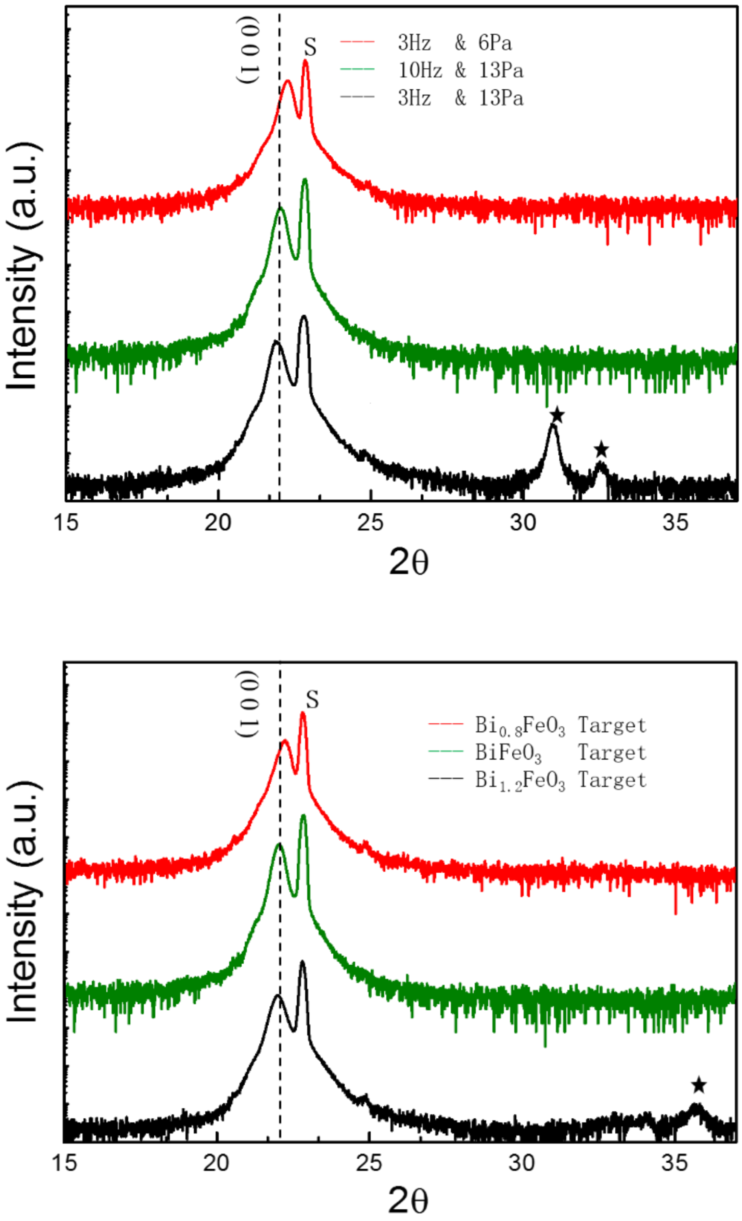

Fig. 3.1 2θ-ω profiles of BFO/STO thin films deposited (a) under various oxygen pressures and ablation rates; (b) by ablation of different targets. The stars indicate Bi_2O_3 phase. The dashed line shows the position of BFO (0 0 1) peak. S denotes the diffraction peak from the STO substrate.

Fig. 3.2 shows the phi scan and omega scan of the films $Bi_{0.8}FeO_3$, 3 Hz & 6 Pa and 10 Hz & 13 Pa, and Table 3.1 lists the detailed information of their rocking curves. As observed, even though all the three samples showed periodic peaks in the phi scan, the FWHM of the film $Bi_{0.8}FeO_3$ and 3 Hz & 6 Pa is prominently larger than that of the film 10 Hz & 13 Pa, which indicates that the film $Bi_{0.8}FeO_3$, 3 Hz & 6 Pa is relatively poor in epitaxial quality.

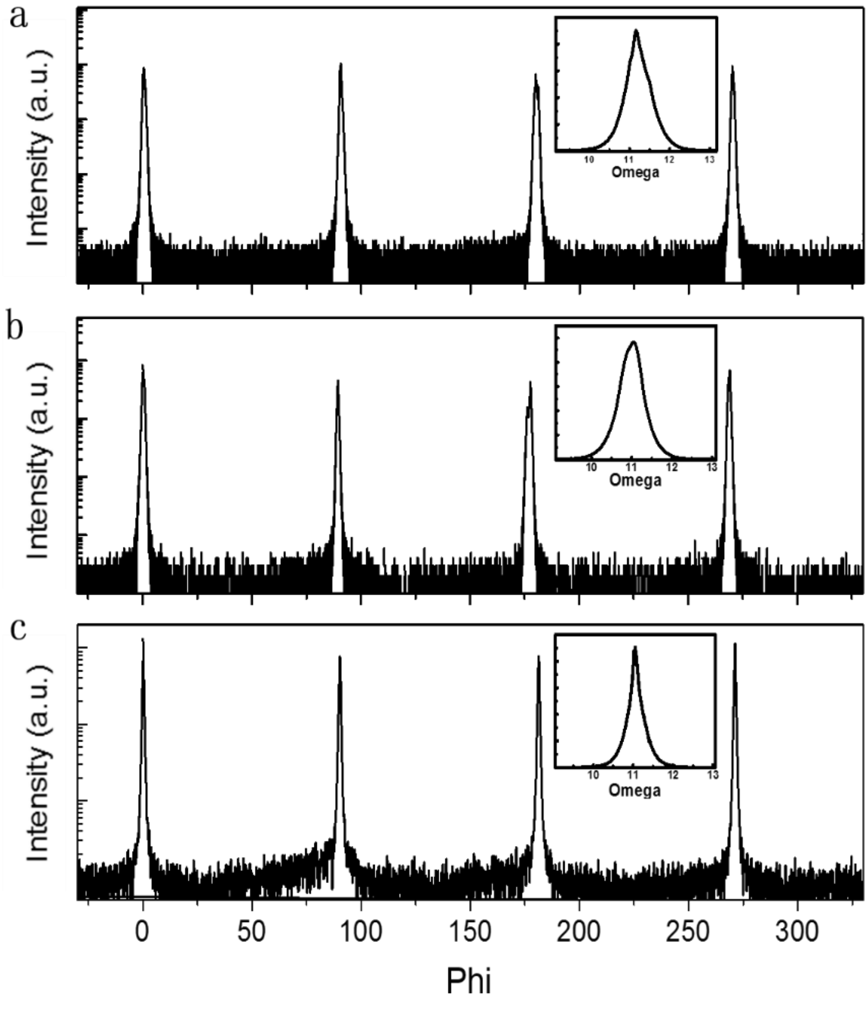

Fig. 3.2 Phi scan of BFO/STO thin film along the (1 0 1) direction. Each figure corresponds to the deposition condition listed in Table 1. Rocking curves of (0 0 1) peak are shown as the insets.

The poor epitaxy and contraction of lattice parameter in samples 3 Hz & 6 Pa and $Bi_{0.8}FeO_3$ are probably caused by two reasons. First, when changing the deposition parameters from 10 Hz & 13 Pa to 3 Hz & 6 Pa, the thin film growth mode has shifted from step flow model (sample 10 Hz & 13 Pa) to island model (sample 3 Hz & 6 Pa), which is confirmed by AFM image in next section. Second, there are bismuth vacancies in sample 3 Hz & 6 Pa and $Bi_{0.8}FeO_3$, which cause the decrease of lattice parameter. Although no Fe_2O_3 phase was detected in the $2\theta-\omega$ profile of both samples, the Bi/Fe ratio measured by EDS confirms bismuth deficiency in the films 3 Hz & 6 Pa and $Bi_{0.8}FeO_3$, as listed in Table 2. It should be noted that the EDS result is averaged over five measurements at different spots on the films.

	a. $Bi_{0.8}FeO_3$	b. 3 Hz 6 Pa	c. 13 Pa 10 Hz
Peak Position	**11.14º**	**11.18º**	**11.04º**
d-(0 0 1)	**3.988**	**3.974**	**4.024**
FWHM	**0.687**	**0.635**	**0.344**

Table 3.1Summary of the corresponding XRD rocking curves for BFO/STO thin films at (0 0 1) direction prepared under different conditions.

	$Bi_{0.8}FeO_3$	3 Hz 6 Pa	13 Pa 10 Hz	13 Pa 3 Hz
Bi/Fe ratio	**0.888**	**0.941**	**0.998**	**1.053**

Table 3.2 EDS result for BFO/STO thin films at (0 0 1) direction prepared under different conditions.

3.3.2 AFM Image

In thin film deposition process, the growth mode is very critical to the quality of produced films. There are three commonly observed surface growth modes: step flow (characterized by steady advance of the steps in the vicinal direction), step bunching (characterized by the crowding of the steps and the creation of large terraces), and island formation (characterized by layer-by-layer growth via nucleation and coalescence of islands). In most cases, step flow is the desired mode of thin film growth[85].

Fig. 3.3 presents the AFM images for films 10 Hz & 13 Pa, 3 Hz & 6 Pa, 3 Hz & 13 Pa, and $Bi_{0.8}FeO_3$. As observed in these figures, we can conclude that the growth mode of sample 10 Hz & 13 Pa is step flow, and the growth mode of other samples is island formation.

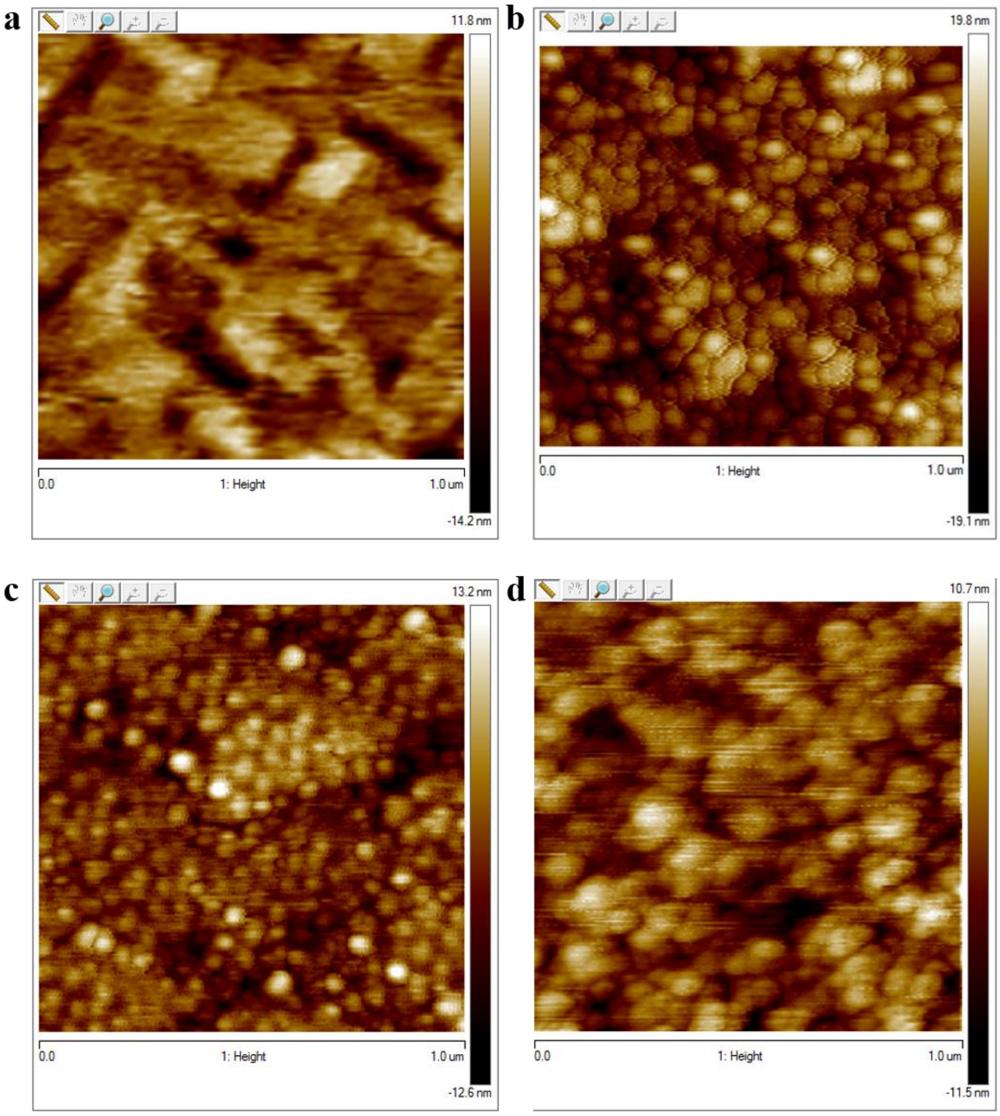

Fig. 3.3 AFM image of sample (a) 10 Hz & 13 Pa; (b) 3 Hz & 6 Pa; (c) 3 Hz & 13 Pa; (d) $Bi_{0.8}FeO_3$.

3.3.3 Raman Spectroscopy

The crystal structure of BFO thin films deposited on STO substrates reported in literature varied from tetragonal, monoclinic to rhombohedral. In order to confirm the lattice symmetry of our samples, Raman spectroscopy with backward scattering were employed. Fig. 3.4 shows the Raman shifts of BFO thin films deposited under different conditions. As observed, these four films are almost identical to each other with peaks of A_1 modes at 141 cm^{-1}, 175 cm^{-1}, 222 cm^{-1}. This Raman spectroscopy confirms all of our samples belong to a M_A type monoclinic structure in the *Cm* space group[86], which has none-zero projection of spontaneous polarization onto (0 0 *h*) plane.

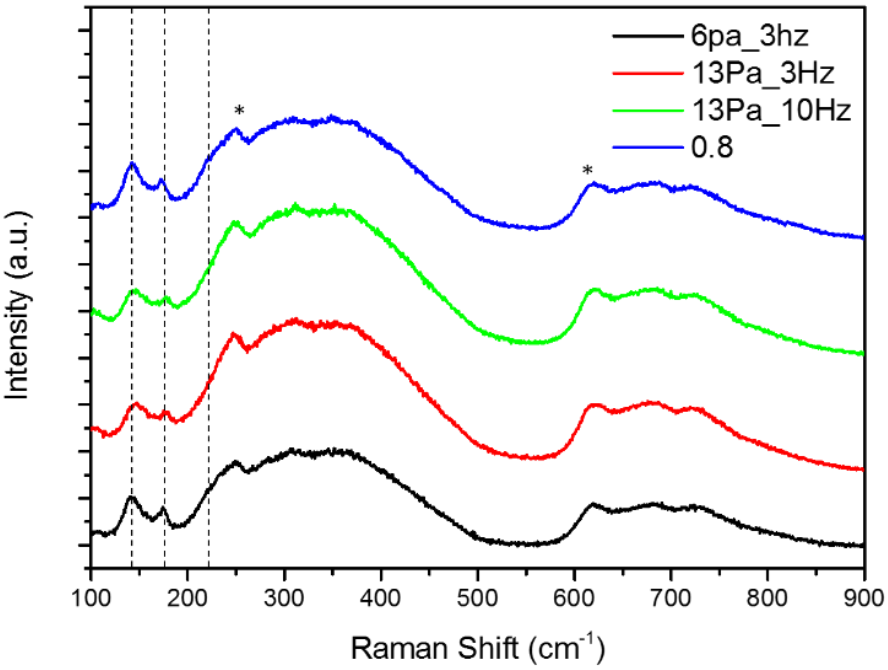

Fig. 3.4 Raman profiles of BFO thin films. Dashed lines indicate the rhombohedral phase of BFO and stars show peaks of STO.

3.4 Photoelectric properties of BFO thin films prepared under different conditions

In this section, the photoelectric behaviors of BFO thin film prepared under different conditions are examined. To measure the photocurrent and dark current, in-plane electrode configuration was employed. Gold/Titanium electrodes were deposited by magnetron sputtering with 5 μm of separation distance. A schematic figure is shown in the inset of Fig. 3.5. The setup for photoelectric measurement is presented in Chapter 2.

3.4.1 Leakage current

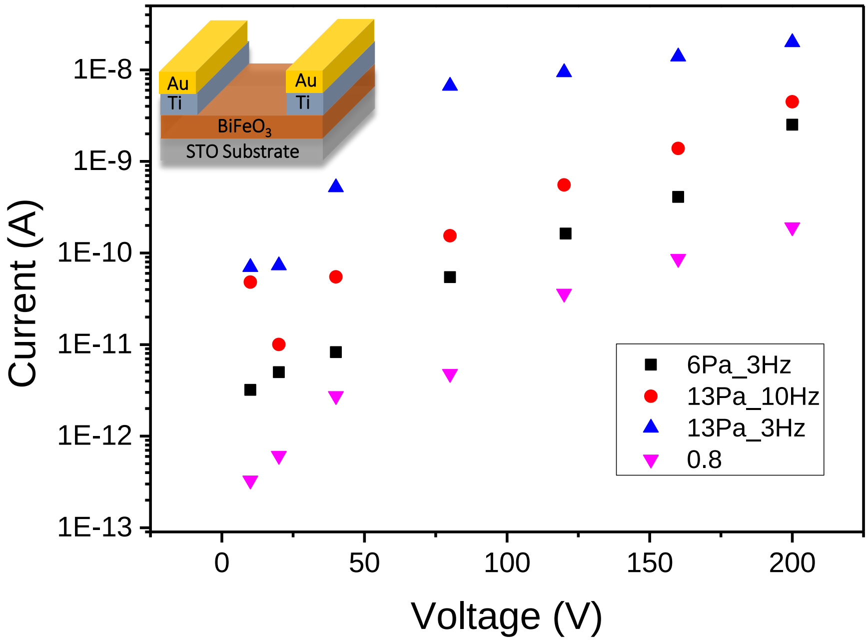

Fig. 3.5 Leakage current of BFO thin films.

Fig 3.5 shows the leakage currents of BFO thin films prepared under different parameters. Each data point presented in the figure is actually the average of 30 data points from a 30-second measurement under each voltage. The data of $Bi_{1.2}FeO_3$ film are not presented here because the film is too conductive and its leakage current is significantly larger than any of the other samples. As observed in the figure, sample $Bi_{0.8}FeO_3$ possesses the lowest leakage current followed by sample 6 Pa & 3 Hz, 13 Pa & 10 Hz and 13 Pa & 3 Hz, whose Bi/Fe ratio also increases in the same order. Therefore, the leakage current, or dark conductivity, of BFO thin film is dominated by the Bi/Fe ratio[82].

3.4.2 The photoelectric responses

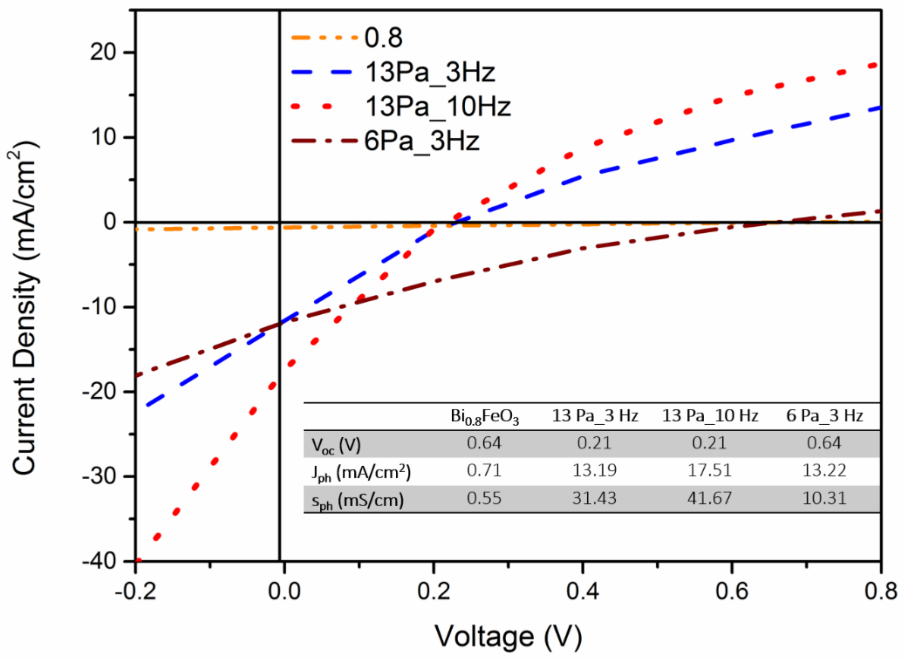

	$Bi_{0.8}FeO_3$	13 Pa_3 Hz	13 Pa_10 Hz	6 Pa_3 Hz
V_{oc} (V)	0.64	0.21	0.21	0.64
J_{ph} (mA/cm^2)	0.71	13.19	17.51	13.22
s_{ph} (mS/cm)	0.55	31.43	41.67	10.31

Fig. 3.6 I-V curves of BFO thin films under illumination. The inset list is a summary of photovoltaic behavior of BFO thin films

Fig. 3.6 shows photovoltaic behaviors of BFO thin films. Before measurement, all of these samples are poled by 200 V for 30 seconds, and then short-circuited for 30 seconds. It can be observed in Fig. 3.6 that the influence of secondary phases on FePV is more complex than on conductivity. Compared with a monotonic relationship between Bi/Fe ratio and the leakage current of the film, the photocurrent of BFO thin film is the minimum in the sample with the smallest Bi/Fe ratio

($Bi_{0.8}FeO_3$) and the maximum in the sample with nearly stoichiometric $BiFeO_3$ thin film (sample 13 Pa & 10 Hz), instead of the sample with the largest Bi/Fe ratio (sample 13 Pa & 3 Hz). Therefore, the photovoltaic effect in BFO thin film is essentially an intrinsic effect, and either a bismuth deficiency or a bismuth excess will lead to smaller photocurrent. S.M. Yong *et al.* has proposed a shift current theory where the electrons hop along polarization directions[10] A more detail discussion of the mechanism of FePV effect in BFO thin film will be presented in the next chapter in terms of electrode material.

The photoconductivity at zero bias can be calculated. According to equation (2) in section 1.2.2, the open-circuit voltage of thin film is proportional to photocurrent and reversely proportional to conductivity, i.e. $V_{oc} = \frac{J_{ph}}{\sigma_{ph}+\sigma_d} d$. Since the dark conductivity is negligible to photoconductivity, the results can be calculated directly, as listed in the inset of Fig. 3.6.

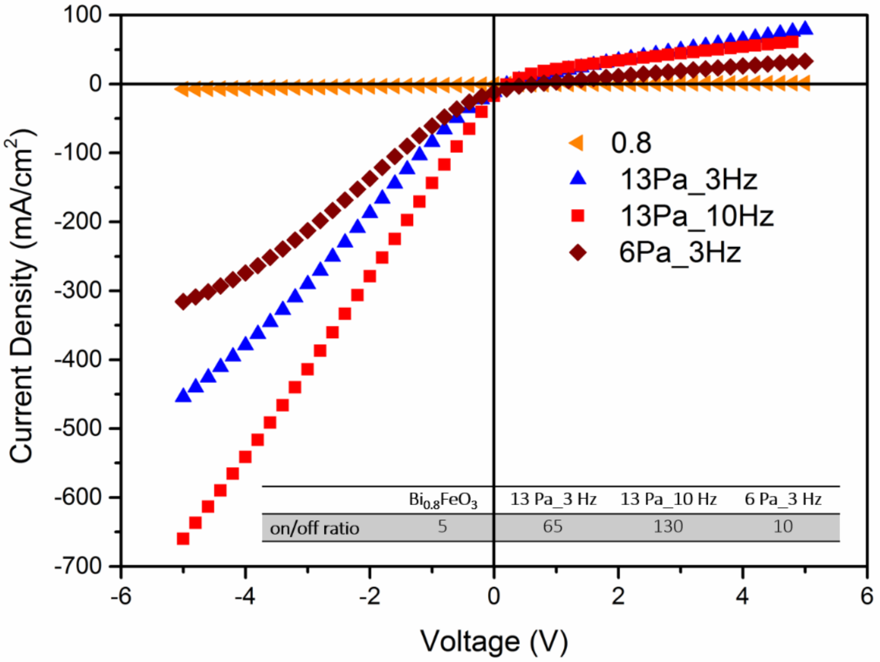

Fig. 3.7 I-V curves of BFO thin films under illumination in a large scale. The inset is calculated on/off ratio of BFO thin films

Fig. 3.7 shows photoelectric behaviors of all samples in a larger scale. As shown in the figure, the photocurrent under a negative bias is much larger than that under the positive bias, and the on/off ratios of the current density at 5 V of all the films are listed in the inset list of Fig. 3.7. These results suggest that the FePV in BFO thin film is an intrinsic bulk effect that requires a high thin film quality to produce a large photovoltaic response.

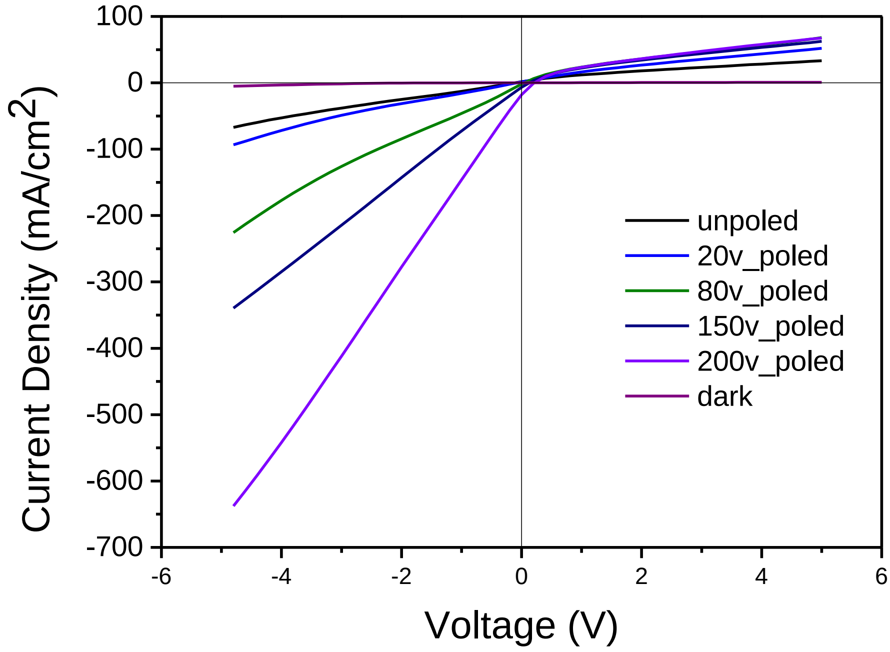

Fig. 3.8 I-V curves of the BFO thin film 10 Hz & 13 Pa.

Fig. 3.8 shows I-V curves of film 10 Hz & 13 Pa poled by different voltages. The dark current was measured after poling by 200 V. As shown in Fig. 3.8, with increasing poling voltage, the photocurrent under positive external bias is deceased and saturated quickly, while the photocurrent under negative bias is increased. Fig. 3.9 shows the on/off response of film 10 Hz & 13 Pa under zero-bias, and the result was measured after short-circuit the film for 24 hours. As shown in Fig. 3.9, a very stable on/off response is observed for 10 cycles.

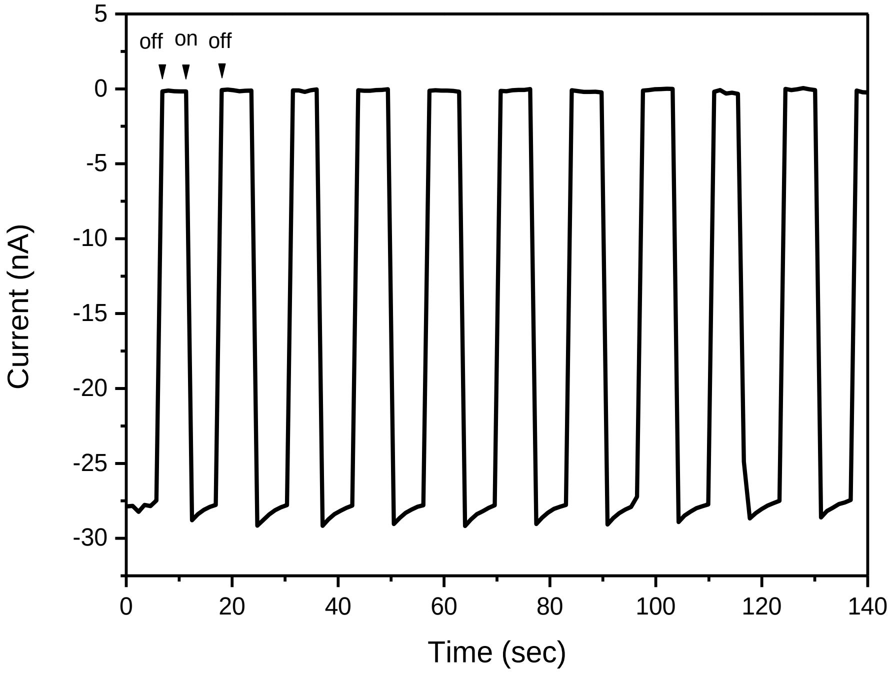

Fig. 3.9 Light on/off response of film 10 Hz & 13 Pa.

Fig. 3.10 shows the switching behavior of film 10 Hz & 13 Pa. The solid lines represent poling by one direction and dashed lines represent poling by the opposite direction. The results show symmetric shift of the I-V patterns upon poling in reverse directions with increasing voltages.

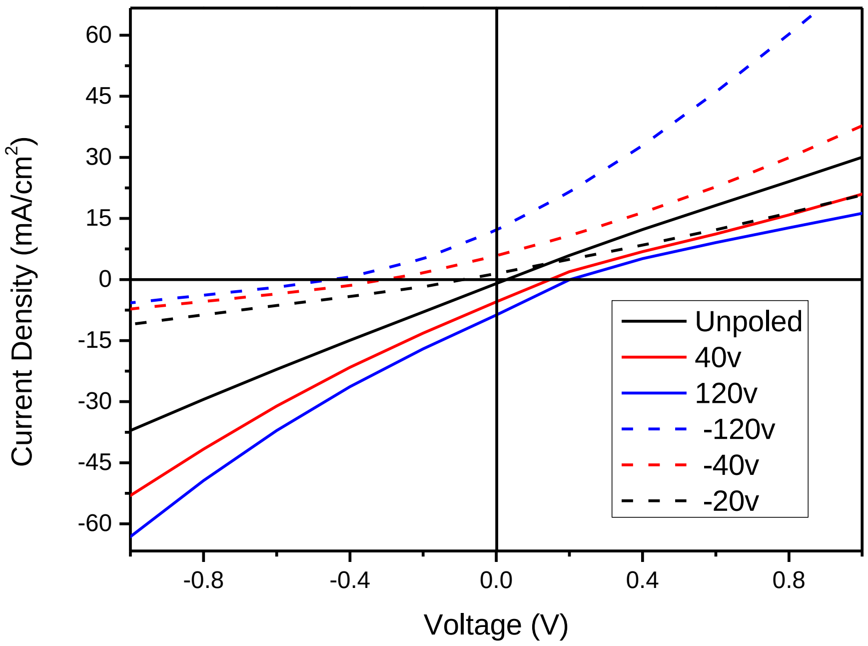

Fig. 3.10 Switchable photovoltaic behavior of film 10 Hz & 13 Pa.

3.5 Ferroelectric properties of BFO thin films prepared under optimized parameters

To examine the ferroelectric properties of optimized film, 200 nm-thick BFO thin film was deposited on LSMO buffered STO substrate. The deposition parameters for LSMO electrode are: substrate temperature at 700 °C, oxygen pressure at 13 Pa, ablation rate of 5 Hz, and laser energy of 1.2 mJ/cm^2.

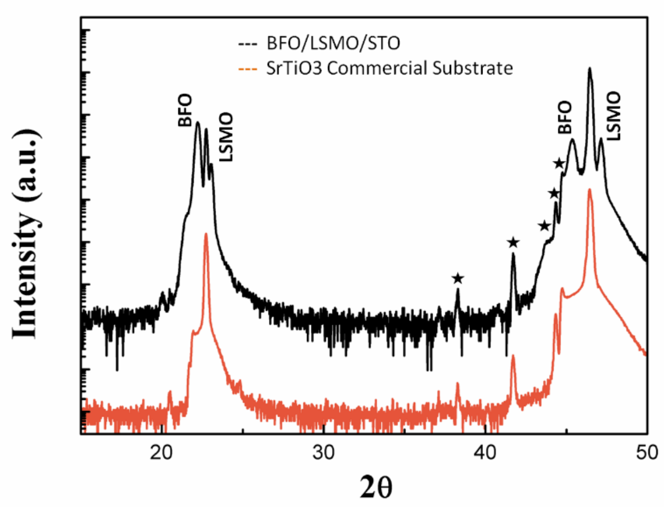

Fig. 3.11 XRD patterns of the BFO/LSMO/STO sample and the commercial STO substrate.

Fig 3.11 shows the XRD pattern of BFO/LSMO/STO thin film, in which the impurity peaks brought by the substrate are marked as stars. It can be seen that a pure BFO phase is also obtained in our sample with LSMO bottom electrode. The undesired peaks brought by the STO substrate imply that the substrate was not perfectly cut.

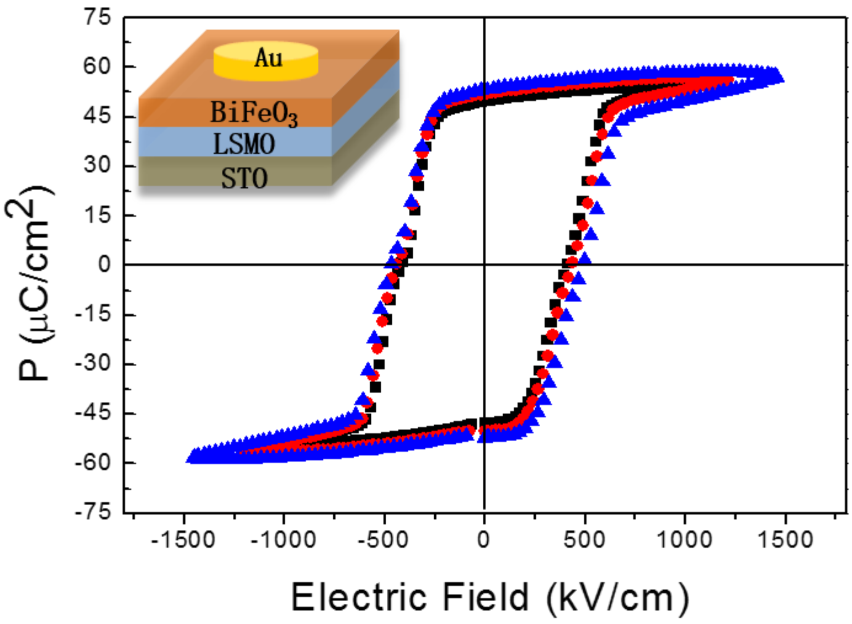

Fig. 3.12 P-E loop of BFO thin film. The applied electric fields are 500, 750 and 1000 kV/cm. The inset schemes the device structure.

As shown in Fig. 3.12, a square P-E loop is obtained from the schemed device with a remnant polarization of 58 μC/cm^2 at a driven frequency of 1 kHz. Fig. 3.13 shows a typical PFM image of the BFO thin film. The film is first positively poled at 8 V, and then negatively poled at -10 V in the dark area.

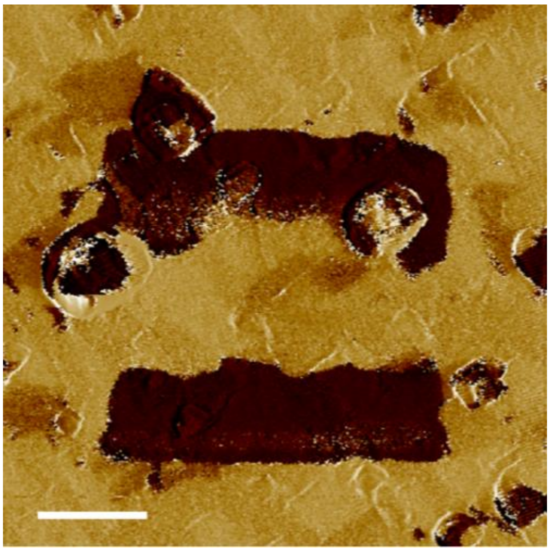

Fig. 3.13 PFM image of BFO thin film. The dark area is poled negatively while the light area is poled positively. The white scale bar represents 1 μm.

3.6 Summary

In this section, structure characterization of BFO thin film deposited under different parameters are presented. An optimal parameter set is selected, that is, oxygen pressure of 13 Pa and ablation rate of 10 Hz. Deviation from optimal condition leads to either poorer epitaxy of the film or secondary phases. The leakage current and photoelectric response of the films are examined. The bismuth vacancies and Bi_2O_3 secondary phases, are confirmed to affect the dark conductivity, photoconductivity and photocurrent of the film. The results suggest a convenient way to control the photovoltaic behavior of BFO thin film through the fine-tuning of deposition parameters. In the end, the ferroelectric behavior and FePV properties of the film prepared under optimal parameter set are presented. This work provides some detailed understanding on the FePV effect in BFO thin film and possible solution to BFO thin films with good photovoltaic properties.

Chapter 4. Influence of electrode material on FePV of BFO Thin Film

4.1 Introduction

In chapter 3, the influence of deposition conditions on FePV effect in BFO thin film was discussed, and a large photocurrent was obtained under optimized oxygen pressure, laser ablation rate and target composition.

In this chapter, the influence of electrode material on FePV of BFO thin film deposited under optimized condition is investigated. Gold electrode (Au/BFO) and titanium electrode (Ti/BFO) were used for comparison, and the electrode configurations were the same with the one in Chapter 3 Fig. 3.5. Bin Chen *et al.* have examined the effect of top electrode materials on the photovoltaic properties of polycrystalline BFO thin film based devices[61], and it was found that the photovoltaic efficiency in ITO/BFO/Pt is 25 times larger than that in Au/BFO/Pt sample. However, detailed mechanism of the electrode effect is still unknown. In this work, the effect of electrode materials on the photovoltaic properties of epitaxial BFO thin films is studied thoroughly, and the in-plane electrode configuration was chosen in particular because the symmetric configuration of electrodes can exclude unwanted factors that will affect a clear explanation on the effect of electrode materials on FePV.

BFO samples used in this work were prepared under the optimal deposition conditions as described in Chapter 3, i.e. sample 10 Hz & 13 Pa. Titanium and gold electrodes were deposited by magnetron sputtering, and classical lift-off lithography was used for electrode patterning. The shape of each electrode is rectangular with 50 μm in width and 200 μm in length, and two electrodes are placed in parallel with a distance of 5 μm. Dimension Icon Atomic Force Microscope (Bruker) was used for surface potential (SPoM) measurement.

4.2 Experimental result.

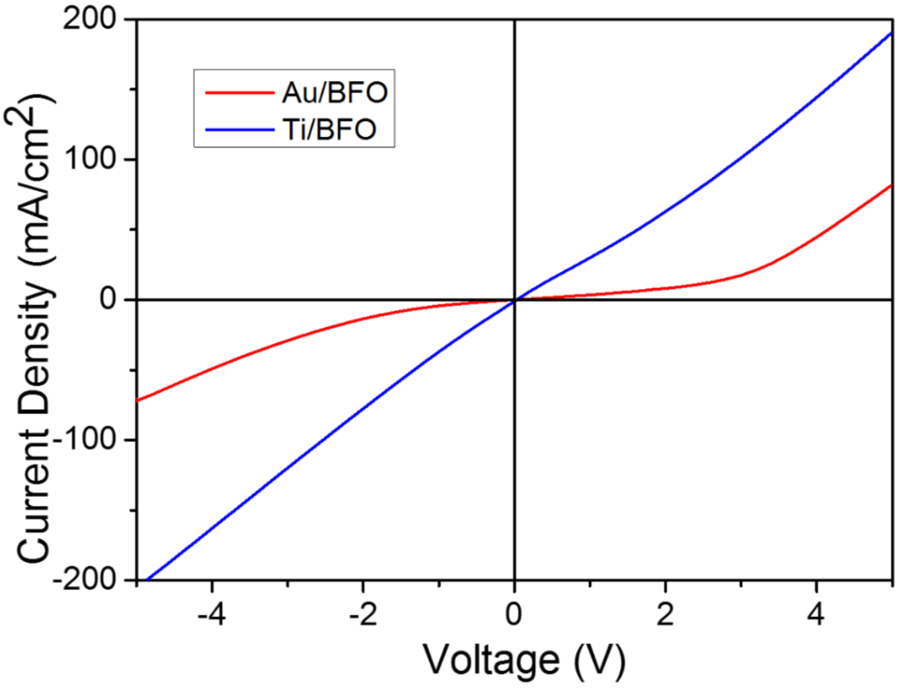

Fig. 4.1 I-V curves of Au/BFO and Ti/BFO samples under illumination before poling.

Fig. 4.1 shows photo-response of BFO thin films in virgin state (before poling). It can be seen that the I-V curve of Ti/BFO sample under illumination is almost linear around zero bias, while that of Au/BFO sample is nonlinear, which implies that the electrode material has a significant influence on the photovoltaic properties. According to S. J. Clark *et al*, the Fermi level of BFO is about 4.7 eV, and the work functions of titanium and gold are 4.3 and 5.1 eV, respectively[35]. The band alignment BFO thin film at the electrode/BFO interface is shown in Fig.4.2. Ohmic contact is formed at the Ti/BFO interface, and there is no potential barrier that obstacles electron transport from BFO thin film to titanium electrode. On the contrary, Schottky contact is formed at Au/BFO interface with a potential barrier of about 0.4 eV, and excited electrons could only pass the barrier by thermal activation at around zero bias. When the bias voltage is much larger than 0.4 V, the slope of I-V curve, i.e. conductivity, is about the same in two samples, which means that the intrinsic conductivity of BFO thin film is not influenced by different types of interface contact.

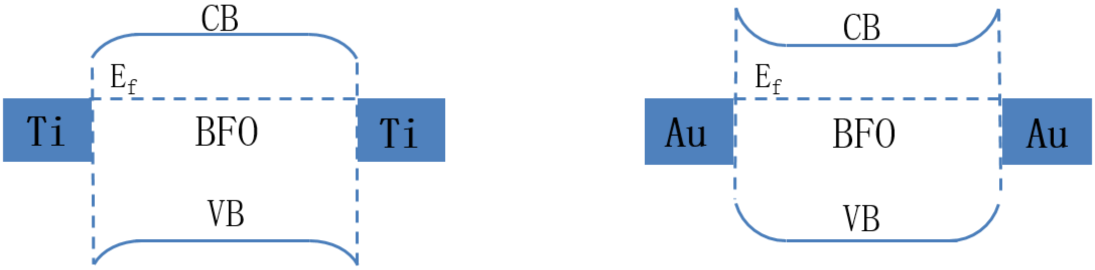

Fig. 4.2 Schematic graphs of band alignment at the interface of BFO thin film with titanium and gold electrodes, respectively.

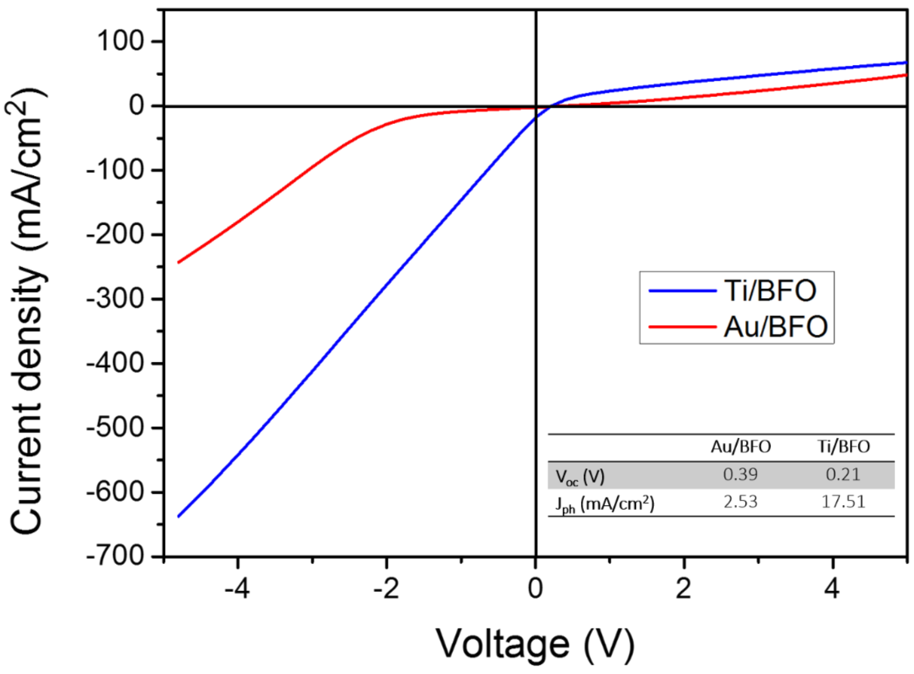

	Au/BFO	Ti/BFO
V_{oc} (V)	0.39	0.21
J_{ph} (mA/cm^2)	2.53	17.51

Fig. 4.3 I-V curves of Au/BFO and Ti/BFO samples under illumination after poling. The inset is summary of photovoltaic properties of two samples.

Fig. 4.3 shows the I-V curves of two samples under illumination after poling. The photovoltaic behavior of two samples are very much different. The J_{ph} and V_{oc} of sample Au/BFO and Ti/BFO are listed in the inset list of Fig. 4.3, and it is clearly shown that the photocurrent density of sample Ti/BFO is far more excellent than that of sample Au/BFO, therefore it is very tempted to use titanium as electrode material instead of gold in photovoltaic application of BFO. It can be also seen that the conductivity of BFO thin film is distinctly different under positive or negative bias for both samples, and the turning point of sample Au/BFO is on the negative bias side while that of sample Ti/BFO is on the positive bias side.. Here, the positive bias refers to the same positive electrode used in poling process, and the negative bias refers to the opposite bias field applied. These distinctively differences of photovoltaic behavior in two samples are proposed to be highly related to the metal-semiconductor contact formed at electrode interface. The reasons are presented in the following context with the help of band alignment diagram.

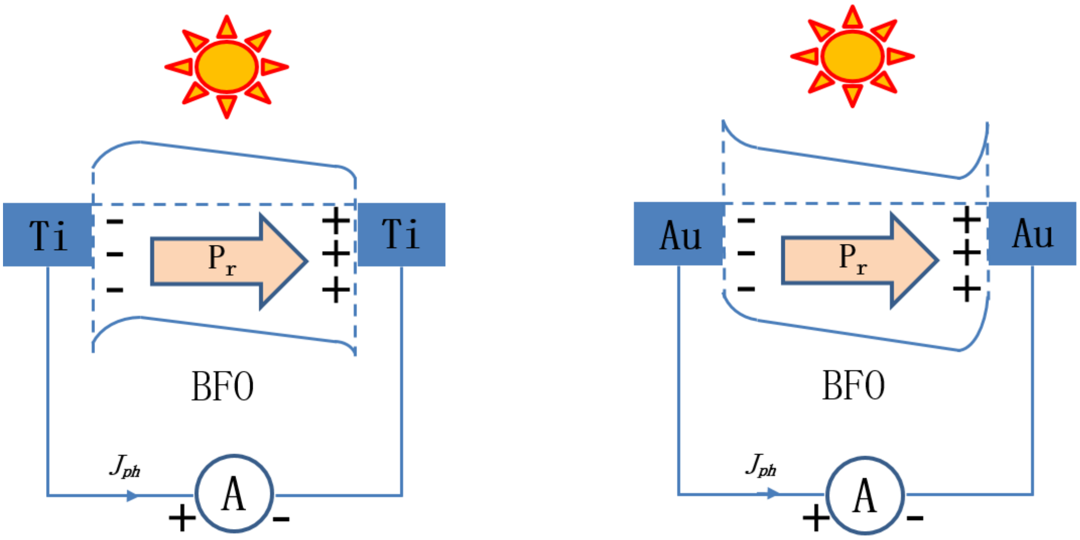

Fig. 4.4 Schematic graphs of interface band alignment of Ti/BFO and Au/BFO samples at zero bias after poling. J_{ph} represents for photocurrent at zero bias

Fig. 4.4 shows the change of band alignment of two samples at zero bias after been poled. After poling, the positive and negative charge centers in the BFO thin film are aligned along electric field. Therefore, the very thin layers beneath the electrodes are regarded as being equivalently doped by anions and cations, and the photocurrent flows in the opposite direction of polarization as discussed in previous chapter. However, the magnitude of photocurrent is much different in two situations. For Ti/BFO sample, as shown in the left graph of Fig. 4.4, there is no potential barrier and the electrons transport fluently from BFO to electrode, which results in the tuning point a large photocurrent density of 17.51 mA/cm^2. For Au/BFO sample, the potential barrier reduces the photocurrent greatly, which results in a small photocurrent density of 2.53 mA/cm^2.

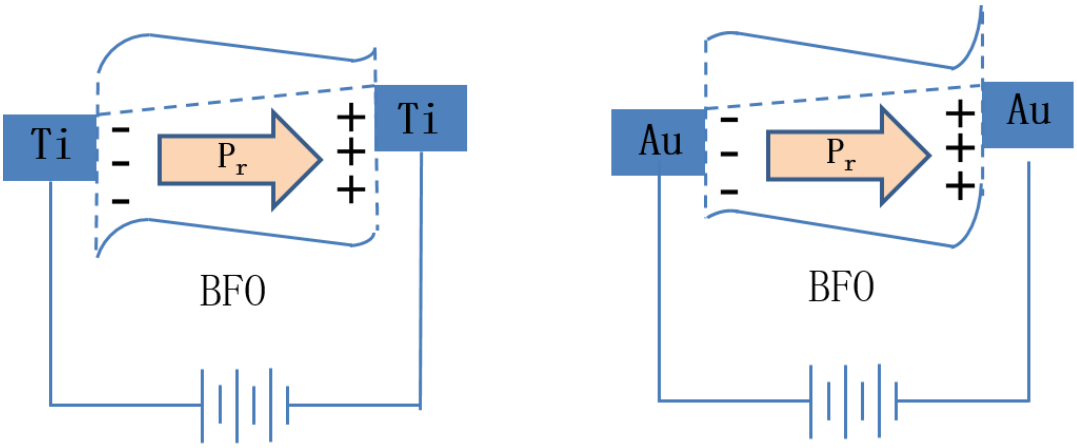

Fig. 4.5 Schematic graphs of the interface band alignment of Ti/BFO and Au/BFO samples at a large positive bias after poling. The slope of Fermi level is enlarged for better presentation.

Fig 4.5 shows the band alignment at a large positive bias. At a small positive bias, the contact type of both electrodes in Ti/BFO is Ohmic. However, as observed in the left figure, the contact at the negative electrode in Ti/BFO sample could transfer from Ohmic to Schottky when the positive bias is large enough. Therefore, the conductivity of BFO thin film becomes smaller due to the potential barrier. For Au/BFO thin film, even though the contact at the positive electrode would transfer to Ohmic contact under a large positive bias, the contact at the negative electrode is always Schottky contact with an even higher potential barrier.

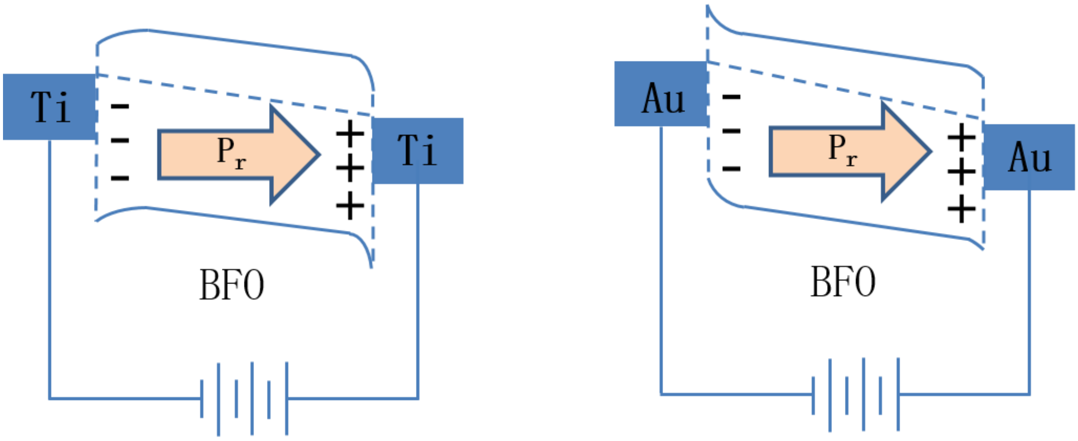

Fig. 4.6 Schematic graphs of interface band alignment of Ti/BFO and Au/BFO samples at a large negative bias after poling. The slope of Fermi level is enlarged for better presentation.

The situation for negative bias is sketched in Fig. 4.6. Under a small negative bias, both electrodes in Au/BFO samples are Schottky contacts and the positive electrode transfers to Ohmic contact at a larger negative bias, as shown in the right figure of Fig. 4.6. Thus, the transportation of electrons becomes much easier and the conductivity of BFO changes greatly. For film Ti/BFO, the conductivity under negative bias remains unchanged since the contact type of the positive electrode is still Ohmic.

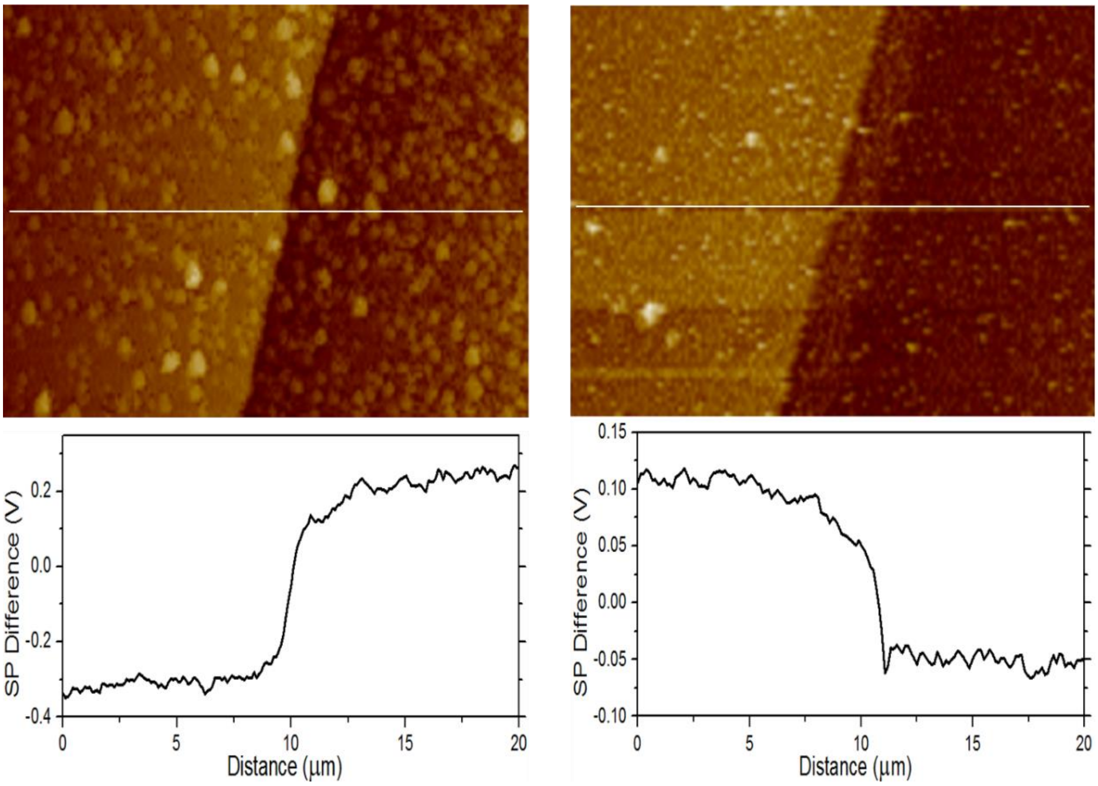

Fig. 4.7 AFM (upper) and SPoM (lower) results at the interface of Ti/BFO (right) and Au/BFO (left) samples. The white line indicates the scanning trace of SPoM measurement.

To confirm the type of electrode contact in two samples, the SPoM is under taken to measure the difference of surface potential of Ti Vs BFO and Au Vs BFO, as shown in Fig. 4.7. The darker part in AFM images indicates BFO thin film and the lighter yellow part is electrode. The SPoM data were measured by scanning along a straight line marked in the AFM images. The surface potential difference of Au/BFO is 0.55 V, which indicates that the contact is Schottky type; and the surface potential difference of Ti/BFO is -0.17 V, which indicates that the contact is Ohmic type. Therefore, it is safe to conclude that the proposed mechanism is based on solid ground. In addition, the Fermi level of our BFO thin film can be calculated to be around 4.5~4.6 eV.

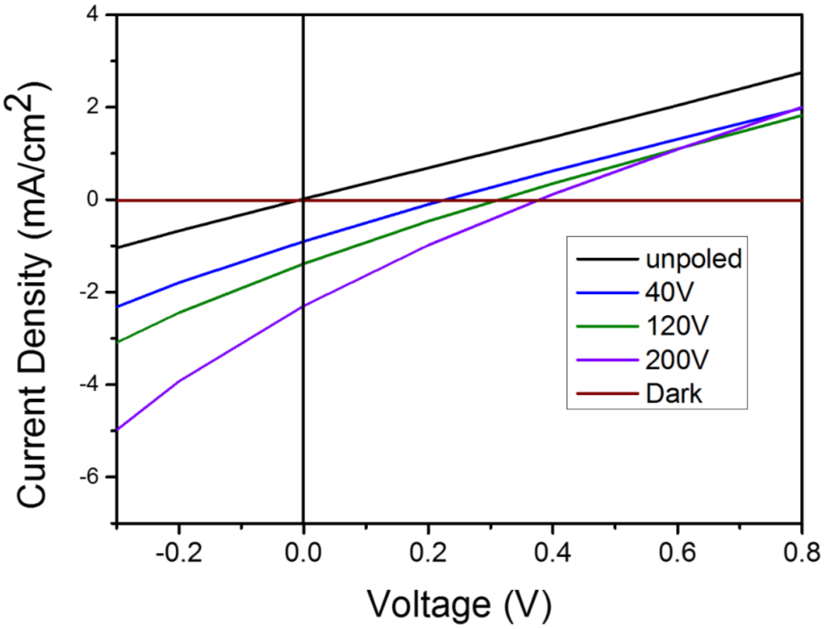

Fig. 4.8 I-V curves of photo-response of Au/BFO sample around zero bias.

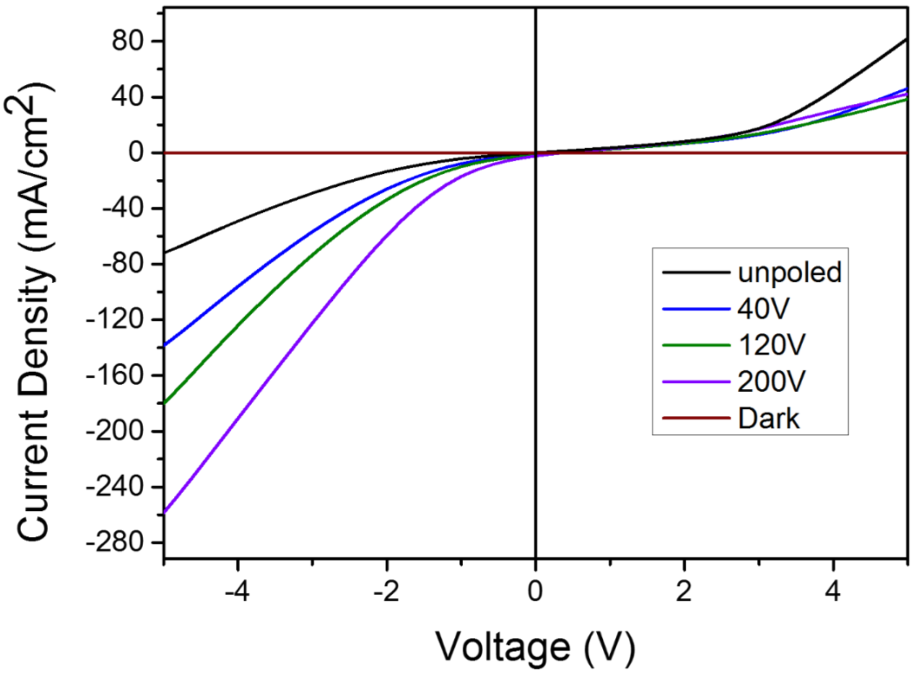

Fig. 4.9 I-V curves of photo-response of sample Au/BFO at a larger scale.

Fig. 4.8-4.9 shows the I-V curves of Au/BFO sample poled by different external voltages, and the on/off ratio of photocuurent at ±5V is calculated as 6.5, which is far less than 130 of Ti/BFO sample presented in Fig 3.7. This result further implies that using Au as electrode in photovoltaic application affects the efficiency of electron transportation and is suggested to be replaced by materials with small work function like titanium.

4.3 Summary

In this chapter, the effect of electrode materials on photovoltaic properties of BFO thin film is investigated in detail. The photocurrent measured in Ti/BFO sample is 7 times larger than that in Au/BFO sample, while the open circuit voltage in Ti/BFO sample is about half of that in Au/BFO sample. It is clearly shown that interface contact plays a critical role in electron transportation from BFO thin film to electrode. Our results recommend that Ohmic electrode contact is preferred in BFO photovoltaic application to obtain a better performance.

Chapter 5. Strain effect on FePV properties of BFO

5.1 Introduction

Strained $BiFeO_3$ (BFO) has proven to show intriguing properties, many of which are very different from the parent unconstrained BFO phase. Different substrates would lead to different lattice structure in the upper thin film, as shown in Fig. 5.1, and hence different physical properties. Epitaxial growth of $BiFeO_3$ (with a lattice constant of a_{pc} = 3.96 Å) on $LaAlO_3$ (a_{pc} = 3.78 Å) is under a large compressive stress due to a lattice mismatch of 4.4%[42]. The lattice structure of the resulting BFO thin film is varied greatly at different film thickness. In very thin films on LAO, a pure tetragonal phase would be observed, while thicker films tend to be almost pure R-like phase. The strain relaxation progression in BFO/LAO thin film usually happens in sequence of pure tetragonal phase, M_C phase, mixed M_C-M_A and M_A phase[87][88]. With the increasing of film thickness, the surface morphology of BFO/LAO is accordingly modified[88].

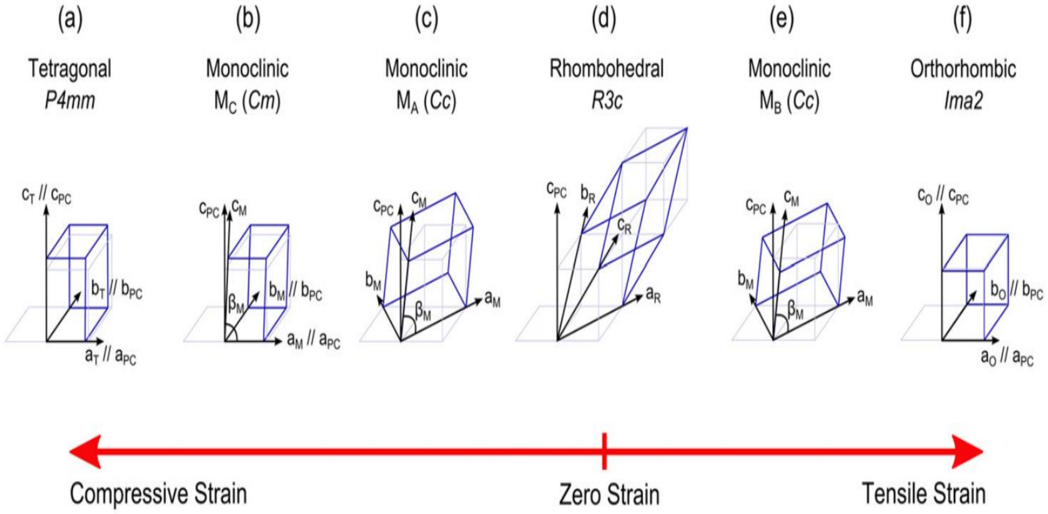

Fig. 5.1 Summary of various lattice structures in BFO thin films deposited on different substrates. (a) pure tetragonal (T) phase; (b) T-like monoclinic (M_C) phase; (c) R-like monoclinic (M_A) phase; (d) bulk-like rhombohedral (R) phase; (e) M_B monoclinic phase; and (f) the orthorhombic (O) phase.

Piezoelectric single crystal (1-x)$Pb(Mg_{1/3}Nb_{2/3})O_3$-x$PbTiO_3$ (PMN-PT) (with a lattice constant of a = b = 3.9969 Å, c = 4.0457 Å) has been proven to provide a nearly uniform linear biaxial strain to the ferroelectric thin film deposited on it and it has been employed to reversibly control electric and magnetic properties. A maximum compression in the in-plane lattice constant of 0.24% can be induced in BFO/PMN-PT thin film by an external field applied on substrate. Though it is not large enough to induce a phase transition in BFO from rhombohedral phase to M_A phase, the strain effect on the physical properties can be quantitatively measured.

The influence of strain effect on physical properties is also pronounced. In BFO (1 1 1)-oriented films, a polarization of about 100 μC/cm^2 have been reported, which is also observed in bulk BFO material[33]. However, in the T-like phase of BFO thin film deposited on LAO substrate, a huge polarization of about 150 μC/cm^2 has been numerically calculated and experimentally realized[49]. Moreover, the ferroelectric Curie temperature T_C of BFO thin film was shown to be greatly reduced with increasing compressive strain provided by different substrates[89].

In recent years, FePV effect of BFO thin film has attracted intensive attention for its rich fundamental physics and great application potential. However, the influence of strain effect on the photovoltaic properties of BFO thin film is still unclear. In this chapter, the FePV effect in BFO thin film with large compressive (deposited on $LaAlO_3$ substrate) and tunable strain (deposited on $(1-x)Pb(Mg_{1/3}Nb_{2/3})O_3-xPbTiO_3$, x = 0.33) are examined. In addition, FePV effect in strain-free BFO nanofibers are also presented as complementary results.

5.2 Influence of tunable strain

5.2.1 Structure characterization

In order to investigate the influence of tensile strain on the photovoltaic effect, 200 nm of BFO thin film was deposited on PMN-PT (1 1 1) substrate under the optimal deposition parameter set presented in Chapter 1. 50 nm of titanium and 100 nm of gold are deposited by magnetron sputtering in sequence as top electrodes, and 100 nm of gold is used as a bottom electrode. Schematic diagram is shown in Fig. 5.2.

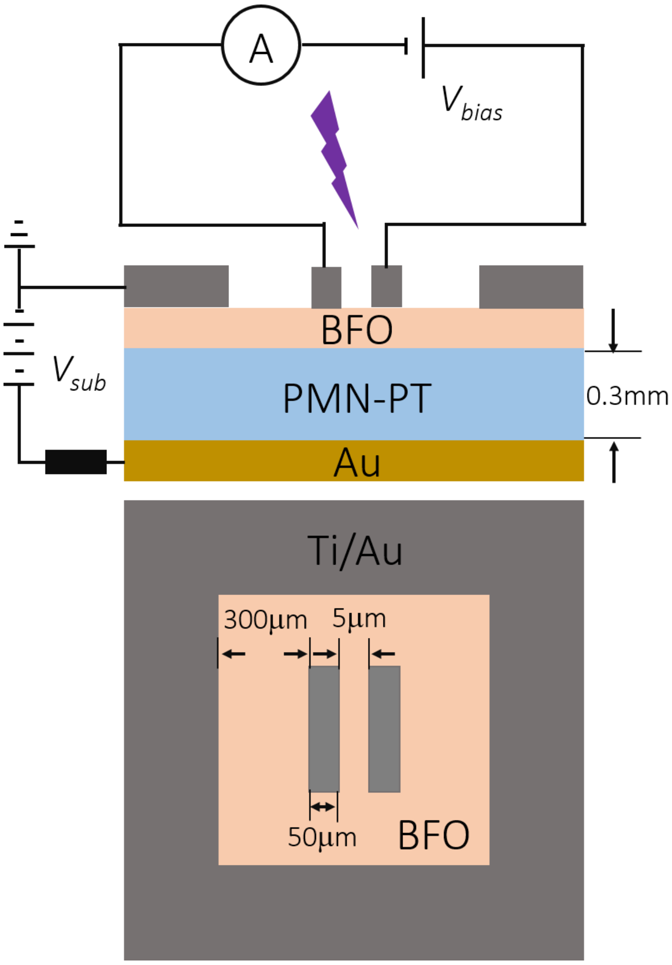

Fig. 5.2 Schematic diagram of electrode configuration and photovoltaic measurement setup. Keithley 6517b electrometer was used to provide bias voltage (V_{bias}) and photocurrent measurement. Keithley 2400 was used for V_{sub}. Some parts of the diagram are intentionally enlarged for clarity.

The crystalline quality of BFO thin film was examined by high resolution X-ray diffractometer. In the XRD measurement, a voltage (V_{sub}) was applied to the PMN-PT substrates to induce a change of lattice constant, as shown in Fig. 5. The change of lattice constant of BFO/PMN-PT thin film under 0 and 200 V is presented in Fig. 5.3. The XRD data suggested a bulk-like rhombohedral phase in BFO thin film, which is also confirmed in previous work[90]. It can be seen that the diffraction peak of PMN-PT (1 1 1) is shifted to the left under 200 V, which means that the crystal lattice in the out-plane direction is elongated. Following the shift of the PMN-PT peak as marked by the red star, BFO (1 1 1) diffraction peak is also shifted closer to the PMN-PT peak. The change of out-plane lattice constant under 200 V of V_{sub} is calculated to be 0.24%, as compared with that under 0 V.

The Raman spectroscopy of BFO/PMN-PT thin film is showed in Fig. 5.4. Typical peaks for A_1 modes in BFO rhombohedral phase are indicated by dashed lines, and the characteristic peaks for PNM-PT single crystal are also marked. The Raman result confirms the rhombohedral phase in BFO thin film as suggested by the XRD data.

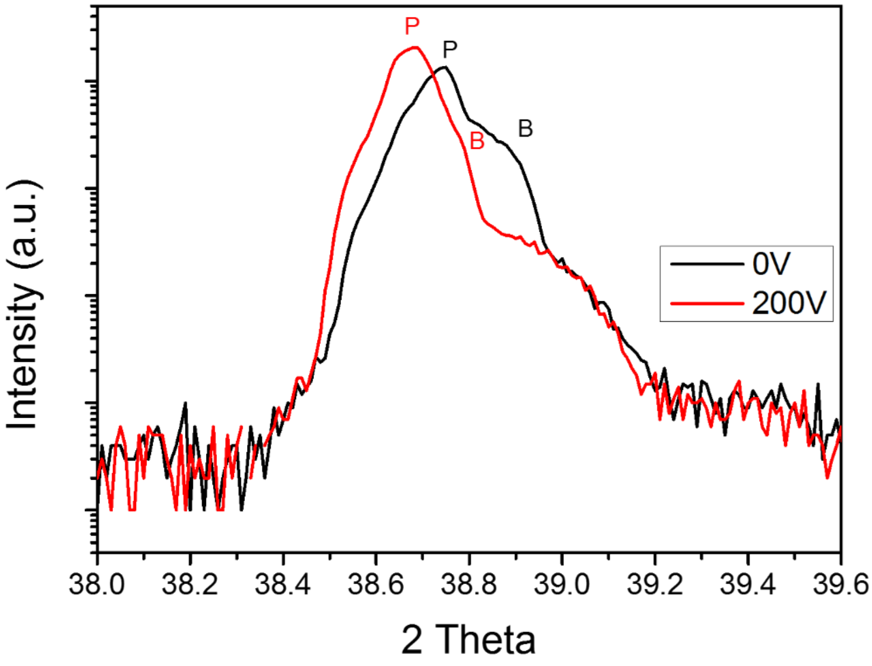

Fig. 5.3 2θ-ω scan of BFO/PMN-PT sample.

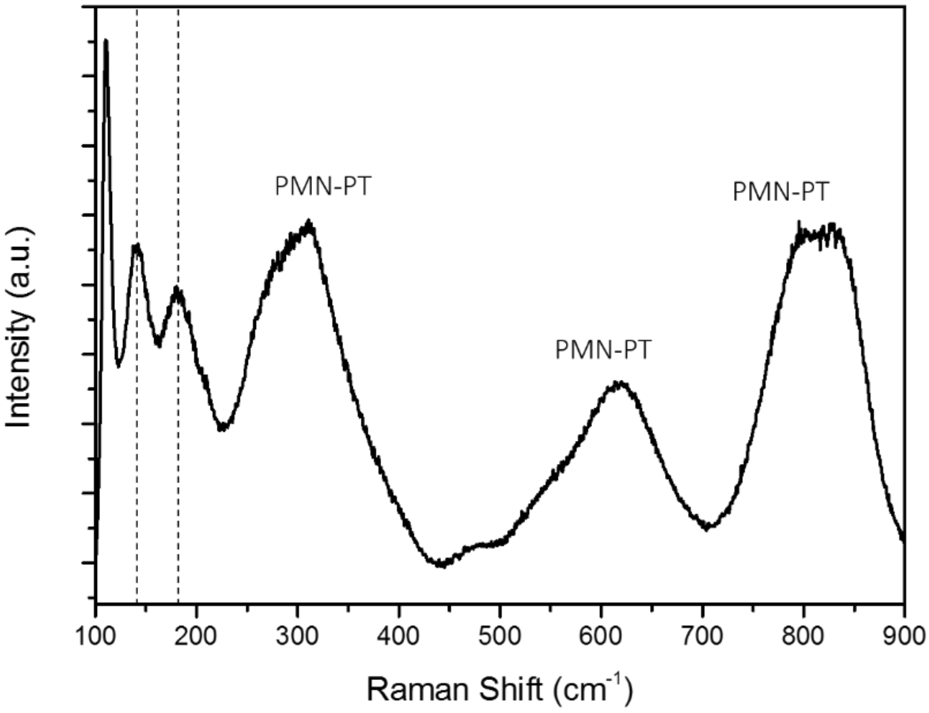

Fig. 5.4 Raman spectroscopy of BFO/PMN-PT sample. BFO rhombohedral phase is indicated by dashed lines

5.2.2 Photovoltaic measurement

In Fig. 5.5-5.6, the I-V of BFO/PMN-PT sample under illumination is presented. Since the lattice constant would change in BFO thin film when PMN-PT substrate is subjected to an external V_{sub}, as observed in XRD profile, it is natural to expect that the photoelectric behavior of BFO thin film can be also tuned by V_{sub}. As observed in Fig. 5.5, the photocurrent shifts in parallel under different V_{sub}. However, the photoconductivity does not change. Therefore, a small change (0.24%) of strain by the substrate is not enough to change the photoelectric behavior in BFO thin film.

Fig. 5.6 shows the I-V curve of BFO/PMN-PT sample poled by different $V_{bias.}$ The poling process persists for 30 seconds, and then short-circuit for another 30 seconds. A weak photo-response is recorded in the sample, and a photocurrent density of $2x10^{-4}$ A/cm^2 and open circuit voltage about 1V are obtained. The small photocurrent density is resulted from two reasons: first, the PMN-PT provides a moderate tensile strain of about 0.48% to BFO thin film, therefore the bulk photovoltaic effect is reduced by change of lattice structure. Second, according to equation (1) in Chapter1, the photocurrent J_{ph} is related to the glass coefficient $\boldsymbol{\beta}_{ijk}$, which is different in BFO (1 1 1) and BFO (0 0 1), resulting a smaller photocurrent in BFO (1 1 1) situation[9].

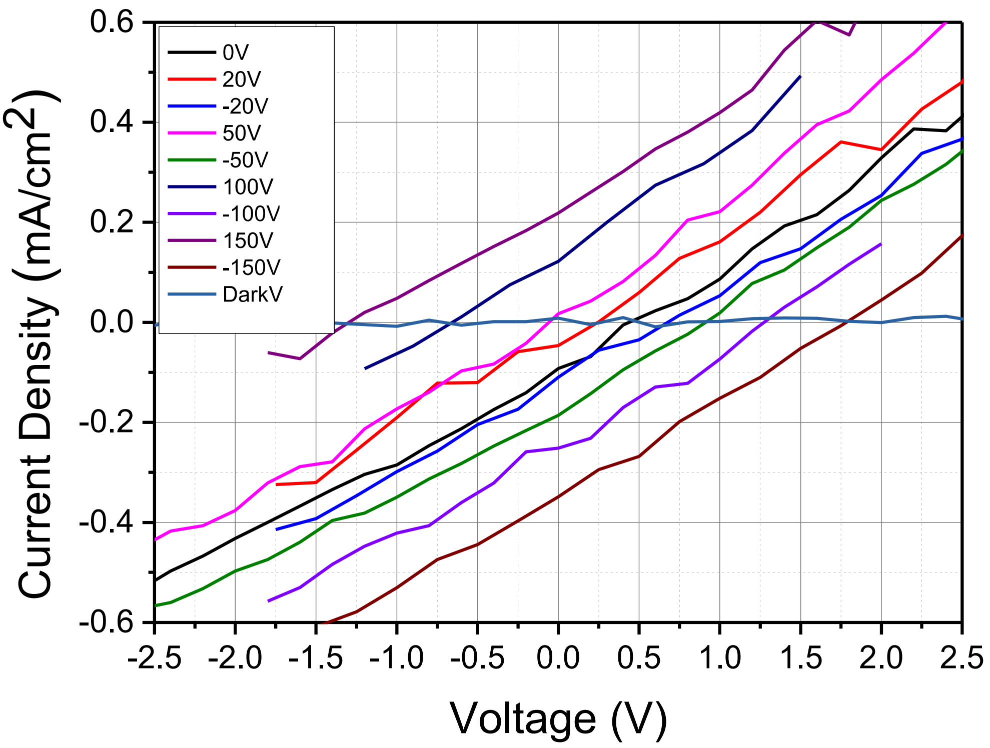

Fig. 5.5 I-V curves of BFO/PMN-PT sample under different V_{sub}.

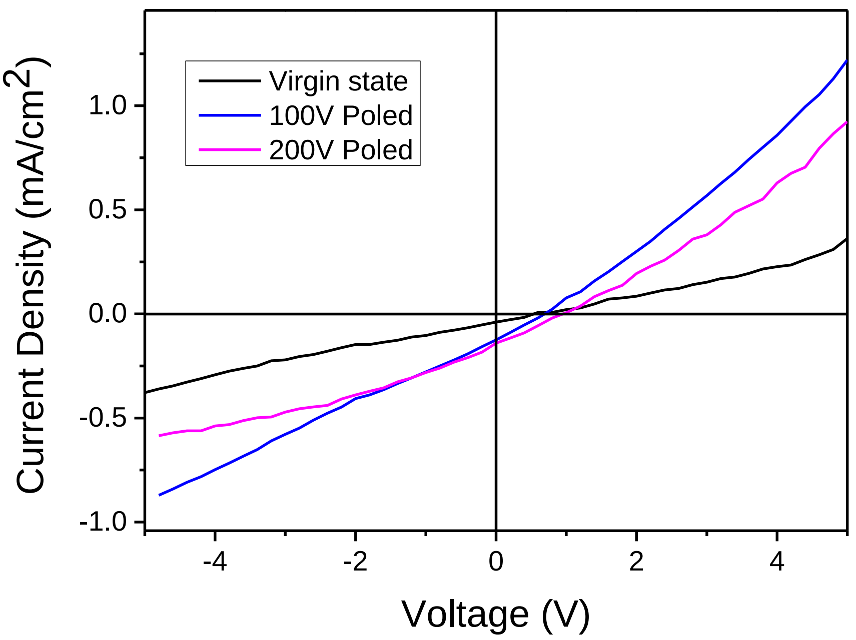

Fig. 5.6 I-V curves of BFO/PMN-PT sample poled by different voltages.

5.3 Influence of compressive strain

5.3.1 Structure characterization

In order to investigate the influence of large compressive strain on the photovoltaic effect, 200 nm of epitaxial BFO thin film was deposited on LAO (0 0 1) substrate under the optimal deposition parameter set presented in Chapter 1. The crystalline quality of BFO thin film was examined by high resolution X-ray diffractometer. In Fig. 5.7, 2θ-ω profile of BFO/LAO sample shows the strong (0 0 1) and (0 0 2) diffraction peaks indicating that BFO are of single phase and highly (0 0 1)-oriented.

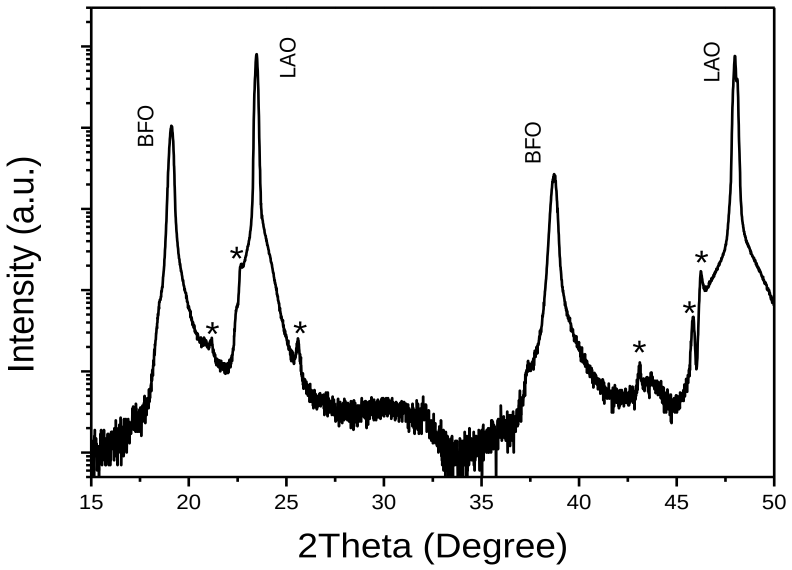

Fig. 5.7 2θ-ω profile of BFO/LAO sample. Black stars mark the undesired peaks brought by LAO substrate.

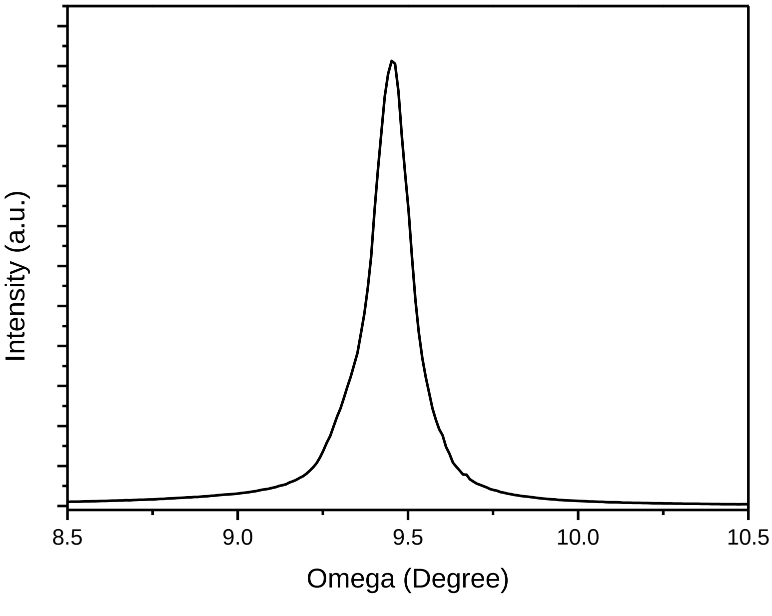

Fig. 5.8 Omega scan of BFO (0 0 1) peak.

As observed in Fig. 5.8 of, the FWHM of BFO (0 0 1) diffraction peak is 0.13482, and the out-of-plane lattice parameter is 0.469 nm. The Omega scan shows a highly epitaxial BFO thin film under a larger in-plane compression, with a strain along (0 0 1) direction of 19%. The morphology image was acquired by AFM, as showed in Fig 5.9. The roughness of BFO thin film is about 3nm, and the AFM image shows a rather complex morphological pattern with lamella-like structures, which were caused by the formation of T-like phase, as observed in other papers[91][92]. The XRD and AFM results suggest mixed T- and R-like phases in the film.

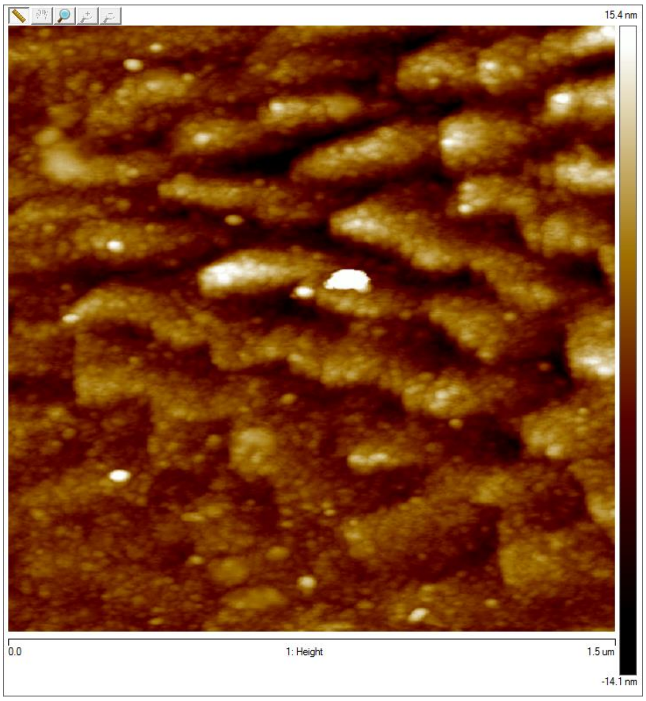

Fig. 5.9 AFM image of BFO/LAO sample.

Raman spectroscopy was conducted on BFO/LAO sample to confirm the lattice structure, as shown in Fig. 5.10. Typical Raman shift peaks of rhombohedral phase are indicated by dash lines at 175 and 222 cm^{-1}, and they are the same as the samples grown on STO substrates which are presented in Chapter 3 Fig. 3.4. There are also peaks (marked by stars) at 262, 526, and 640 cm^{-1}, representing the Raman active modes of the T-like phase[46][93]. This result confirms that the structure phase in our sample is mixed T- and R-like phases.

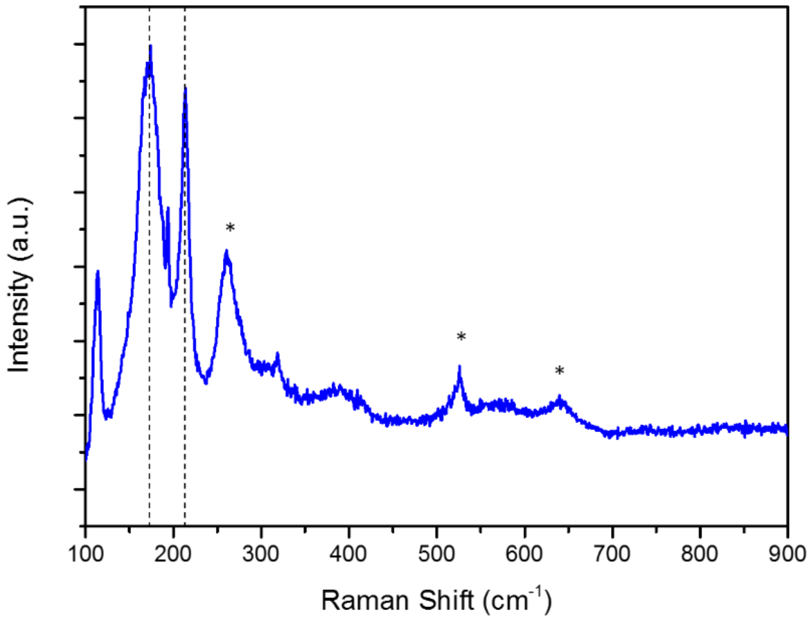

Fig. 5.10 Raman spectroscopy of BFO/LAO sample. Dashed lines indicate peaks of typical rhombohedral phase. Peaks marked by stars imply the existence of T-like phase.

5.3.2 Photovoltaic behavior

In order to investigate the photovoltaic effect in BFO thin film under large compressive strain, parallel electrode configuration was employed to measure the in-plane photocurrent. 50 nm and 100 nm of titanium and gold are deposited by magnetron sputtering in sequence as top electrodes, and the parallel electrodes are separated by 5 μm. As observed in Fig. 5.11, there isn't any obvious photocurrent at zero bias region. However, when the bias voltage was increased up to 120V, a distinct photocurrent was produced. The difference of conductivity in dark and illuminated thin film infers that there indeed exists photoelectric effect in highly strained BFO thin film, which is, however, not caused by bulk effect as in the R-phase BFO. The photocurrent in BFO/LAO is probably produced by sub-bandgap excitation in the surface defect sites, as suggested by Bhatnagar *et al.* [120]

Fig. 5.12 shows time profile of photocurrent at different V_{bias}. Compared with the time profile in BFO/STO sample as presented in Chapter 3 Fig. 3.9, the photocurrent in BFO/LAO is not very stable and it takes time to reach to a steady state when the V_{bias} is changed. Especially, when an opposite V_{bias} was applied to the thin film, a spike of current would appear, implying the slow mobility of excited electrons which were hampered by scattered distribution of surface defects.

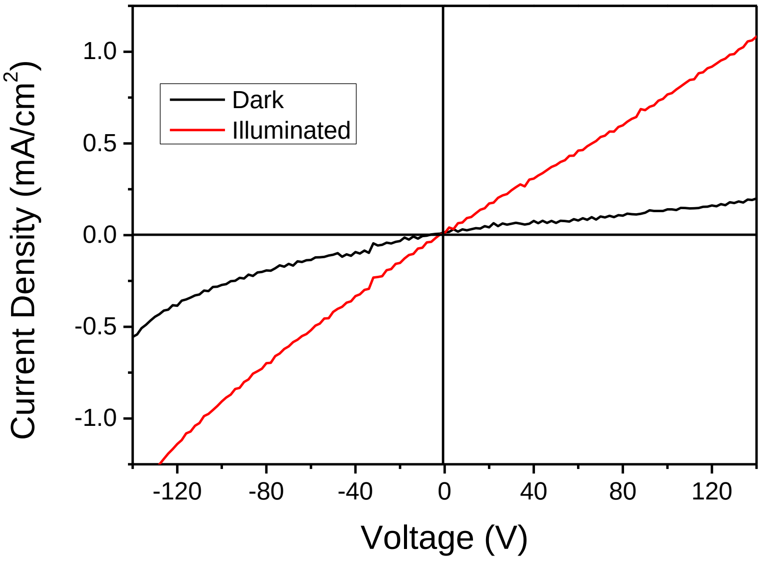

Fig. 5.11 I-V curve of BFO/LAO sample.

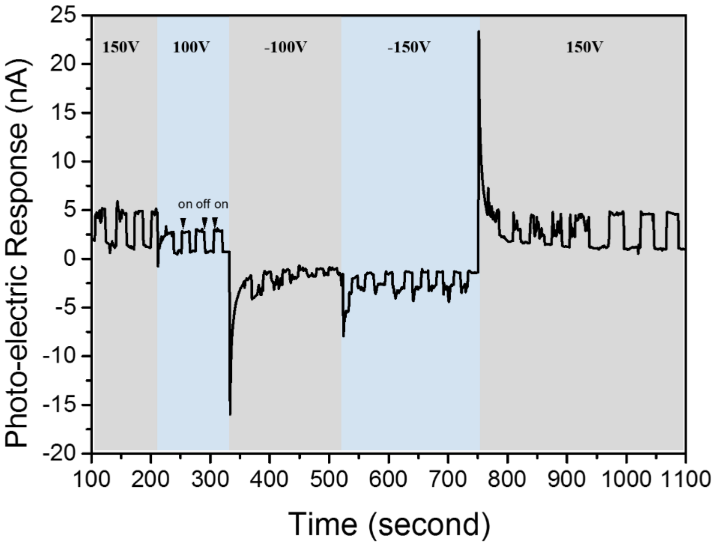

Fig. 5.12 Time profile of photocurrent in BFO/LAO sample under different V_{bias}.

5.4 Photovoltaic of strain-free BFO nanofibers

5.4.1 Introduction

Apart from thin film structure, nanofibers of bismuth ferrite are also of interest for materials scientists as such one-dimensional structure may be employed as building blocks to construct three dimensional functional materials and/or components. Due to the high-symmetry crystal structure of bismuth ferrite, it is not easy to synthesis nanofibers or nanowires of this oxide via conventional processes (such as hydrothermal method) despite that there are successful cases in the literature. Comparatively, electrospinning technique offers a more convenient alternative through which the morphology control becomes very easy.

In the literature, BFO-based photovoltaic devices have a common parallel-capacitor type of structure (also referred as a metal-insulator-metal “sandwich” structure). The advantage for such structure is that the devices can be made using standard semiconductor technology with a buffer layer (despite there is actually a technical compatibility issue due to the volatility of bismuth at high temperature). The problems associated with such configuration are that the devices may exhibit (1) low output voltages because the output voltage of a single “sandwich” is proportional to film thickness (typically < 1 μm) and (2) suppressed ferroelectric polarization due to the clamping effect from the substrate and hence relatively poor photovoltaic coefficient. In light of this situation, we propose to develop BFO-nanofiber based photovoltaic devices with a new configuration of nanofibers/IDE/substrate (where IDE refers to “interdigital electrode”). In our structure, much higher output voltage could be obtained because it is now proportional to the length of BFO nanofibers (which could be > several micrometers long). Meanwhile, the nanofibers are free-standing and free of substrate clamping effect. It is noted that such laterally aligned structures have been adopted in energy harvesting systems such as piezoelectric nanogenerators but not yet used in photovoltaic devices. To make devices with the above-mentioned configuration, the development of high quality BFO nanofibers is a critical step. In this work, the electrospinning method was employed as it is a feasible and scalable technique for making nanofibers by utilizing an electrical voltage to draw fibers from a liquid with suitable viscosity[94]. Due to thermodynamic reasons, the synthesis of bulk BFO via solid-state reaction is often associated with the formation of impurity phases (such as Bi_2O_3/$Bi_2Fe_4O_9$), which could be effectively suppressed via rapid annealing. A similar problem would occur in the synthesis of BFO nanostructures through chemical routes unless processing parameters are carefully optimized. Among the chemical processes in the literature, the soft chemical method first reported by Ghosh *et al*. is relatively easy to handle as it simply involves the use of tartaric acid as a template material and nitric acid as an oxidizing agent, meanwhile the crystallization of BFO could be realized at relatively low temperature and under ambient pressure[95]. We managed to modify the soft chemical method through which high quality nanofibers of BFO were obtained. The electrical measurements indicate that the nanofibers are ferroelectric and exhibit excellent photovoltaic performance.

5.4.2 Experimental Procedure

Fig. 5.13 shows the flowchart of BFO nanofiber preparation procedure. The whole procedure can be divided into two major sections: precursor solution preparation and electrospinning. Different amount of PVP was added to the precursor and different electric field was applied in the spinning process to decide best fiber growth condition. The photo-response of optimized nanofiber was examined and the following sections describe detail experimental procedure.

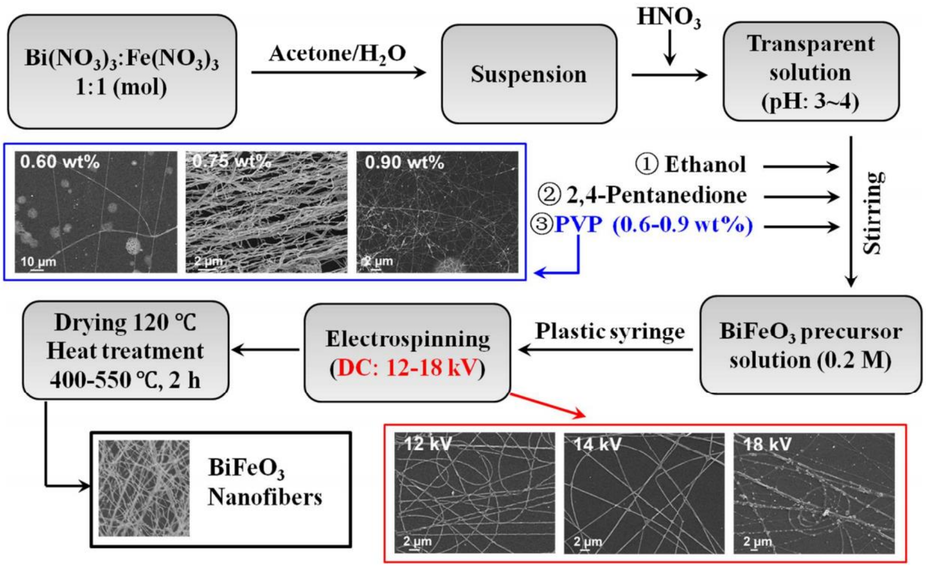

Fig. 5.13 Flowchart of the precursor preparation and nanofiber synthesis. Inserts: (blue) morphology of nanofibers prepared using different amount of PVP in solutions - 0.6, 0.75 and 0.9 wt%.; and (red) morphology of nanofibers synthesized at different accelerating voltages - 12, 14 and 18kV[96]**.**

5.4.2.1 Precursor solution preparation

The precursors were prepared via a sol-gel process. All start chemicals were of analytical grade. In a typical procedure, 1.20 g bismuth nitrate ($Bi(NO_3)_3$ $5H_2O$) and 1.00 g iron nitrate ($Fe(NO_3)_3$ $9H_2O$) were weighed and dissolved into a mixture of 10 ml acetone and 5 ml distilled water, followed by exposed to ultrasound for 5 minutes to give a suspended solution. Then 1 ml nitric acid (67%, mass ratio) was added dropwise until the suspended solution became transparent. After that, a 7.5 g solution of 10% (mass concentration) poly (vinyl pyrrolidone) (PVP, molecular weight of about 1 300 000) in ethanol was added dropwise and stirred for 30 minutes. Finally, 1 ml of 2, 4-pentanedione (99+ %) was added dropwise to the solution to form precursor solution.

5.4.2.2 Electrospinning

The processing conditions were (i) capillary-collector distance = 10 cm, (ii) accelerating voltage = 14 kV, and (iii) solution feeding rate = 0.5 ml/h. The as-spun fibers (collected on Al foil, Au/glass wafer, or Au/SiO2/Si wafer) were then dried at 120 ℃ for 2h. Thermogravimetric analysis and differential scanning calorimetry were conducted on a TG-DSC system (NETZSCH STA 449 C Jupiter®). Based on the analytical results, the thermal annealing were conducted at temperatures from 400 to 600 ℃ for 2h in ambient conditions.

5.4.2.3 Electrical and photovoltaic characterizations

The optical responses of BFO nanofibers were examined using a symmetric electrode configuration to eliminate the effects of different work functions of the electrodes and asymmetric Schottky-Ohmic contacts on the photovoltaic properties (asymmetric Schottky-Ohmic contact can also produce diode-like photocurrent). Au

IDEs were sputtered on highly transparent glass substrate. The nanofibers were deposited on Au IDE by electrospinning, as shown in Fig. 5.14. Before optical measurement, the BFO nanofibers were poled under a voltage of 200V, much larger then external bias applied during measurement (5V). The photocurrent-photovoltage response was measured under AM 1.5G illumination (100 mW/cm^2) provided by a solar simulator (Model 91160, Newport-Oriel Instruments, USA) with an AM 1.5 filter, and the photocurrent was record by an electrometer (Keithley 6517b).

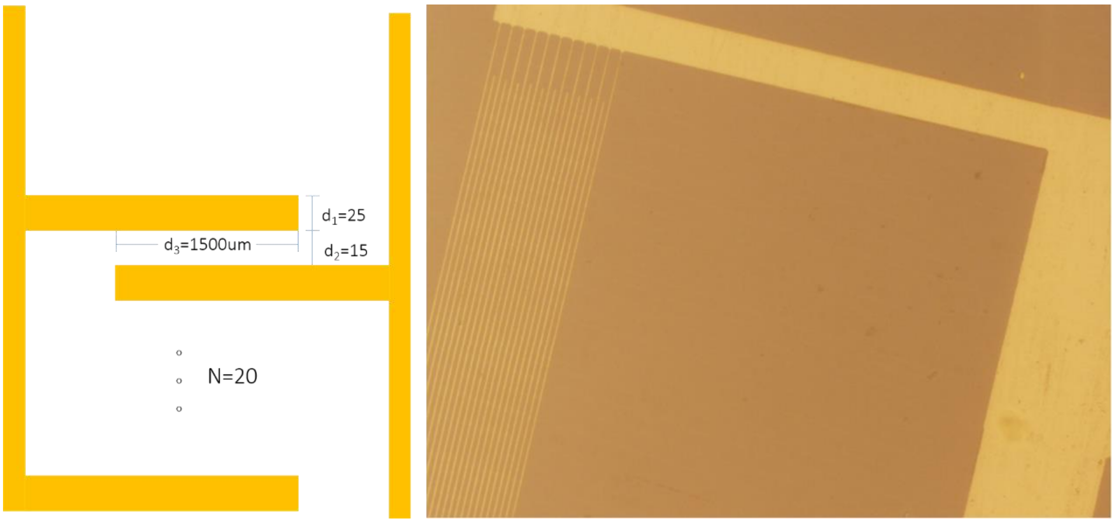

Fig. 5.14 Schematic diagram of IDE used in this work (left); optical photography of interdigital electrode pattern (right).

5.4.3 Results and discussion

5.4.3.1 Structure Characterization

Detailed structural analysis on BFO sample (annealed at 500 °C) was conducted and the results are shown in Fig. 5.15. Both SEM and TEM observations show clearly the polycrystalline nature of the nanofibers and the grain size is 10~20 nm. The XRD measurements in Fig. 5.15f indicate that BFO has a rhombohedral perovskite structure and no impurity phase was identified. Lattice parameters of BFO nanofibers were calculated using XRD analysis software and the results are as following, a = b = 0.5569 nm, c = 1.387 nm, $\alpha = \beta = 90^o$ and $\gamma = 120^o$. All the values of our sample are consistent with the literature data (JCPDS card No. 86-1518), suggesting that our samples are pure perovskite and free of internal stress. The SAED pattern and the corresponding high-resolution TEM (HRTEM) image further confirm the structural analysis. From the EDS analysis shown in Fig. 5.15b, we can calculate that the atomic ratio of Bi: Fe is almost 1: 1. All the analysis from the HRTEM is consistent with the XRD data.

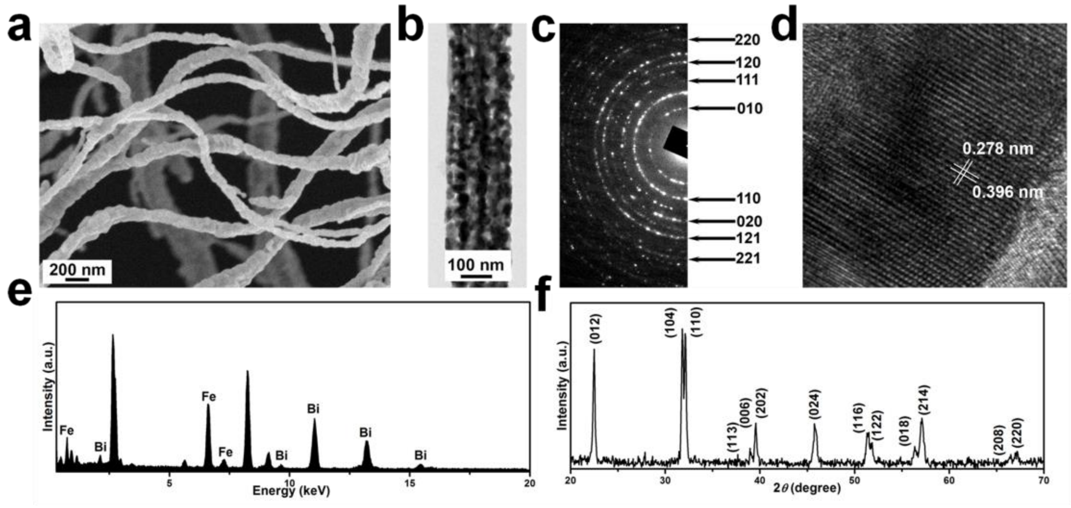

Fig. 5.15 (a) SEM image and (b) TEM image of the BFO nanofibers annealed at 500 ºC for 2h; (c), (d) and (e) the corresponding SEAD pattern, HRTEM image and the EDS spectra from (b) (all un-indexed peaks in (e) are caused by the copper grid used in TEM); and (f) XRD pattern of the annealed nanofibers.

5.4.3.2 Photovoltaic performance of BFO nanofibers

In the literature, two major types of ferroelectric thin film-based photovoltaic devices are reported, as schematically shown in Fig. 5.16. For the structural configuration of our devices, the calculation of material property is complicated due to the random distribution of the nanofibers. Nevertheless, one may still estimate the values of the parameters with an acceptable precision and accuracy. As the measured current from the photovoltaic device is I (mA), then the average current density J in a single nanofiber is

$$J = \frac{I}{S \times N} \quad (2)$$

where S is the average cross-section area of individual nanofiber, and N is the number of nanofibers per unit area (of the substrate). In our sample, the average diameter of the nanofibers is ~200 nm, so $S = 3.46\times10^{-10}$ cm^2. The averaged number of nanofibers on the device, estimated from the SEM image, is about 7.5×10^{-3}.

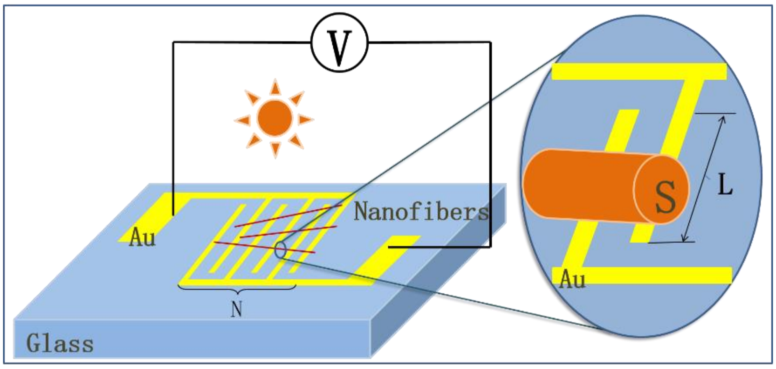

Fig. 5.16 Schematic setup for measurement of random BFO nanofiber-based photovoltaic devices.

If we preset the current of ~2.5 nA from the I-V curve, the current density can be calculated as: $J = 2.5\times10^{-6}/(3.46\times10^{-10}\times7.5\times10^{-3}) \approx 1$ mA/cm^2, as shown in Fig. 5.17-5.18 This value is ~10 times larger than that of BFO thin films in the literature[35]. From this result we may also estimate the light absorption coefficient of the nanofibers using the equation

$$J\ (short\text{-}circuit\ current) = \alpha \times \beta \times I_L$$

Where α is the light absorption coefficient, β is the glass linear coefficient (~0.1 cm/V), and I_L is the light intensity (100 mW/cm^2). If we assume J_{SC} to be 1 mA/cm^2, then the value of α is ~1.5× 10^7 cm^{-1}. This value is twice the typical value for BFO thin films in the literature. The photovoltaic effect of BFO nanofibers are further confirmed in Fig 5.19 where averaged current for different deposition time was measured, and it shows that more fibers bigger averaged photocurrent.

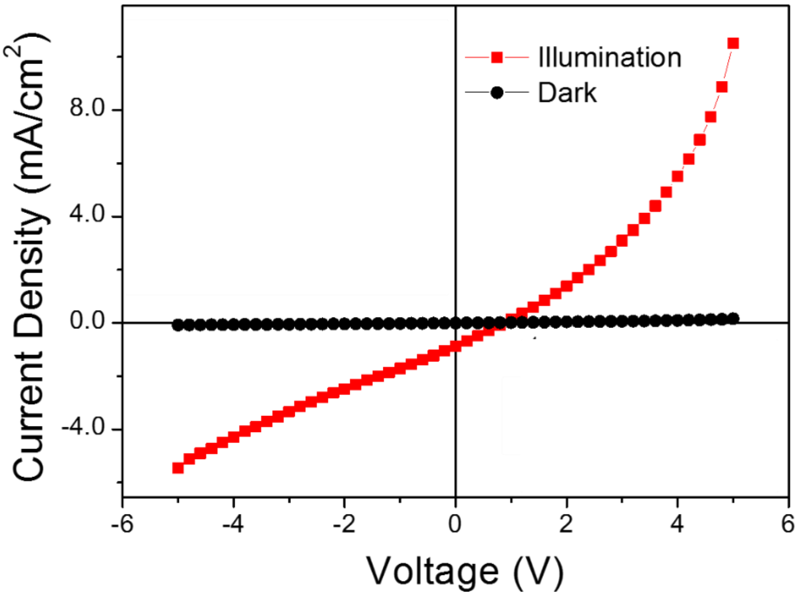

Fig. 5.17 Photo-response profile of the nanofibers.

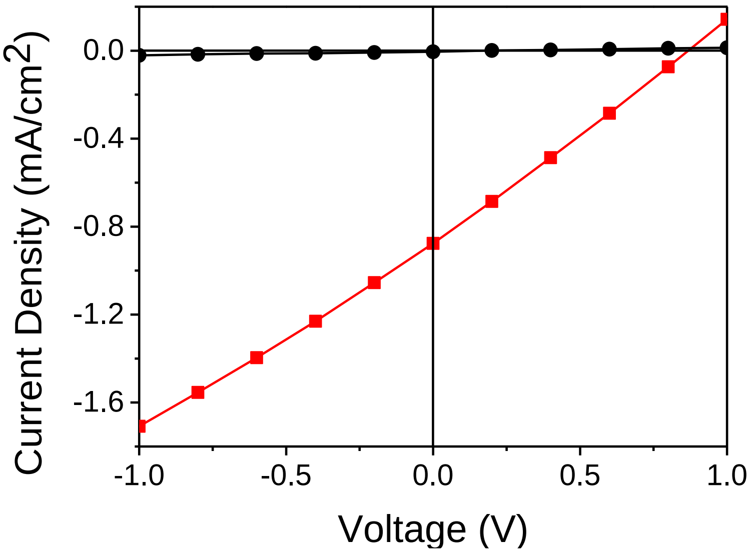

Fig. 5.18 Expanded view of current density behaviour around zero bias.

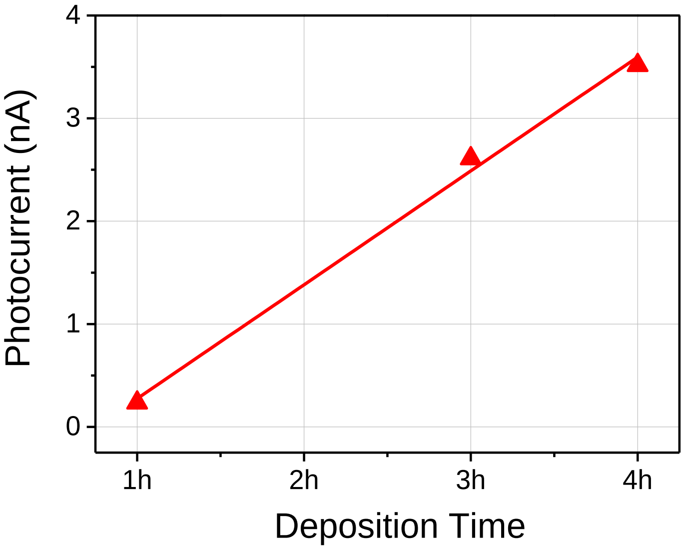

Fig. 5.19 Averaged photocurrent after several measurements for different deposition time from 1 to 4h.

5.4.3.3 Discussion

The reasons for the nanofibers showing enhanced photovoltaic properties could be related to several factors. First, the nanofibers are free-standing (as clearly shown by the XRD and SEM data) while the thin films are mechanically clamped by substrates. As it is generally believed, domain structure and dynamics are critical for the photovoltaic behaviours of the ferroelectric oxides; it is thus understandable that the free-standing feature of the nanofibers makes it possible for the ferroelectric domains switching more freely and efficiently. Second, the nanofibers could trap more photons due to geometric confinement. In the present work, the incident light is along the cross-sectional plane of the nanofibers, which is circular. Similar idea of “photon trapping” using reflection from a photonic crystal is widely applied in solar cells[97].

5.5 Summary

In this chapter, BFO thin films were deposited on PMN-PT and LAO substrates. The structure and photoelectric characterizations were conducted on these films. A small photocurrent was observed in BFO/PMN-PT sample while none was observed in BFO/LAO sample. The photovoltaic effect in BFO thin film is confirmed to be stable in rhombohedral phase regardless small stress, but diminished in a significantly distorted film. Additionally, a relatively large photocurrent is also obtained in strain-free BFO nanofiber, and the one dimensional structure is proposed to have promoted FePV effect in BFO.

Chapter 6. Conclusions and future work

6.1 Conclusions

In summary, the FePV effect of BFO thin film with planar electrode configuration was systematically investigated. Epitaxial $BiFeO_3$ thin films were deposited on $SrTiO_3$ substrates by pulsed laser deposition. The deposition process was optimized to obtain high quality BFO thin films with a steady short-circuit photocurrent density of 17.51 mA/cm^2 and open-circuit voltage of 0.21 V. The relative high power conversion efficiency (2.3%), much larger than typical value (<1%) measured in top-bottom electrode structure, infers that the planar electrode configuration is more suitable for application in photo-electricity conversion cells, photo sensors and memory devices. The influence of secondary phases in BFO thin film on FePV property was also discussed in detail. The result shows that the bismuth vacancy, which is induced by lowering oxygen pressure or ablating $Bi_{0.8}FeO_3$ target, is helpful to reduce leakage current that is critical for device stability, and also enables a larger open-circuit voltage. It is also suggested that Bi_2O_3 secondary phase induced by decreasing ablation rate or ablating $Bi_{1.2}FeO_3$ target is detrimental to electric properties of BFO thin film, therefore should be avoided in future research.

Then, the influence of electrode material to FePV property was examined. Two types of interface contact were established on purpose. Schottky contact was formed at Au/BFO interface while Ohmic contact was formed at Ti/BFO interface. The type of interface contact was confirmed by I-V curve and SPoM, and the photovoltaic behaviour of BFO thin film with different electrode contacts varied distinctively. The results showed that the short-circuit photocurrent of BFO thin film using titanium electrode was five times larger than the one using gold electrode which was widely used in many of the current studies. Since the work function of titanium metal is smaller than the electron infinity of BFO thin film, the formed Ohmic contact at Ti/BFO interface is helpful for charge transportation. Therefore, it is recommended to use titanium metal as the electrode in BFO material applications.

In the end, the influence of substrate-BFO interface on FePV property was investigated. BFO thin films deposited on LAO and PMN-PT single crystal substrates were characterized by XRD and Raman spectroscopy. A mixture of R- and T-like phases was confirmed in BFO/LAO sample due to large difference of lattice constant. The distortion of lattice structure along out-of-plane direction results in an undetectable planar photocurrent density under zero bias. Therefore, unlike excellent ferroelectric property observed in distorted BFO thin film, the bulk-like phase structure shows more favourable FePV effect of BFO material. For BFO/PMN-PT sample, it is implied that the FePV of BFO is not sensitive to small strain, different from the ferroelectric properties of BFO which is strain tunable. Photovoltaic effect of BFO nanofibers was also investigated. A prominent photocurrent was obtained and possible mechanism for such distinct photo-response in nano-device is discussed. Our results indicate great potential application of BFO nanofibers in stretchable photo-sensor devices.

6.2 Future work

Based on our work, the photovoltaic properties of BFO thin film have been investigated thoroughly in terms of film quality, electrode contact and substrate interface. The next big leap will be the further improvement of device for real applications in areas of energy harvesting, photo-sensing and memory device. For instant, we are planning to investigate the influence of asymmetric in-plane electrode material to the FePV effect of BFO thin film. Moreover, since our work is not particular designed for BFO only, it is also applicable for other perovskite oxide material, and it may open more opportunities for future application.

Reference

[1] A. G. Chynoweth, “Surface space-charge layers in barium titanate,” *Phys. Rev.*, vol. 102, no. 3, pp. 705–714, 1956.

[2] A. M. Glass, “High-voltage bulk photovoltaic effect and the photorefractive process in $LiNbO_3$,” *Appl. Phys. Lett.*, vol. 25, no. 4, p. 233, 1974.

[3] V. M. Fridkin and B. N. Popov, “The anomalous photovoltaic effect and photoconductivity in ferroelectrics,” *Ferroelectrics*, vol. 21, no. 1, pp. 611–613, 1978.

[4] F. S. Chen, “Optically induced change of refractive indices in $LiNbO_3$ and $LiTaO_3$,” *J. Appl. Phys.*, vol. 40, no. 8, pp. 3389–3396, 1969.

[5] W. Kraut and R. Von Baltz, “Anomalous bulk photovoltaic effect in ferroelectrics: A quadratic response theory,” *Phys. Rev. B*, vol. 19, no. 3, pp. 1548–1554, 1979.

[6] C. D. Hollister and D. Spencer, “Bulk photovoltaic effect in pure pyro-and piezoelectrics,” *Physics Letters A*, vol. 27, no. 4, pp. 364–366, 1980.

[7] R. Von Baltz and W. Kraut, “Theory of the bulk photovoltaic effect in pure crystals,” *Phys. Rev. B,* vol. 23, no. 10, pp. 5590–5596, 1981.

[8] W. Ruppel, R. Von Baltz, and P. Wurfel, “The origin of the photo-emf in ferroelectric and non-ferroelectric materials,” *Ferroelectrics*, vol. 43, no. 1, pp. 109–123, 1982.

[9] W. Ji, K. Yao, and Y. C. Liang, “Evidence of bulk photovoltaic effect and large tensor coefficient in ferroelectric $BiFeO_3$ thin films,” *Phys. Rev. B - Condens. Matter Mater. Phys.*, vol. 84, pp. 1–5, 2011.

[10] S. M. Young, F. Zheng, and A. M. Rappe, “First-principles calculation of the bulk photovoltaic effect in bismuth ferrite,” *Phys. Rev. Lett.*, vol. 109, no. 23, pp. 16–21, 2012.

[11] A. Bhatnagar, A. Roy Chaudhuri, Y. Heon Kim, D. Hesse, and M. Alexe, “Role of domain walls in the abnormal photovoltaic effect in $BiFeO_3$,” *Nat. Commun.*, vol. 4, no. May, p. 2835, 2013.

[12] J. Sipe and a. Shkrebtii, “Second-order optical response in semiconductors,” *Phys. Rev. B*, vol. 61, no. 8, pp. 5337–5352, 2000.

[13] F. Nastos and J. E. Sipe, “Optical rectification and shift currents in GaAs and

GaP response: Below and above the band gap," *Phys. Rev. B*, vol. 74, no. 3, pp. 1–15, 2006.

[14] Y. Yuan, Z. Xiao, B. Yang, and J. Huang, "Arising applications of ferroelectric materials in photovoltaic devices," *J. Mater. Chem. A*, vol. 2, no. 17, p. 6027, 2014.

[15] S. Y. Yang, J. Seidel, S. J. Byrnes, P. Shafer, C.-H. Yang, M. D. Rossell, P. Yu, Y.-H. Chu, J. F. Scott, J. W. Ager, L. W. Martin, and R. Ramesh, "Above-bandgap voltages from ferroelectric photovoltaic devices," *Nat. Nanotechnol.*, vol. 5, no. 2, pp. 143–147, 2010.

[16] J. Seidel, L. W. Martin, Q. He, Q. Zhan, Y.-H. Chu, A. Rother, M. E. Hawkridge, P. Maksymovych, P. Yu, M. Gajek, N. Balke, S. V Kalinin, S. Gemming, F. Wang, G. Catalan, J. F. Scott, N. a Spaldin, J. Orenstein, and R. Ramesh, "Conduction at domain walls in oxide multiferroics," *Nat. Mater.*, vol. 8, no. 3, pp. 229–234, 2009.

[17] H. Huang, "Solar energy: Ferroelectric photovoltaics," *Nat. Photonics*, vol. 4, no. 3, pp. 134–135, 2010.

[18] B. Meyer and D. Vanderbilt, "Ab initio study of ferroelectric domain walls in

$PbTiO_3$," *Physical Review B,* vol. 65, no. September 2001, pp. 1–11, 2002.

[19] J. F. Scott, "Room-temperature multiferroic magnetoelectrics," *NPG Asia Mater.*, vol. 5, no. 11, pp. e72–11, 2013.

[20] D. Y. Wang, N. Y. Chan, R. K. Zheng, C. Kong, and D. M. Lin, "Multiferroism in orientational engineered (La , Mn) co-substituted $BiFeO_3$ thin films thin films," *Journal of Applied Physics,* vol. 109, no. 11, pp. 114105, 2011.

[21] G. Catalan and J. F. Scott, "Physics and Applications of Bismuth Ferrite," *Adv. Mater.*, vol. 21, no. 24, pp. 2463–2485, 2009.

[22] L. You, C. Lu, P. Yang, G. Han, T. Wu, U. Luders, W. Prellier, K. Yao, L. Chen, and J. Wang, "Uniaxial magnetic anisotropy in $La_{0.7}Sr_{0.3}MnO_3$ thin films induced by multiferroic $BiFeO_3$ with striped ferroelectric domains," *Adv. Mater.*, vol. 22, pp. 4964–4968, 2010.

[23] D. Sando, A Agbelele, D. Rahmedov, J. Liu, P. Rovillain, C. Toulouse, I. C. Infante, A P. Pyatakov, S. Fusil, E. Jacquet, C. Carrétéro, C. Deranlot, S. Lisenkov, D. Wang, J.-M. Le Breton, M. Cazayous, A Sacuto, J. Juraszek, K. Zvezdin, L. Bellaiche, B. Dkhil, A. Barthélémy, and M. Bibes, "Crafting the

magnonic and spintronic response of $BiFeO_3$ films by epitaxial strain," *Nat. Mater.*, vol. 12, no. 7, pp. 641–6, 2013.

[24] H. Béa, M. Gajek, M. Bibes, and A. Barthélémy, "Spintronics with multiferroics," *Journal of Physics: Condensed Matter*, vol. 20, no. 43. 2008.

[25] J. M. Moreau, C. Michel, R. Gerson, and W. J. James, "Ferroelectric $BiFeO_3$ X-Ray and neutron diffraction study," *J. Phys. Chem. Solids*, vol. 32, pp. 1315–1320, 1971.

[26] F. Kubel and H. Schmid, "Structure of a ferroelectric and ferroelastic monodomain crystal of the perovskite $BiFeO_3$," *Acta Crystallogr. Sect. B Struct. Sci.*, vol. 46, no. 6, pp. 698–702, 1990.

[27] J. D. Bucci, B. K. Robertson, and W. J. James, "The precision determination of the lattice parameters and the coefficients of thermal expansion of $BiFeO_3$," *J. Appl. Crystallogr.*, vol. 5, no. 3, pp. 187–191, 1972.

[28] X. Qi, M. Wei, Y. Lin, Q. Jia, D. Zhi, J. Dho, M. G. Blamire, and J. L. MacManus-Driscoll, "High-resolution x-ray diffraction and transmission electron microscopy of multiferroic $BiFeO_3$ films," *Appl. Phys. Lett.*, vol. 86, no. 7, p. 071913, 2005.

[29] J. R. Chen, W. L. Wang, J. Li, and G. H. Rao, “X-ray diffraction analysis and specific heat capacity of (Bi_{1-x} La_x) FeO_3 perovskites,” *Journal of Alloys and Compounds,* vol. 459, pp. 66–70, 2008.

[30] A. Palewicz, R. Przeniosło, I. Sosnowska, and A. W. Hewat, “Atomic displacements in $BiFeO_3$ as a function of temperature: Neutron diffraction study,” *Acta Crystallogr. Sect. B Struct. Sci.*, vol. 63, no. 4, pp. 537–544, 2007.

[31] J. R. Teague, R. Gerson, and W. J. James, “Dielectric hysteresis in single crystal $BiFeO_3$,” *Solid State Communications,* vol. 8, no. 90, pp. 1073–1074, 1970.

[32] J. Wang, *et al.* “Epitaxial $BiFeO_3$ Multiferroic Thin Film Heterostructures,” *Science*, vol. 299, no. 5613, pp. 1719–1722, 2003.

[33] D. Lebeugle, D. Colson, A. Forget, M. Viret, D. Lebeugle, D. Colson, A. Forget, and M. Viret, “Very large spontaneous electric polarization in $BiFeO_3$ single crystals at room temperature and its evolution under cycling fields,” *Appl. Phys. Lett.*, vol. 91, no. 2, p. 022907, 2007.

[34] V. V. Shvartsman, W. Kleemann, R. Haumont, and J. Kreisel, “Large bulk polarization and regular domain structure in ceramic $BiFeO_3$,” *Appl. Phys.*

Lett., vol. 90, no. 17, p. 172115, 2007.

[35] S. J. Clark, J. Robertson, and S. J. Clark, “Band gap and Schottky barrier heights of multiferroic $BiFeO_3$,” *Applied Physics Letters*, vol. 132903, no. 2007, pp. 158–161, 2013.

[36] T. Choi, S. Lee, Y. J. Choi, V. Kiryukhin, and S.-W. Cheong, “Switchable ferroelectric diode and photovoltaic effect in $BiFeO_3$,” *Science*, vol. 324, no. 5923, pp. 63–66, 2009.

[37] G. Xu, H. Hiraka, G. Shirane, J. Li, J. Wang, and D. Viehland, “Low symmetry phase in (001) $BiFeO_3$ epitaxial constrained thin films,” *Appl. Phys. Lett.*, vol. 86, no. 001, pp. 1–3, 2005.

[38] H. Liu, K. Yao, P. Yang, Y. Du, Q. He, Y. Gu, X. Li, S. Wang, X. Zhou, and J. Wang, “Thickness-dependent twinning evolution and ferroelectric behavior of epitaxial $BiFeO_3$ (001) thin films,” *Phys. Rev. B*, vol. 82, no. 6, p. 064108, 2010.

[39] Z. Chen, S. Prosandeev, Z. L. Luo, W. Ren, Y. Qi, C. W. Huang, L. You, C. Gao, I. A. Kornev, T. Wu, J. Wang, P. Yang, T. Sritharan, L. Bellaiche, and L. Chen, “Coexistence of ferroelectric triclinic phases in highly strained $BiFeO_3$

films," *Phys. Rev. B,* vol. 84, no. 9, pp. 1–6, 2011.

[40] J. E. Giencke, C. M. Folkman, S. Baek, and C. Eom, "Tailoring the domain structure of epitaxial $BiFeO_3$ thin films," *Curr. Opin. Solid State Mater. Sci.*, vol. 18, no. 1, pp. 39–45, 2014.

[41] S. Ryu, J. Y. Kim, Y. H. Shin, B.-G. Park, J. Y. Son, and H. M. Jang, "Enhanced Magnetization and Modulated Orbital Hybridization in Epitaxially Constrained $BiFeO_3$ Thin Films with Rhombohedral Symmetry," *Chem. Mater.*, vol. 21, no. 16, pp. 5050–5057, 2009.

[42] R. J. Zeches, M. D. Rossell, J. X. Zhang, A. J. Hatt, Q. He, C.-H. Yang, A. Kumar, C. H. Wang, A. Melville, C. Adamo, G. Sheng, Y.-H. Chu, J. F. Ihlefeld, R. Erni, C. Ederer, V. Gopalan, L. Q. Chen, D. G. Schlom, N. A. Spaldin, L. W. Martin, and R. Ramesh, "A Strain-Driven Morphotropic Phase Boundary in $BiFeO_3$," *Science*, vol. 326, no. 5955, pp. 977–980, 2009.

[43] D. Ricinschi, K.-Y. Yun, and M. Okuyama, "A mechanism for the 150 $\mu C/cm^{-2}$ polarization of $BiFeO_3$ films based on first-principles calculations and new structural data," *J. Phys. Condens. Matter*, vol. 18, no. 6, pp. L97–L105, 2006.

[44] H. Béa, B. Dupé, S. Fusil, R. Mattana, E. Jacquet, B. Warot-Fonrose, F. Wilhelm, A. Rogalev, S. Petit, V. Cros, A. Anane, F. Petroff, K. Bouzehouane, G. Geneste, B. Dkhil, S. Lisenkov, I. Ponomareva, L. Bellaiche, M. Bibes, and A. Barthélémy, "Evidence for room-temperature multiferroicity in a compound with a giant axial ratio," *Phys. Rev. Lett.*, vol. 102, no. May, pp. 1–5, 2009.

[45] Z. H. Chen, L. You, C. W. Huang, Y. J. Qi, J. L. Wang, T. Sritharan, and L. Chen, "Nanoscale domains in strained epitaxial $BiFeO_3$ thin Films on $LaSrAlO_4$ substrate," *Appl. Phys. Lett.*, vol. 96, no. 25, p. -, 2010.

[46] D. Mazumdar, V. Shelke, M. Iliev, S. Jesse, A. Kumar, S. V. Kalinin, A. P. Baddorf, and A. Gupta, "Nanoscale Switching Characteristics of Nearly Tetragonal $BiFeO_3$ Thin Films," *Nano Lett.*, vol. 10, no. 7, pp. 2555–2561, 2010.

[47] H. M. Christen, J. H. Nam, H. S. Kim, A. J. Hatt, and N. A. Spaldin, "Stress-induced R - M_A - M_C - T symmetry changes in $BiFeO_3$ films," *Physical Review B*, vol. 144107, pp. 1–7, 2011.

[48] J. C. Yang, Q. He, S. J. Suresha, C. Y. Kuo, C. Y. Peng, R. C. Haislmaier, M.

A. Motyka, G. Sheng, C. Adamo, H. J. Lin, Z. Hu, L. Chang, L. H. Tjeng, E. Arenholz, N. J. Podraza, M. Bernhagen, R. Uecker, D. G. Schlom, V. Gopalan, L. Q. Chen, C. T. Chen, R. Ramesh, and Y. H. Chu, “Orthorhombic $BiFeO_3$,” *Phys. Rev. Lett.*, vol. 109, no. 24, p. 247606, 2012.

[49] J. X. Zhang, Q. He, M. Trassin, W. Luo, D. Yi, M. D. Rossell, P. Yu, L. You, C. H. Wang, C. Y. Kuo, J. T. Heron, Z. Hu, R. J. Zeches, H. J. Lin, A. Tanaka, C. T. Chen, and L. H. Tjeng, “Microscopic Origin of the Giant Ferroelectric Polarization in Tetragonal-like $BiFeO_3$,” *Phys. Rev. Lett.*, vol. 147602, no. September, pp. 1–5, 2011.

[50] Y.-H. Chu, Q. Zhan, L. W. Martin, M. P. Cruz, P.-L. Yang, G. W. Pabst, F. Zavaliche, S.-Y. Yang, J.-X. Zhang, L.-Q. Chen, D. G. Schlom, I.-N. Lin, T.-B. Wu, and R. Ramesh, “Nanoscale Domain Control in Multiferroic $BiFeO_3$ Thin Films,” *Adv. Mater.*, vol. 18, no. 17, pp. 2307–2311, 2006.

[51] Y. H. Chu, M. P. Cruz, C. H. Yang, L. W. Martin, P. L. Yang, J. X. Zhang, K. Lee, P. Yu, L. Q. Chen, and R. Ramesh, “Domain control in multiferroic $BiFeO_3$ through substrate vicinality,” *Adv. Mater.*, vol. 19, no. 18, pp. 2662–2666, 2007.

[52] H. W. Jang, D. Ortiz, S. H. Baek, C. M. Folkman, R. R. Das, P. Shafer, Y. Chen, C. T. Nelson, X. Pan, R. Ramesh, and C. B. Eom, “Domain engineering for enhanced ferroelectric properties of epitaxial (001) BiFeO thin films,” *Adv. Mater.*, vol. 21, no. 001, pp. 817–823, 2009.

[53] J. H. Lee, K. Chu, A. a. Ünal, S. Valencia, F. Kronast, S. Kowarik, J. Seidel, and C.-H. Yang, “Phase separation and electrical switching between two isosymmetric multiferroic phases in tensile strained $BiFeO_3$ thin films,” *Phys. Rev. B*, vol. 89, no. 14, p. 140101, 2014.

[54] M. Daraktchiev, G. Catalan, and J. F. Scott, “Landau theory of domain wall magnetoelectricity,” *Phys. Rev. B*, vol. 81, no. 22, p. 224118, 2010.

[55] H. T. Yi, T. Choi, S. G. Choi, Y. S. Oh, and S. W. Cheong, “Mechanism of the switchable photovoltaic effect in ferroelectric $BiFeO_3$,” *Adv. Mater.*, vol. 23, no. 30, pp. 3403–3407, 2011.

[56] R. Moubah, O. Rousseau, D. Colson, A. Artemenko, M. Maglione, and M. Viret, “Photoelectric Effects in Single Domain $BiFeO_3$ Crystals,” *Adv. Funct. Mater.*, vol. 22, no. 22, pp. 4814–4818, 2012.

[57] M. Alexe and D. Hesse, “Tip-enhanced photovoltaic effects in bismuth ferrite,”

Nat. Commun., vol. 2, p. 256, 2011.

[58] V. S. Filip'ev and et al, "Preparation and Lattice Parameters of $BiFeO_3$," *Appl. Phys. Lett.*, vol. 32, no. 6, p. 958, 1960.

[59] S. Y. Yang, L. W. Martin, S. J. Byrnes, T. E. Conry, S. R. Basu, S. Y. Yang, L. W. Martin, S. J. Byrnes, T. E. Conry, S. R. Basu, and D. Paran, "Photovoltaic effects in $BiFeO_3$," *Appl. Phys. Lett.*, vol. 062909, pp. 1–4, 2009.

[60] W. Ji, K. Yao, and Y. C. Liang, "Bulk Photovoltaic Effect at Visible Wavelength in Epitaxial Ferroelectric $BiFeO_3$ Thin Films," *Adv. Mater.*, vol. 22, no. 15, pp. 1763–1766, 2010.

[61] B. Chen, M. Li, Y. Liu, Z. Zuo, F. Zhuge, Q.-F. Zhan, and R.-W. Li, "Effect of top electrodes on photovoltaic properties of polycrystalline $BiFeO_3$ based thin film capacitors," *Nanotechnology*, vol. 22, no. 19, p. 195201, 2011.

[62] R. Nechache, C. Harnagea, S. Licoccia, E. Traversa, A. Ruediger, R. Nechache, C. Harnagea, S. Licoccia, E. Traversa, A. Ruediger, and A. Pignolet, "Photovoltaic properties of Bi_2FeCrO_6 epitaxial thin films," *Appl. Phys. Lett.*, vol. 202902, no. 2011, pp. 2011–2014, 2013.

[63] R. Guo, L. You, Y. Zhou, Z. S. Lim, X. Zou, L. Chen, R. Ramesh, and J. Wang, “Non-volatile memory based on the ferroelectric photovoltaic effect.,” *Nat. Commun.*, vol. 4, p. 1990, 2013.

[64] F. Yan, G. Chen, L. Lu, and J. E. Spanier, “Dynamics of photogenerated surface charge on $BiFeO_3$ films.,” *ACS Nano*, vol. 6, no. 3, pp. 2353–60, 2012.

[65] W. M. Lee, J. H. Sung, K. Chu, X. Moya, D. Lee, C. J. Kim, N. D. Mathur, S. W. Cheong, C. H. Yang, and M. H. Jo, “Spatially resolved photodetection in leaky ferroelectric $BiFeO_3$,” *Adv. Mater.*, vol. 24, no. 10, pp. 49–53, 2012.

[66] G. Catalan, J. Seidel, R. Ramesh, and J. F. Scott, “Domain wall nanoelectronics,” *Rev. Mod. Phys.*, vol. 84, no. 1, pp. 119–156, 2012.

[67] K. Prashanthi, R. Gaikwad, and T. Thundat, “Surface dominant photoresponse of multiferroic $BiFeO_3$ nanowires under sub-bandgap illumination.,” *Nanotechnology*, vol. 24, no. 50, p. 505710, 2013.

[68] N. Nuraje, X. Dang, J. Qi, M. a. Allen, Y. Lei, and A. M. Belcher, “Biotemplated synthesis of perovskite nanomaterials for solar energy conversion,” *Adv. Mater.*, vol. 24, p. 2885, 2012.

[69] G. Hass and J. Ramsey, “Vacuum Deposition of Dielectric and Semiconductor

Films by a CO_2 Laser," *Appl. Opt.*, vol. 8, no. 6, pp. 1115–1118, 1969.

[70] H. M. Smith and A. F. Turner, "Vacuum Deposited Thin Films Using a Ruby Laser," *Appl. Opt.*, vol. 4, no. 1, pp. 147–148, 1965.

[71] G. J. H. M. Rijnders, G. Koster, D. H. A. Blank, and H. Rogalla, "In situ monitoring during pulsed laser deposition of complex oxides using reflection high energy electron diffraction under high oxygen pressure," *Appl. Phys. Lett.*, vol. 70, no. 14, p. 1888, 1997.

[72] K. Ueda, H. Tabata, and T. Kawai, "Coexistence of ferroelectricity and ferromagnetism in $BiFeO_3$–$BaTiO_3$ thin films at room temperature," *Appl. Phys. Lett.*, vol. 75, no. 4, p. 555, 1999.

[73] Y. P. Wang, L. Zhou, M. F. Zhang, X. Y. Chen, J. M. Liu, and Z. G. Liu, "Room-temperature saturated ferroelectric polarization in $BiFeO_3$ ceramics synthesized by rapid liquid phase sintering," *Appl. Phys. Lett.*, vol. 84, no. 10, pp. 1731–1733, 2004.

[74] M. K. Singh, S. Ryu, and H. M. Jang, "Polarized Raman scattering of multiferroic $BiFeO_3$ thin films with pseudo-tetragonal symmetry," *Phys. Rev. B*, vol. 72, no. 13, p. 132101, 2005.

[75] H. Bea, M. Bibes, S. Petit, J. Kreisel, and A. Barthelemy, “Structural distortion and magnetism of $BiFeO_3$ epitaxial thin films : a Raman spectroscopy and neutron diffraction study,” *Philos. Mag. Lett.*, vol. 87, no. 3–4, pp. 165–174, 2007.

[76] M. N. Iliev, M. V. Abrashev, D. Mazumdar, V. Shelke, and A. Gupta, “Polarized Raman spectroscopy of nearly tetragonal $BiFeO_3$ thin films,” *Phys. Rev. B*, vol. 82, no. 1, p. 014107, 2010.

[77] R. Haumont, J. Kreisel, and P. Bouvier, “Raman scattering of the model multiferroic oxide $BiFeO_3$: effect of temperature, pressure and stress,” *Phase Transitions*, vol. 79, no. 12. pp. 1043–1064, 2006.

[78] R. Palai, R. S. Katiyar, H. Schmid, P. Tissot, S. J. Clark, J. Robertson, S. A. T. Redfern, G. Catalan, and J. F. Scott, “β phase and γ−β metal-insulator transition in multiferroic $BiFeO_3$,” *Phys. Rev. B*, vol. 77, no. 1, p. 014110, 2008.

[79] A. J. Hatt and N. A. Spaldin, “Strain-induced isosymmetric phase transition in $BiFeO_3$,” *Phys. Rev. B*, vol. 81, no. 5–1, p. 012102, 2010.

[80] H.-J. Liu, W.-I. Liang, Y.-H. Chu, H. Zheng, and R. Ramesh, “Self-assembled

vertical heteroepitaxial nanostructures: from growth to functionalities," *MRS Commun.*, vol. 4, no. 02, pp. 31–44, 2014.

[81] H. B́a, M. Bibes, a. Barth́ĺmy, K. Bouzehouane, E. Jacquet, a. Khodan, J. P. Contour, S. Fusil, F. Wyczisk, a. Forget, D. Lebeugle, D. Colson, and M. Viret, "Influence of parasitic phases on the properties of $BiFeO_3$ epitaxial thin films," *Appl. Phys. Lett.*, vol. 87, no. 7, pp. 50–52, 2005.

[82] L. You, N. Chua, K. Yao, L. Chen, and J. Wang, "Influence of oxygen pressure on the ferroelectric properties of epitaxial $BiFeO_3$ thin films by pulsed laser deposition," *Phys. Rev. B*, vol. 80, no. 2, p. 024105, 2009.

[83] R. Guo, L. You, M. Motapothula, Z. Zhang, M. B. H. Breese, L. Chen, D. Wu, and J. Wang, "Influence of target composition and deposition temperature on the domain structure of $BiFeO_3$ thin films," *AIP Adv.*, vol. 2, no. 4, p. 042104, 2012.

[84] R. Guo, L. You, Y. Zhou, Z. Shiuh Lim, X. Zou, L. Chen, R. Ramesh, and J. Wang, "Non-volatile memory based on the ferroelectric photovoltaic effect," *Nat. Commun.*, vol. 4, no. May, pp. 1–5, 2013.

[85] W. Hong, H. N. Lee, M. Yoon, H. M. Christen, D. H. Lowndes, Z. Suo, and Z.

Zhang, "Persistent Step-Flow Growth of Strained Films on Vicinal Substrates," *Phys. Rev. Lett.*, vol. 95, no. 9, p. 095501, 2005.

[86] V. R. Palkar and R. Pinto, "$BiFeO_3$ thin films: Novel effects," *Pramana - J Phys*, vol. 58, no. 5–6, pp. 1003–1008, 2002.

[87] H. Liu, P. Yang, K. Yao, and J. Wang, "Growth rate induced monoclinic to tetragonal phase transition in epitaxial $BiFeO_3$ (001) thin films," *Appl. Phys. Lett.*, vol. 98, no. 10, pp. 101–104, 2011.

[88] A. R. Damodaran, S. Lee, J. Karthik, S. MacLaren, and L. W. Martin, "Temperature and thickness evolution and epitaxial breakdown in highly strained $BiFeO_3$ thin films," *Phys. Rev. B*, vol. 85, no. 2, p. 24113, 2012.

[89] I. C. Infante, S. Lisenkov, B. Dupé, M. Bibes, S. Fusil, E. Jacquet, G. Geneste, S. Petit, A. Courtial, J. Juraszek, L. Bellaiche, A. Barthélémy, and B. Dkhil, "Bridging Multiferroic Phase Transitions by Epitaxial Strain in $BiFeO_3$," *Phys. Rev. Lett.*, vol. 105, no. 5, p. 057601, 2010.

[90] M. M. Yang, X. Q. Zhao, J. Wang, Q. X. Zhu, J. X. Zhang, X. M. Li, H. S. Luo, X. G. Li, and R. K. Zheng, "Intrinsic and quantitative effects of in-plane strain on ferroelectric properties of Mn-doped $BiFeO_3$ epitaxial films by in

situ inducing strain in substrates," *Appl. Phys. Lett.*, vol. 104, no. 5, p. 052902, 2014.

[91] A. Bhatnagar, Y. H. Kim, D. Hesse, and M. Alexe, "Persistent Photoconductivity in Strained Epitaxial $BiFeO_3$ Thin Films.," *Nano Lett.*, vol. 14, no. 9, pp. 5224–8, 2014.

[92] A. Bhatnagar, Y. H. Kim, D. Hesse, and M. Alexe, "Sub-band level-assisted photoconduction in epitaxial $BiFeO_3$ films," *Appl. Phys. Lett.*, vol. 105, p. 122905, 2014.

[93] C. Himcinschi, A. Bhatnagar, A. Talkenberger, M. Barchuk, D. R. T. Zahn, D. Rafaja, J. Kortus, and M. Alexe, "Optical properties of epitaxial $BiFeO_3$ thin films grown on $LaAlO_3$," *Appl. Phys. A*, vol. 106, no. 1, p. 012908, 2015.

[94] D. Li and Y. Xia, "Electrospinning of nanofibers: Reinventing the wheel?," *Adv. Mater.*, vol. 16, no. 14, pp. 1151–1170, 2004.

[95] S. Ghosh, S. Dasgupta, A. Sen, and H. Sekhar Maiti, "Low-Temperature Synthesis of Nanosized Bismuth Ferrite by Soft Chemical Route," *J. Am. Ceram. Soc.*, vol. 88, no. 5, pp. 1349–1352, 2005.

[96] L. Fei, Y. Hu, X. Li, R. Song, L. Sun, H. Huang, H. Gu, H. L. W. Chan, and Y.

Wang, “Electro spun Bismuth Ferrite Nanofibers for Potential Applications in Ferroelectric Photovoltaic Devices,” *ACS Appl. Mater. Interfaces*, vol. 7, no. 6, pp. 3665–3670, 2015.

[97] M. Guo, K. Xie, J. Lin, Z. Yong, C. T. Yip, L. Zhou, Y. Wang, and H. Huang, “Design and coupling of multifunctional TiO_2 nanotube photonic crystal to nanocrystalline titania layer as semi-transparent photoanode for dye-sensitized solar cell,” *Energy Environ. Sci.*, pp. 9881–9888, 2012.